7-12-2014

Discovery of the Bc(2S) Meson and Development of Pixel Detectors for Future Particle Collider Experiments

Wang Rui

Rui Wang

Candidate

Department of Physics and Astronomy

Department

This dissertation is approved, and it is acceptable in quality and form for publication:

Approved by the Dissertation Committee:

Sally Seidel , Chairperson

Steven M. Errede

Igor Gorelov

Rouzbeh Allahverdi

Discovery of the $B_c(2S)$ Meson and Development of Pixel Detectors for Future Particle Collider Experiments

by

Rui Wang

B.S., Wuhan University, 2007
M.S., Department of Physics and Astronomy, University of New Mexico, 2011

DISSERTATION

Submitted in Partial Fulfillment of the
Requirements for the Degree of

Doctor of Philosophy
Physics

The University of New Mexico

Albuquerque, New Mexico

May, 2014

Dedication

These years of hard work and effort I dedicate to my parents. They never doubted my ability to succeed and do everything they can to support me both physically and spiritually. Of course the rest of my family have been supportive, even though they are thousands of miles away. Then, there are my friends, too many to list here. Some I want to mention are those whose friendship means a great deal to me. These include my best friends: Jin He, Jin Yu, Chao You, Lei Zheng, Yu Cheng, Ting Yu, Ruomin Sun, Xuan Pan, Chen Chen, Tong Xia, etc. I miss you all.

Acknowledgments

I would like to thank my advisor, Professor Sally Seidel, for taking me into the beautiful world of particle physics and supporting all my work. In these five years I have learned many lessons, about physics and people. I'm now even more glad to choose to learn physics and do want to pursue a career in science. I also thank my collaborators, Konstantin Toms, Igor Gorelov and Martin Hoeferkamp. I have learned so much from each one of you through your brilliant advice and discussions. I really enjoyed the projects we worked on. I have several other people to thank: Harris Kagan, James Catmore, Maria Smizanska, Kerstin Lantzsch, Roger Jones, Beniamino Di Girolamo, Stephen Gibson and Daniel Muenstermann. Thank you for all your support on the projects. Finally, thank you Alessandro Cerri, for the endless discussion.

Discovery of the $B_c(2S)$ Meson and Development of Pixel Detectors for Future Particle Collider Experiments

by

Rui Wang

B.S., Wuhan University, 2007
M.S., Department of Physics and Astronomy, University of New Mexico, 2011

Ph.D., Physics, University of New Mexico, 2014

Abstract

This work involves an analysis of data recorded at the Large Hadron Collider combined with a program to develop detectors for future collider experiments.

Using the full 4.9 fb^{-1} of 7 TeV data collected in 2011 and the 19.2 fb^{-1} of 8 TeV data collected in 2012, the $B_c(2S)$ meson has been observed with the ATLAS detector in the hadronic decay mode $B_c(2S) \to B_c\pi^+\pi^-$, $B_c \to J/\psi\pi$. This new state has been found in the mass difference distribution with invariant mass $6845 \pm 7_{stat.} \pm 4_{syst.}$ MeV. To prepare for the high radiation environment at the High Luminosity LHC, diamond sensors are being developed. Their leakage current and resistivity are measured at fluences and temperatures relevant to the ATLAS upgrade. No evidence of dependence of the resistivity on fluence or temperature has been observed for the ranges [-10 °C, +20 °C] and [0, $1.0 \times 10^{16} \mathrm{n_{eq}/cm^2}$]. To study the radiation damage of the sensors in the ATLAS Pixel Detector, their leakage current is monitored at

the level of single pixel modules. The result agrees with a prediction based on the Hamburg model.

Contents

List of Figures

List of Tables

Glossary

Br	The branching ratio.
$\mathscr{R}$	The ratio.
$\mathscr{L}$	The luminosity.
Γ	The decay width.
p_{T}	The transverse momentum.
PV	The primary vertex reconstructed by the ATLAS software.
SV	The reconstructed secondary vertex; normally the decay vertex.
d^0	The impact parameter of the track related to the primary vertex.
d^0_{xy}	The transverse impact parameter of the track related to the primary vertex.
$\sigma(d^0_{xy})$	The error on the measured transverse impact parameter of the track related related to the primary vertex.
$z0$	The longitudinal impact parameter of the track related to the primary vertex.
$\chi^2/N.d.o.f.$	The χ^2 per number of degrees of freedom.

Chapter 1

Introduction

This chapter presents a brief overview of the Standard Model (SM) and the $\bar{b}c$ bound states known as the B_c meson family. The $\bar{b}c$ is the only meson state combining two different heavy quarks. It probes Quantum Chromodynamics (QCD) differently than the $c\bar{c}$ abd $b\bar{b}$ do. It is mainly produced through the gluon-gluon (gg) fusion process. Its production cross section is suppressed to $\mathscr{O}(10^{-3})$ compared to other b hadrons. The $\bar{b}c$ system is expected to have a rich mass spectrum.

1.1 Introduction to the Standard Model

Currently, our understanding of subatomic particle dynamics is based on the Standard Model. This is a renormalizable field theory that encompasses three of the four fundamental interactions, electromagnetism, the weak interaction, and the strong nuclear interaction. Particle relationships in the Standard Model are described by $SU(3) \times SU(2) \times U(1)$ gauge symmetry. The $SU(3)$ group refers to quantum chromodynamics, and describes the interactions of quarks and gluons through the color charge. The $SU(2) \times U(1)$ refers to the electroweak interaction. The first step in

the unification of the Standard Model was the combining of the electromagnetic and weak interactions in the 1960's [1]. The model incorporated the Higgs mechanism [2–4], which gives mass to the weak mediators, in 1967. The description of the strong interaction acquired its modern form around 1974, with its current formulation finalized upon the experimental confirmation of the existence of quarks in the mid-1970's. The discovery of the W and Z bosons were achieved in 1983, the top quark in 1995, the tau neutrino in 2000, and the Higgs boson in 2012 [6, 7]. This completed the set of predicted particles (Figure 1.1). Predictions are possible over scales down to 10^{-18} m and energies to about 200 GeV [8].

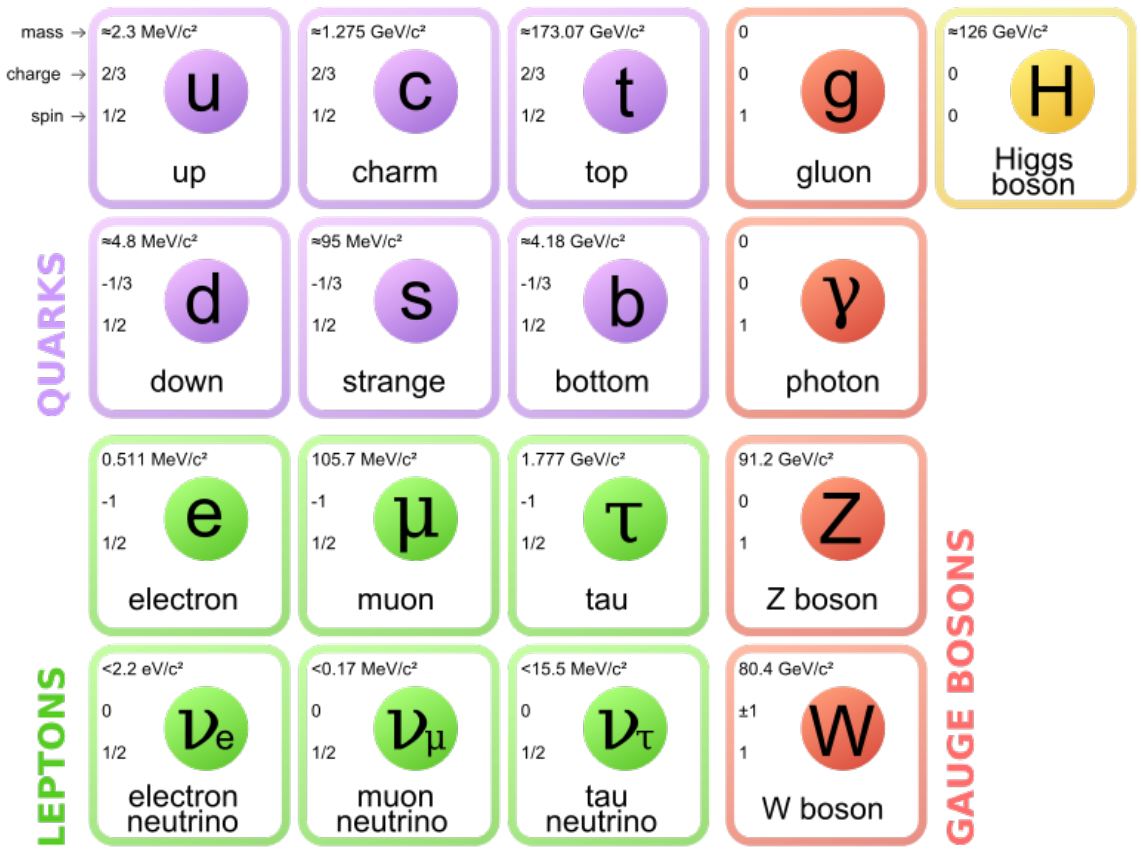

Figure 1.1: The Standard Model of elementary particles: the 12 fundamental fermions, the one fundamental scalar, and 4 fundamental bosons. [5]

The Standard Model includes 61 elementary particles: 12 fermions with spin $\frac{1}{2}$, 3 kinds of bosons with spin 1, and the Higgs boson with spin 0.

Fermions obey a statistical rule that leads to the Pauli exclusion principle, and each of them has a corresponding antiparticle. There are two types of fermions:

- Six quarks: $u,\ d,\ c,\ s,\ b,\ t$. They carry color charge and interact via the strong interaction. The quarks bind to form color-neutral composite particles, the hadrons, which contain a quark and an antiquark (mesons) or three quarks (baryons). Quarks carry electric charge and weak isospin as well, and hence they interact with other fermions both via the electromagnetic interaction and the weak interaction.

- Six leptons: $e,\ \nu_e,\ \mu,\ \nu_\mu,\ \tau,\ \nu_\tau$. They do not carry color charge, so they are only influenced by the gravitational and electroweak interactions. The three neutrinos do not have electric charge and are difficult to detect.

The quarks and leptons can be classified into doublets and combined to form 3 generations (Figure 1.1), with corresponding particles between generations exhibiting similar physical characteristics, and with mass increasing by generation.

Bosons are the carriers of the forces. In the Standard Model, there are three types:

- The photon is a massless $U(1)$ gauge boson that mediates the electromagnetic force between electrically charged particles in processes described by quantum electrodynamics (QED).

- The W^+, W^-, and Z^0 are $SU(2)$ gauge bosons that mediate the weak interactions between particles of different flavors. They are massive due to the breaking of the $SU(2)$ symmetry, and this limits the range of the weak nuclear force. The $W^\pm$ bosons have positive and negative electric charge and are

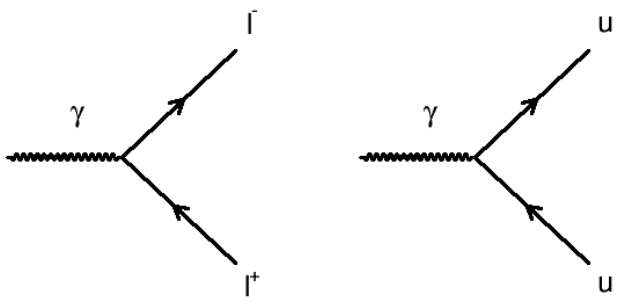

(a) (b)

Figure 1.2: Examples of electromagnetic interactions.

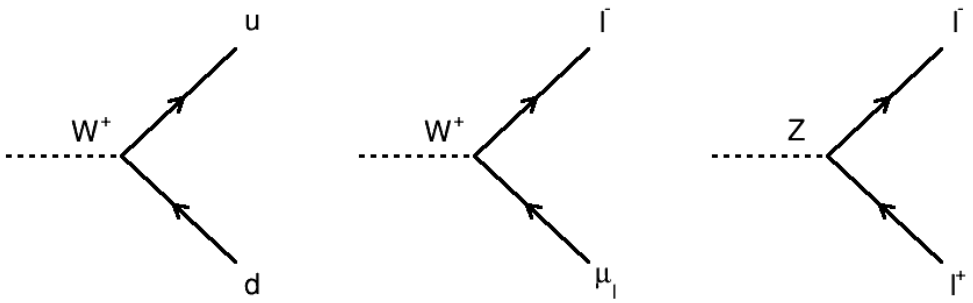

(a) (b) (c)

Figure 1.3: Examples of weak interactions.

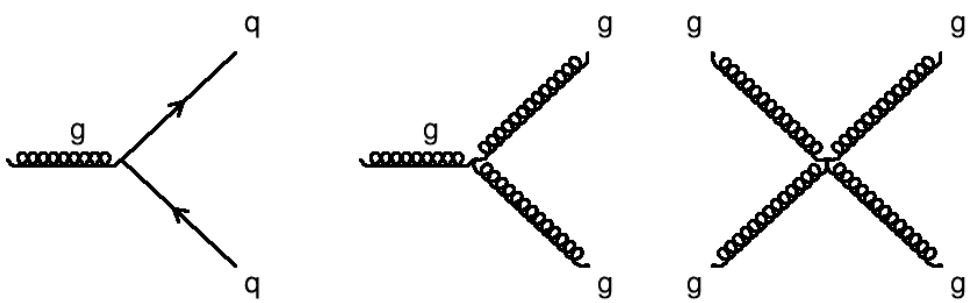

(a) (b) (c)

Figure 1.4: Examples of strong interactions.

antiparticles of each other, acting on left-handed particles and right-handed antiparticles only. They are involved in both neutrino and charged electron absorption and emission, causing nuclear transmutation. The Z boson has zero flavor quantum numbers and charges, so its exchange between particles is a neutral current that leaves the interacting particles unaffected except for their momentum.

- The gluons are massless $SU(3)$ vector gauge bosons that mediate the strong interaction between color charged particles (the quarks) as described by the theory of Quantum Chromodynamics. The eight gluons are labeled by combinations of color and anticolor charge. Because the gluons carry color charge, they can also interact among themselves.

The Higgs boson is a massive scalar particle with no spin, electric charge, or color charge. The masses of the fermions and weak bosons are generated by the Higgs boson. It explains why $W^{\pm}$ and Z bosons have mass when the gauge symmetries require them to be massless. The Higgs boson is very massive, decays almost immediately when created, and interacts with itself.

The Higgs can be produced in four ways:

- gluon fusion where two gluons combine to form a loop of virtual quarks;
- Higgs-strahlung in which a fermion collides with an anti-fermion to form a virtual W or Z boson and then, if that carries sufficient energy, a Higgs boson can be emitted;
- weak boson fusion where two fermions exchange a virtual W or Z boson, with a Higgs boson emitted;
- top fusion where two gluons each decay into a top pair, which combine to form a Higgs boson.

The observation of a standard model Higgs was announced by both ATLAS and CMS in 2012, with a measured mass of $126.0 \pm 0.4_{stat} \pm 0.4_{sys}$ GeV at ATLAS [6] and $125.3 \pm 0.4_{stat} \pm 0.5_{sys}$ GeV at CMS [7].

1.2 The B_c meson

The B_c meson is a bound state of $\bar{b}$ and c quarks. It is the only meson consisting of two heavy quarks with different flavors. Different from the charmonium and bottomonium systems, the $\bar{b}c$ system is expected to provide unique insight into heavy quark dynamics and therefore an important test of QCD. Because the masses of the b and c quark are large, the B_c can be used to test heavy-quark symmetries and better the next-to-leading terms in Heavy Quark Effective Theory.

Collaboration	$\sqrt{s}$(TeV)	B_c mass (GeV)
CDF [11]	1.96	$6.2756 \pm 0.0029_{stat} \pm 0.0025_{sys}$
D0 [14]	1.96	$6.300 \pm 0.014_{stat} \pm 0.005_{sys}$
CDF [9]	1.8	$6.4 \pm 0.39_{stat} \pm 0.13_{sys}$
LHCb [17]	7	$6.2737 \pm 0.0013_{stat} \pm 0.0016_{sys}$

Table 1.1: The B_c mass as measured by several experiments.

The B_c meson was first discovered by the Collider Detector at Fermilab (CDF) Collaboration [9] in $p\bar{p}$ collisions at $\sqrt{s} = 1.8$ TeV through its semi-leptonic decay $B_c \to J\psi l\nu$. It was confirmed by many other experiments using first the semi-leptonic decay $B_c \to J/\psi l\nu$ and then hadronic decays [14,18–20]. It has recently been reported by the LHCb and CMS experiments in the decay $B_c \to J\psi\pi\pi\pi$ [20,21]. Its mass and lifetime have been measured and are listed in Tables 1.1 and 1.2 with the latest world average values being $m(B_c) = (6274.5 \pm 1.8)$ MeV and $\tau = (0.452 \pm 0.033)$ ps [23].

Collaboration	$\sqrt{s}$ TeV	B_c lifetime (ps)
CDF [13]	1.96	$0.452 \pm 0.048 \pm 0.027$
D0 [15]	1.96	$0.448^{+0.038}_{-0.036} \pm 0.032$
CDF [12]	1.8	$0.463^{+0.073}_{-0.065} \pm 0.036$
CDF [9]	1.96	$0.46^{+0.18}_{-0.16} \pm 0.03$
LHCb [16]	8	$0.509 \pm 0.008 \pm 0.012$

Table 1.2: The B_c lifetime as measured by several experiments.

1.2.1 The mass spectrum of the B_c meson

Because the $\bar{b}c$ system carries flavor, it cannot annihilate into gluons. This makes the ground state quasi-stable with a width less than a hundred keV. The $\bar{b}c$ states have a rich spectrum of orbital and angular-momentum excitations (Figure 1.5 is an example from one model). Their masses are calculated via Lattice QCD, Non-relativistic QCD (NRQCD), and perturbative NRQCD (pNRQCD) models [24–40, 43].

Some typical predictions are listed in Tables 1.3 and 1.4. They show consistency among the potential models. One significant difference among them occurs in the Eichten-Quigg calculation [24], where the P states are almost pure $3P_1$ and $1P_1$ with little mixing, while in other models there is significant mixing. The latest prediction [27] is based on a relativistic quark model including the Coulomb plus linear potentials ($\sim$0.18 GeV^2) expected from QCD, the running coupling of QCD ($\alpha_s(Q^2)$), and relativistic effects, with uncertainty no less than 10 - 20 MeV due to the neglecting of coupled channel effects and simplifications in the relativization procedure.

As is shown in Figure 1.5, above the BD threshold, the $\bar{b}c$ states will decay into a $B - D$ pair, while below it those excited states which do not annihilate through strong interactions can only decay to the ground state by radiating photons or pion pairs. There are two sets of S wave states, two sets of P wave multiplets, and one D wave multiplet below the BD threshold.

1.2.2 Decays of the B_c meson

The B_c meson decays weakly though three different channels (Figure 1.6):

- The b-constituent decay with c as a spectator.
- The c-quark decay with the b quark as a spectator.
- The weak annihilation of the $\bar{b}$ and c to a W^+.

The total width is the sum over the partial widths:

$$\Gamma(B_c \to X) = \Gamma(\bar{b} \to X) + \Gamma(c \to X) + \Gamma(ann). \tag{1.1}$$

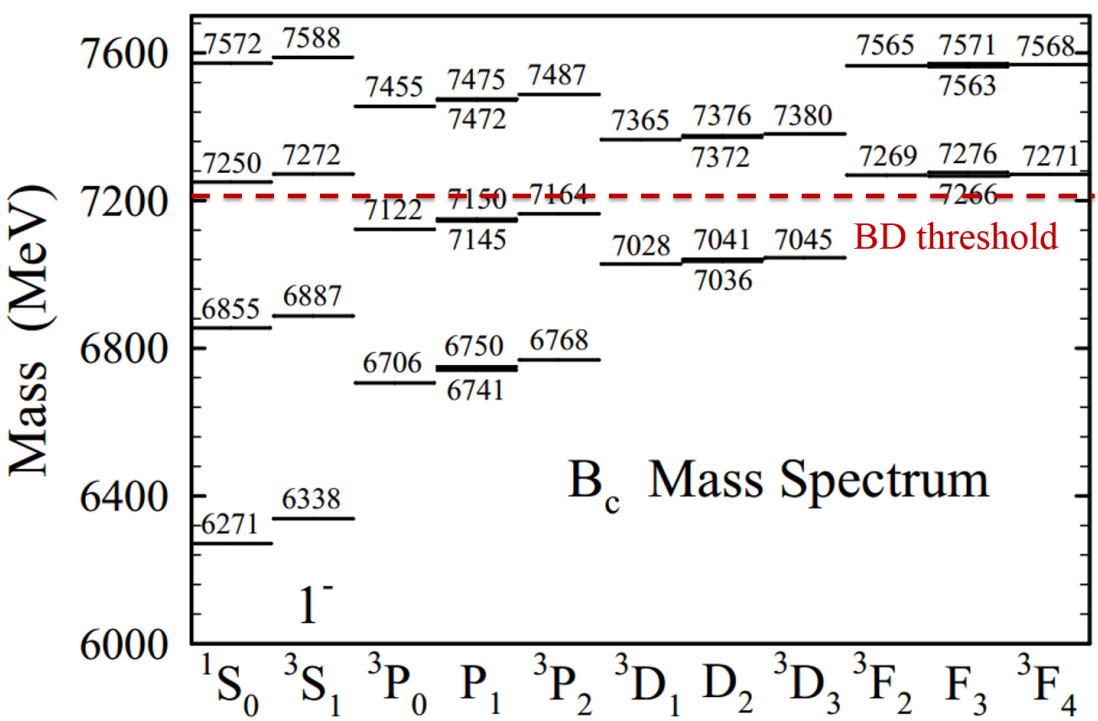

Figure 1.5: One example predicted B_c mass spectrum. The letter is the angular momentum (L) of the state; the number on the bottom right is the total momentum (J) of the state; the number on the top left is the spin ($2S+1$) of the state. [27]

State	GI[27]	EFG[36]	FUII[48]	GKLT[25]
1^3S_1	6338	6332	6341	6317
1^1S_0	6271	6270	6286	6253
1^3P_2	6768	6762	6772	6743
$1P_1'$	6750	6749	6760	6729
$1P_1$	6741	6734	6737	6717
1^3P_0	6706	6699	6701	6683
2^3S_1	6887	6881	6914	6902
2^1S_0	6855	6835	6882	6867
2^3P_2	7164	7156		7134
$2P_1'$	7150	7145		7124
$2P_1$	7145	7126		7113
2^3P_0	7122	7091		7088
3^3S_1	7272	7235		
3^1S_0	7250	7193		
1^3D_3	7045	7081	7032	7007
$1D_2'$	7036	7079	7028	7016
$1D_2$	7041	7077	7028	7001
1^3D_1	7028	7072	7019	7008
1^3F_4	7271			
$1F_3'$	7266			
$1F_3$	7276			
1^3F_2	7269			

Table 1.3: Predicted masses, in MeV, using different models. [27]

In the spectator approximation, the $\bar{b} \to X$ and $c \to X$ widths can be roughly calculated as:

$$\Gamma(\bar{b} \to X) = \frac{9G_F^2|V_{cb}|^2 m_b^5}{192\pi^3} \simeq 4.4 \times 10^{-4} \text{ eV} \tag{1.2}$$

and

$$\Gamma(c \to X) = \frac{5G_F^2|V_{cs}|^2 m_c^5}{192\pi^3} \simeq 3.6 \times 10^{-4} \text{ eV}, \tag{1.3}$$

where $|V_{cb}| = 0.0412$, $|V_{cs}| = 0.973$, $m_b = 4.18$ GeV, and $m_c = 1.275$ GeV [23].

State	EQ[24]	GJ[37]	ZVR[38]	Lattice[39]
1^3S_1	6337	6308	6340	6321 ± 20
1^1S_0	6264	6247	6260	$6280 \pm 30 \pm 190$
1^3P_2	6747	6773	6760	6783 ± 30
$1P_1'$	6736	6757	6740	6765 ± 30
$1P_1$	6730	6738	6730	6743 ± 30
1^3P_0	6700	6689	6680	6727 ± 30
2^3S_1	6899	6886	6900	6990 ± 80
2^1S_0	6856	6853	6850	6960 ± 80
2^3P_2	7153		7160	
$2P_1'$	7142		7150	
$2P_1$	7135		7140	
2^3P_0	7108		7100	
3^3S_1	7280		7280	
3^1S_0	7244		7240	
1^3D_3	7005		7040	
$1D_2'$	7009		7030	
$1D_2$	7012		7020	
1^3D_1	7012		7010	
1^3F_4			7250	
$1F_3'$			7250	
$1F_3$			7240	
1^3F_2			7240	

Table 1.4: Predicted B_c masses using different models [27]. The errors on the Lattice model are taken from [48].

For the annihilation decay, the width can be expressed as:

$$\Gamma(aan) = \frac{G_F^2}{8\pi}|V_{bc}|^2 f_{B_c}^2 M_{B_c} \sum_i m_i^2 (1 - \frac{m_i^2}{m_{B_c}^2})^2 C_i, \tag{1.4}$$

where $f_{B_c} \sim 400$ MeV.

A more detailed calculation [40] is given in the framework of the inclusive Operator Product Expansion (OPE) approach which is related to the small virtuality of the heavy quark in the bound state. This permits the general expansion of operators in inverse powers of heavy quark mass. It also yields the QCD sum rules where the

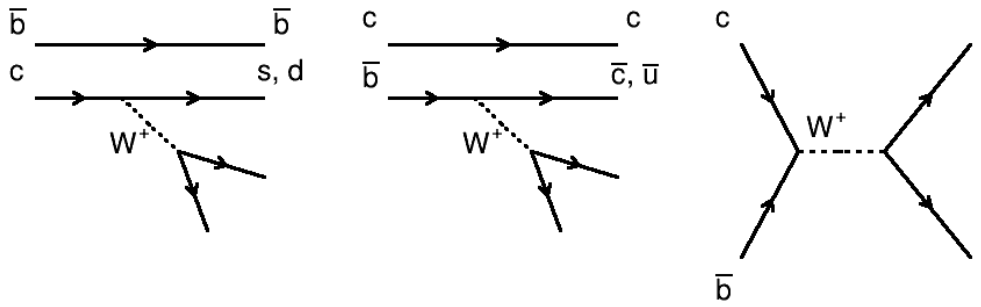

(a) (b) (c)

Figure 1.6: Three weak decay modes of the B_c. (a) The c-quark decay with the b quark as a spectator, (b) the b-constituent decay with c as a spectator, (c) the weak annihilation.

calculated total width is consistent with potential modes (PM):

$$\tau(B_c^+)_{OPE,pm} = 0.55 \pm 0.15 \text{ ps}, \tag{1.5}$$

as well as the semi-inclusive calculations in the sum rules of QCD and NRQCD where the calculated total width is:

$$\tau(B_c^+)_{SR} = 0.48 \pm 0.05 \text{ ps}. \tag{1.6}$$

Both are consistent with the measured lifetime $\tau = 0.452 \pm 0.033$ ps. The branching ratios predicted are summarized in Table 1.5.

On the basis of its final state particles, the B_c's decays can be classified into three types:

- Semi-leptonic, where the B_c decays to $c\bar{c}$, a charmed meson, or another bottom meson, plus a lepton and neutrino. This decay mode has the largest branching ratio predicted.
- Leptonic, where $B_c^+ \to \tau^+\nu_\tau$. This mode has a low experimental efficiency of detection because of the hadronic background to the τ decays and the missing energy of the undetectable neutrino.

B_c decay mode	OPE, %	PM, %	SR, %
$b \to \bar{c}l^+\nu_l$	3.9 ± 1.0	3.7 ± 0.9	2.9 ± 0.3
$\bar{b} \to \bar{c}u\bar{d}$	16.2 ± 4.1	16.7 ± 4.2	13.1 ± 1.3
$\sum \bar{b} \to \bar{c}$	25.0 ± 6.2	25.0 ± 6.2	19.6 ± 1.9
$c \to sl^+\nu_l$	8.5 ± 2.1	10.1 ± 2.5	9.0 ± 0.9
$c \to su\bar{d}$	47.3 ± 11.8	45.4 ± 11.4	54.0 ± 5.4
$\sum c \to s$	64.3 ± 16.1	65.6 ± 16.4	72.0 ± 7.2
$B_c^+ \to \tau^+\nu_\tau$	2.9 ± 0.7	2.0 ± 0.5	1.8 ± 0.2
$B_c^+ \to c\bar{s}$	7.2 ± 1.8	7.2 ± 1.8	6.6 ± 0.7

Table 1.5: The branching ratios of the B_c decay modes calculated in the framework of the inclusive OPE approach, by summing up the exclusive modes in the potential model, and according to semi-inclusive estimates in the sum rules of QCD and NRQCD.[40]

- Hadronic, where the B_c decays to hadrons only.

The most easily observed decay product of the B_c is the J/ψ because its decay to $\mu^+\mu^-$ has little background. The semi-leptonic decay $B_c \to J/\psi\mu\nu$ has the largest branching ratio (1.9%) and thus it was the first decay channel observed. The hadronic decay mode $B_c \to J/\psi\pi$ is used in this analysis as it can be fully reconstructed.

Mode	BR, %
$B_c^+ \to J/\psi l^+\nu_l$	1.9
$B_c^+ \to J/\psi\pi$	0.13
$B_c^+ \to J/\psi\pi\pi$	0.35
$B_c^+ \to J/\psi\pi\pi\pi$	0.52
$B_c^+ \to J/\psi\pi\pi\pi\pi$	0.26
$B_c^+ \to J/\psi\rho$	0.38
$B_c^+ \to J/\psi K^+$	0.011
$B_c^+ \to J/\psi K^{*+}$	0.022
$B_c^+ \to J/\psi D_s^+$	0.17
$B_c^+ \to J/\psi D_s^{*+}$	0.67
$B_c^+ \to J/\psi D^+$	0.009
$B_c^+ \to J/\psi D^{*+}$	0.028

Table 1.6: The branching ratios of the $B_c \to J/\psi X$ channels.[40, 41]

In addition to the $\pi l\nu$ final state, ρ, multi-pions, and kaons are also possible products. Some of the predicted branching ratios of the $B_c \to J/\psi X$ channels are summarized in Table 1.6. The uncertainties are typically as large as 50%[40,41]. The $B_c^+ \to J/\psi\pi\pi\pi$ channel was recently observed by LHCb with measured branching ratio relative to $B_c^+ \to J/\psi\pi$ of $2.41 \pm 0.30 \pm 0.33$ [21]. This has been confirmed by CMS [20].

As is shown in Tables 1.3 and 1.4, the mass difference between the lowest vector 1^3S_1 (B_c^*) and pseudoscalar 1^1S_0 (B_c) states is quite small ($\sim$70 MeV). To be able to observe the γ from the B_c^* decay to the B_c, the transverse momentum of the B_c^* needs to be larger than 24 GeV. Applying a selection requirement at $p_{\rm T} > 24$ GeV would decrease the B_c yield by 2 orders of magnitude.

The P wave states (Table 1.7) can contribute 10-20% of the total B_c yield. Among them, 20% emit one photon, immediately transforming to the lowest (1^1S_0) state via either of the processes:

$$\begin{aligned} 2P_1(B_c) &\xrightarrow[\sim 13\%]{\gamma} 1^1S_0(B_c), \\ 2P_1^{'}(B_c) &\xrightarrow[\sim 94\%]{\gamma} 1^1S_0(B_c). \end{aligned} \tag{1.7}$$

In all other cases, a $2P$ state first decays to a 1^3S_1 state by emitting a hard photon, and then decays to 1^1S_0 by emitting a soft photon:

$$2P \xrightarrow{\gamma^{\rm hard}} 1^3S_1(B_c^*) \xrightarrow{\gamma^{\rm soft}} 1^1S_0(B_c). \tag{1.8}$$

The excited B_c states which decay hadronically are listed in Table 1.8. Both $2S$ and $1D$ states can decay directly to the B_c. The yield of $2S$ is about 10-35% of the total B_c meson yield, and more than half of them decay to B_c (B_c^*) plus a $\pi^+\pi^-$ pair:

$$2^1S_0(B_c) \xrightarrow[\sim 50-90\%]{\pi^+\pi^-} 1^1S_0(B_c), \tag{1.9}$$

$$2^3S_1(B_c) \xrightarrow[\sim 40-80\%]{\pi^+\pi^-} 1^3S_1(B_c). \tag{1.10}$$

Initial state	Final state	BR, %	ΔM, MeV
2^3P_0	$1^3S_1+\gamma$	100	363-366
$2P1^+$	$1^3S_1+\gamma$	87	393-400
	$1^1S_0+\gamma$	13	393-400
$2P1'^+$	$1^1S_0+\gamma$	94	472-476
	$1^3S_1+\gamma$	6	472-476
2^3P_2	$1^3S_1+\gamma$	100	410-426
3^3P_0	$1^3S_1+\gamma$	2	741
$3P1^+$	$1^3S_1+\gamma$	8.5	761
	$1^1S_0+\gamma$	3.3	820
$3P1'^+$	$1^1S_0+\gamma$	22.6	825
	$1^3S_1+\gamma$	0.7	769
3^3P_2	$1^3S_1+\gamma$	18	778

Table 1.7: Branching ratio (BR) and mass differences (ΔM) of radiative decays of B_c meson P-wave excitations [27, 37, 40].

The ratios of the production cross sections are:

$$\sigma(B_c(2S))/\sigma^{total}(B_c) \sim 10-35\% \tag{1.11}$$

and

$$\sigma(2^3S_1)/\sigma(2^1S_0) \sim 2-3. \tag{1.12}$$

Thus, the yield of $2S$ excitations followed by a $B_c(2S) \to B_c(B_c^*)+\pi^+\pi^-$ decay may be up to 10-35% of the total B_c meson yield. The mass difference between the 1^3S_1 state and 1^1S_0 state is approximately 65 MeV which results in about 10 MeV shift in the energy detected in the decay to the ground state. Furthermore, the mass difference between the 2^3S_1 state and the 2^1S_0 state is approximately 30 MeV. This results in an about 30 MeV negative shift in the $B_c+\pi\pi$ mass.

1.2.3 Production of the B_c meson

The B_c production cross section has been measured at CDF through its decay channel $B_c \to J/\psi l\nu$ relative to $B^+ \to J/\psi K$. This is listed in Table 1.9 [9,22]. At LHCb, the

State	Decay mode	BR, %	ΔM, MeV
2^3S_1	$1^3S_1 + \pi\pi$	88.1	549-669
2^1S_0	$1^1S_0 + \pi\pi$	79.6	565-680
2^3P_2	$1^3P_2 + \pi\pi$	1.3	391-406
$2P_1'$	$1P_1' + \pi\pi$	1.4	395-406
$2P_1$	$1P_1 + \pi\pi$	4.0	392-410
2^3P_0	$1^3P_0 + \pi\pi$	2.1	392-420
$1^3D_{1,3}$	$1^3S_1 + \pi\pi$	5.2	675-749
$1D_2'$	$1^3S_1 + \pi\pi$	2.5	672-747
	$1^1S_0 + \pi\pi$	2.6	742-765
$1D_2$	$1^3S_1 + \pi\pi$	2.4	675-745
	$1^1S_0 + \pi\pi$	2.3	742-807

Table 1.8: Branching ratio (BR) and mass differences (ΔM) of the hadronic transitions of the excited B_c states [27].

same relative production cross section has been measured for different kinematical conditions, as $(2.2 \pm 0.8 \pm 0.2)\%$, for the range $p_{\mathrm{T}} > 4$ GeV and $2.5 < \eta < 4.5$ [18].

$\mathscr{L}$, pb^{-1}	p_{T}(B), GeV	$\mathscr{R}$, %
110	6	$0.132^{+0.041}_{-0.037} \pm 0.031^{+0.032}_{-0.020}$
1000	4	$0.295 \pm 0.040^{+0.033}_{-0.026} \pm 0.036$
1000	6	$0.227 \pm 0.033^{+0.024}_{-0.017} \pm 0.014$

Table 1.9: The ratio of relative production cross sections for decay channels $B_c \to J/\psi l\nu$ and $B^+ \to J/\psi K$ measured by CDF. [9, 22]

The $\bar{b}c$ production mechanism, unlike the $b\bar{b}$, requires two heavy quark-antiquark pairs to be created in a collision. The hard associated production of two heavy pairs $c\bar{c}$ and $b\bar{b}$ determines the B_c production rate. Also important is the soft nonperturbative binding of nonrelativistic quarks in the color-singlet state which can be described in the framework of potential models. The B_c yield is suppressed by a factor on the order of 10^{-3} with respect to beauty hadrons, for which the production cross section is about 10^6 nb at the LHC (Figure 1.7). Unlike production of quarkonium (with hidden flavor), the production of B_c P wave states is suppressed

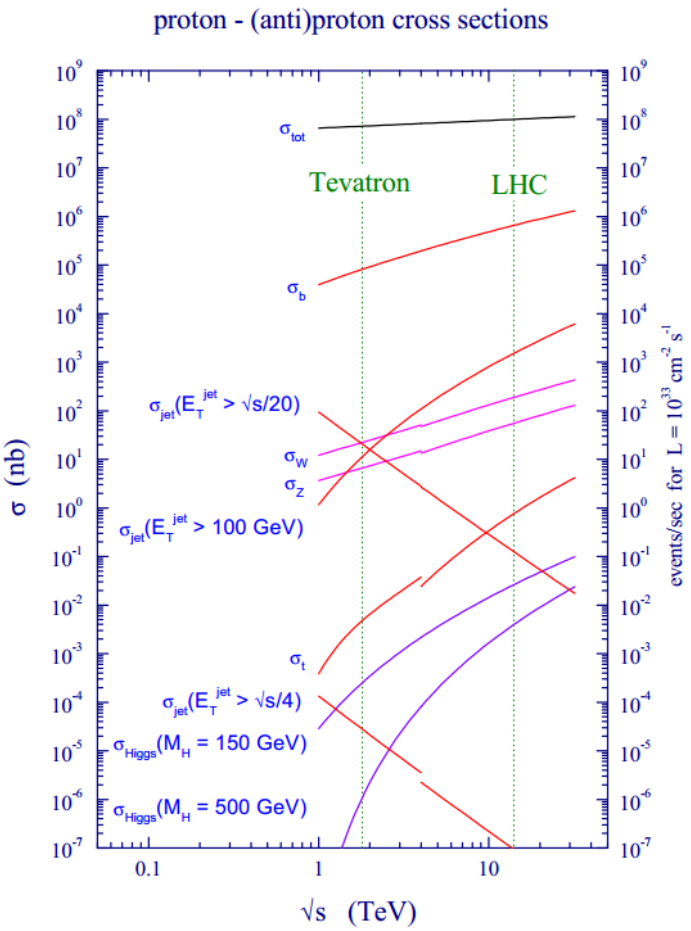

Figure 1.7: Various Standard Model hadronic production cross sections as a function of center of mass energy. [44]

compared to S wave states. B_c meson production is a significant product of b quark fragmentation only at high transverse momenta, $p_{\mathrm{T}} > 35$ GeV. The ratio of cross sections for production of the vector state B_c^* and the pseudoscalar state is predicted to be $R(B_c) = \sigma(B_c^*)/\sigma(B_c) = 1.4$. This is unlike the result for the B mesons, where $R(B) = 3$ at high transverse momentum and $R(B) \sim 2.6$ at low transverse momentum. There is a large non-fragmentation contribution to this process. The non-fragmentation terms in the production amplitude increase the total cross section and change the ratio between yields of B_c and its excited states for large transverse

momentum.

Calculations of the hadronic production of different B_c spin states are based on the factorization of hard parton production of heavy quarks ($b\bar{b}c\bar{c}$) and soft coupling of the $\bar{b}c$ bound state. The hard subprocess can be reliably calculated in the framework of QCD perturbation theory, while the quark binding in the heavy quarkonium can be described by the nonrelativistic potential model in the $\bar{b}c$ rest system.

The cross section calculation technique, the matrix elements, and the gluonic production implemented in the Monte Carlo (MC) generator for the B_c meson are described below [52]. This is based on the theoretical calculations in [42].

The production amplitude can written as

$$A^{SJj_z} = \int T^{Ss_z}_{b\bar{b}c\bar{c}}(p_i, k(\vec{q})) \cdot (\Psi^{Ll_z}_{\bar{b}c}(\vec{q}))^* \cdot C^{Jj_z}_{s_z l_z} \frac{d^3\vec{q}}{(2)^3}, \tag{1.13}$$

where $T^{Ss_z}_{b\bar{b}c\bar{c}}$ is the amplitude for hard production of two heavy quark pairs, $\Psi^{Ll_z}_{\bar{b}c}$ is the quarkonium wave function, J and j_z are the total angular momentum and its projection onto the z axis in the B_c rest frame, L and l_z are the orbital angular momentum of the B_c meson and its projection onto the z axis, S and s_z are the B_c spin and its projection, the $C^{Jj_z}_{s_z l_z}$ are Clebsch-Gordon coefficients, the p_i are the four-momenta of the B_c meson, b quark, and $\bar{c}$ quark, and $\vec{q}$ is the three-momentum of the $\bar{b}$ quark in the B_c rest frame (in this frame $(0, \vec{q}) = k(\vec{q})$). The four momentum of the $\bar{b}$ and c quarks can be determined by the following formula with precision up to $|\mathbf{q}|^2$:

$$\begin{aligned} p_{\bar{b}} &= \frac{m_b}{M} P_{B_c} + k(\mathbf{q}), \\ p_c &= \frac{m_c}{M} P_{B_c} - k(\mathbf{q}), \end{aligned} \tag{1.14}$$

where m_b and m_c are the quark masses, $M = m_b + m_c$, and P_{B_c} is the B_c momentum. For the S wave state it is enough to take into account only the $\mathbf{q} = 0$ term in Eq. 1.13. Linear terms in $\mathbf{q}$ are necessary in the P wave production calculation.

The S wave production amplitude can be written as

$$A^{Ss_z} = iR_S(0)\sqrt{\frac{2M}{2m_b 2m_c}}\sqrt{\frac{1}{4\pi}}(T^{Ss_z}(p_i, k(\mathbf{q}=0))), \tag{1.15}$$

where $R_S(0)$ is the radial wave function at the origin,

$$R_S(0) = \sqrt{\frac{\pi}{3}}\tilde{f}_{B_c}. \tag{1.16}$$

The estimated $\tilde{f}_{B_c}$ value for the potential models is $\tilde{f}_{B_c} = 500 \pm 100$ MeV [24, 25]. The QCD sum rule estimation for the 1^1S_0 state gives $\tilde{f}_{B_c} = 385 \pm 25$ MeV [29], which is in good agreement with the lattice computations where $\tilde{f}_{B_c} = 395 \pm 2$ MeV [34].

The P wave production amplitude can be written as

$$A^{SJj_z} = iR'_P(0)\sqrt{\frac{2M}{2m_b 2m_c}}\sqrt{\frac{3}{4\pi}}C^{Jj_z}_{s_z l_z}\mathscr{L}^{l_z}(T^{Ss_z}(p_i, k(\mathbf{q}=0))), \tag{1.17}$$

where $R'_P(0)$ is the first derivative of the radial wave function at the origin, and $\mathscr{L}^{l_z}$ has the following form:

$$\begin{aligned} \mathscr{L}^{-1} &= \frac{1}{\sqrt{2}}(\frac{\partial}{\partial q_x} + i\frac{\partial}{\partial q_y}), \\ \mathscr{L}^{0} &= \frac{\partial}{\partial q_z}, \\ \mathscr{L}^{+1} &= -\frac{1}{\sqrt{2}}(\frac{\partial}{\partial q_x} - i\frac{\partial}{\partial q_y}), \end{aligned} \tag{1.18}$$

where $\frac{\partial}{\partial q_x}$, $\frac{\partial}{\partial q_y}$, and $\frac{\partial}{\partial q_z}$ are differential operators acting on $T^{Ss_z}(p_i, k(\mathbf{q}))$ as a function of $\mathbf{q} = (q_x, q_y, q_z)$ at $\mathbf{q} = 0$.

The matrix element A^{SJj_z} squared, which is calculated as described above, has to be summed over j_z as well as over the spin states of the free b and $\bar{c}$ quarks. It must be averaged over the spin projections of the initial particles.

About 90% of B_c mesons at the LHC are produced by gluon-gluon fusion $gg \to B_c^+ + b + \bar{c}$. The process is described by 38 diagrams at fourth order in α_s. In diagram

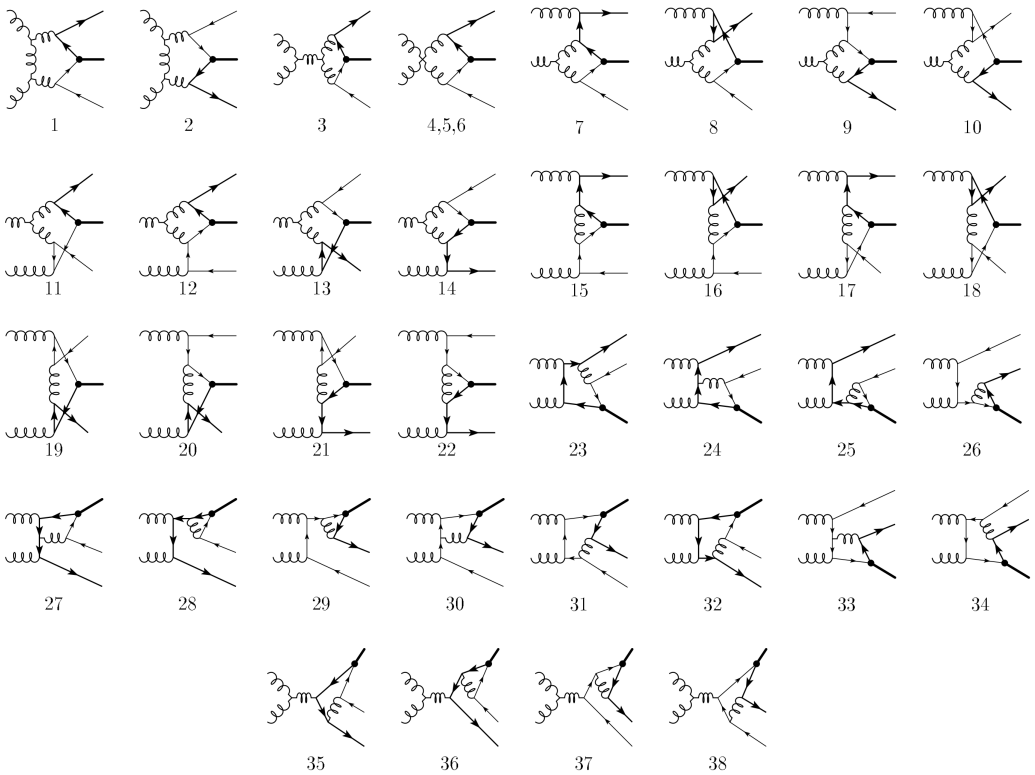

Figure 1.8: The leading order diagrams for the process $gg \to B_c^+ + b + \bar{c}$. [52]

1 of Figure 1.8, the initial gluons exchange a gluon in the t-channel and split into quark-antiquark pairs. The color part can be written as

$$T_1 = -\frac{3}{2} t^{g_2}_{ck} t^{g_1}_{k\bar{b}} - \frac{1}{4} \delta^{g_1 g_2} \delta_{c\bar{b}}. \tag{1.19}$$

The term $\delta^{g_1 g_2} \delta_{c\bar{b}}$ corresponds to the production of a c quark and a $\bar{b}$ quark in a color singlet. A color string connects these two quarks. The term $t^{g_2}_{ck} t^{g_1}_{k\bar{b}}$ contains a singlet part as well:

$$t^a t^b = \frac{1}{6} \delta^{ab} + \frac{1}{2} (d^{abc} + i f^{abc}) t^c. \tag{1.20}$$

The two different singlet hadronization processes can be treated as separate contributions to the color flow. The unrealized color flows would be composed of two color octet states d and f.

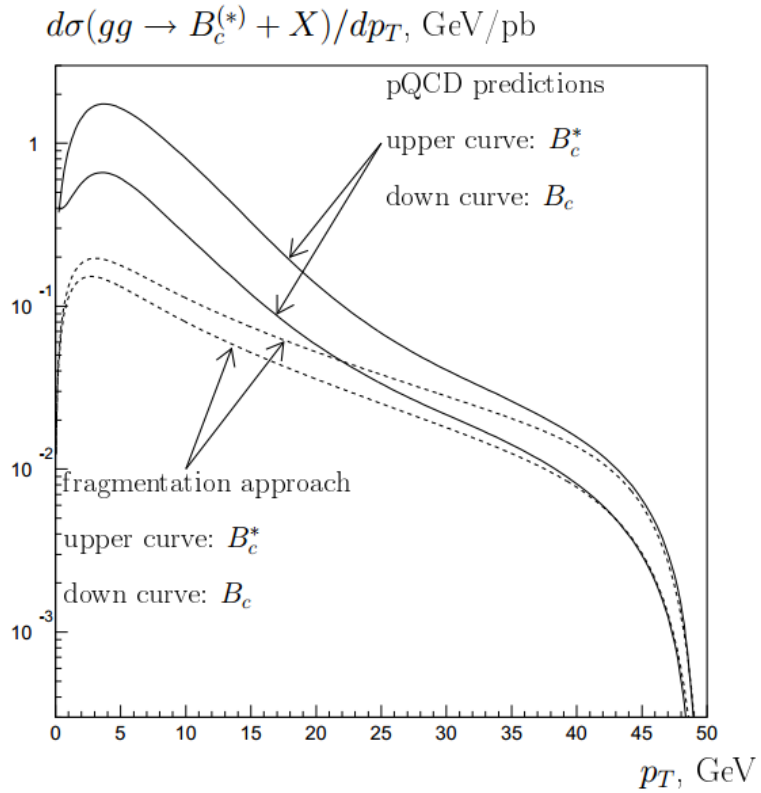

Figure 1.9: Predicted cross section distribution versus transverse momentum for B_c gluonic production at interaction energy $\sqrt{s_{gg}} = 100$ GeV, obtained within pQCD and with the fragmentation model prediction. [52]

Figure 1.9 shows that the fragmentation approach is valid only at transverse momenta larger than 5 to 6 times the B_c mass. The total gluonic cross section is predicted using the full set of leading order diagrams. This result differs from the fragmentation approach prediction in absolute value as well as in the shape of the interaction energy dependence (Figure 1.10). Incorrect phase space counting in the fragmentation approach enhances the fragmentation predictions near the threshold.

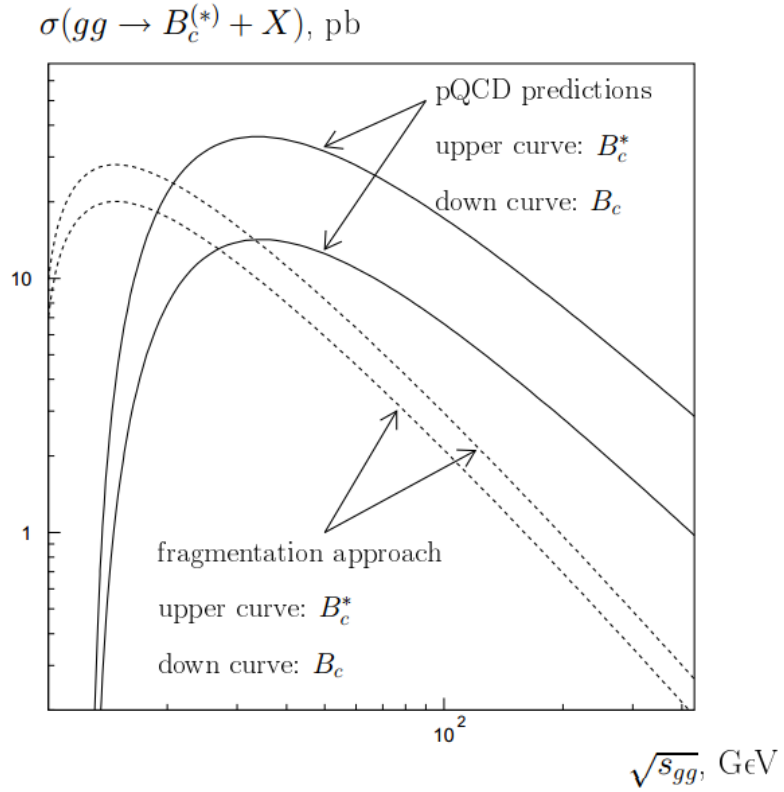

Figure 1.10: Predicted cross section distribution versus interaction energy for gluonic B_c production. [52]

1.3 The B^+ meson

The $B^+ \to J/\psi K^+$ channel has the same topology as the $B_c \to J/\psi\pi$ channel. The B^+ has about a 10^3 times higher production cross section, compared to the B_c, which allows it to be reconstructed with high accuracy. Thus it can be used as a cross check channel in this analysis. The fitted B^+ peak is used as a baseline measurement of the detector resolution, mass bias, and various uncertainty calculations including the mass bias introduced by the momentum scale. The B^+ production cross section has been well measured [53] over a wide p_{T} range by ATLAS and found to agree well with theoretical predictions (Figure 1.11).

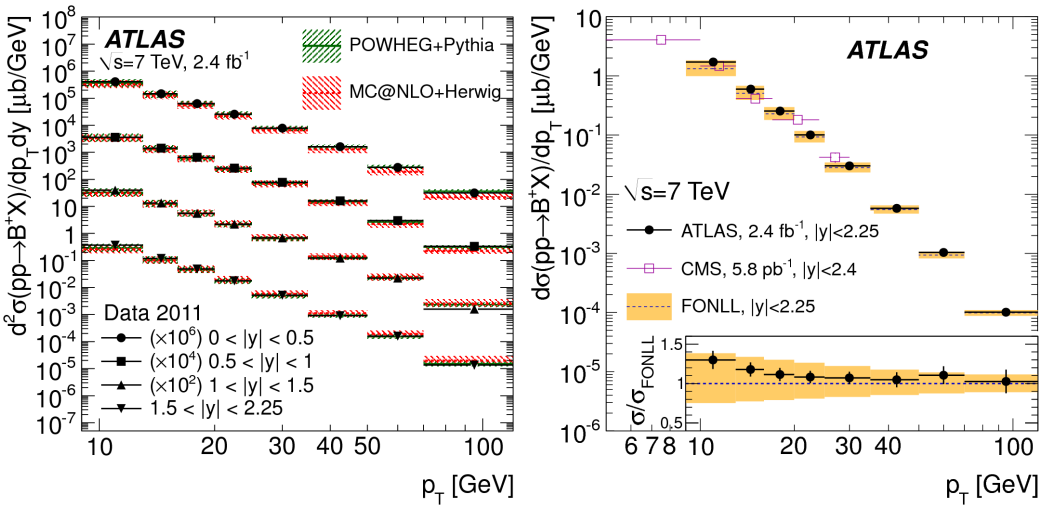

(a) (b)

Figure 1.11: (a) The doubly-differential cross-section for B^+ production as a function of p_{T} and y, averaged over each (p_{T}, y) interval and quoted at its center. The data points are compared to NLO predictions from POWHEG and MC@NLO. The shaded areas around the theoretical predictions reflect the uncertainty from renormalization and factorization scales and the b-quark mass. The ratio of the measured cross-section to the theoretical predictions ($\sigma/\sigma_{\mathrm{NLO}}$) of POWHEG and MC@NLO in eight p_{T} intervals in four rapidity ranges is shown. The points with error bars correspond to data with their associated uncertainties, which is the combination of the statistical and systematic uncertainty. The shaded areas around the theoretical predictions reflect the uncertainty from renormalization and factorization scales and the b-quark mass. (b) The differential cross-section for B^+ production versus p_{T}, integrated over rapidity. The solid points with error bars correspond to the differential cross-section measurement by ATLAS with total uncertainty (statistical and systematic) in the rapidity range $|y| < 2.25$, averaged over each p_{T} interval and quoted at its center. For comparison, data points from CMS are also shown, for a measurement covering $p_{\mathrm{T}} < 30$ GeV and $|y| < 2.4$ [54]. Predictions of the FONLL calculation for b-quark production are also compared with the data, assuming a hadronization fraction $f_{b\to B^+}$ of $(40.1 \pm 0.8)\%$ [62] to fix the overall scale. Also shown is the ratio of the measured cross-section to the predictions by the FONLL calculation ($\sigma/\sigma_{\mathrm{FONLL}}$). The upper and lower uncertainty limits on the prediction were obtained by considering scale and b-quark mass variations. [53]

Chapter 2

Overview of the ATLAS experiment

This chapter describes the main features of the Large Hadron Collider (LHC) and the ATLAS (A Toroidal LHC ApparatuS) experiment, one of the two general-purpose detectors at the LHC.

2.1 The Large Hadron Collider

The LHC [57] at the European Organization for Nuclear Research (CERN) is a two ring superconducting hadron accelerator that began operation on 10 September 2008. The LHC is a proton-proton (pp) collider, designed to reach a maximum center-of-mass energy of $\sqrt{s} = 14$ TeV and a maximum instantaneous luminosity of $10^{34}\text{cm}^{-2}\text{s}^{-1}$. It can also collide heavy (Pb) ions with an energy of 2.8 TeV per nucleon and a peak luminosity of $10^{27}\text{cm}^{-2}\text{s}^{-1}$. During the 2011 run, the LHC operated at a center of mass energy ($\sqrt{s}$) of 7 TeV with one bunch crossing per 50 ns. During the 2012 run, the LHC operated at $\sqrt{s} = 8$ TeV with one bunch crossing per 25 ns.

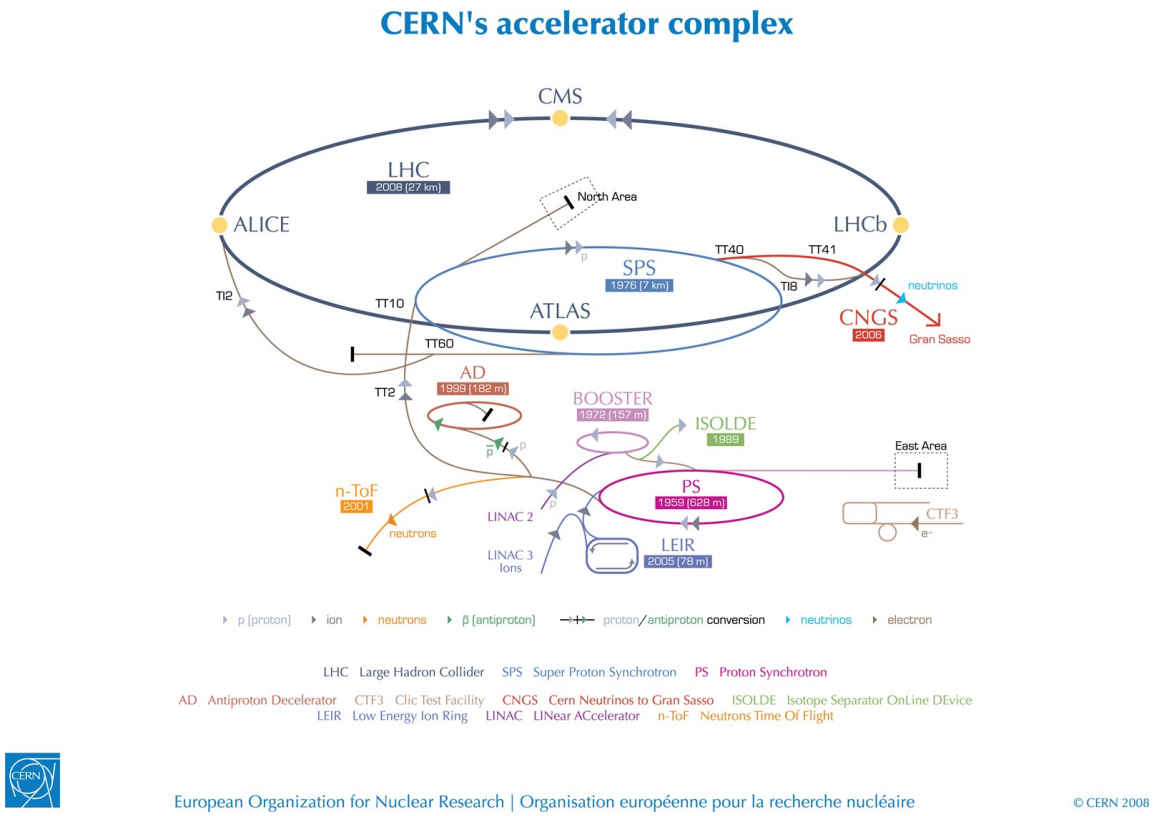

Figure 2.1: The accelerator complex of CERN. [65]

The LHC is part of CERN's complex of accelerators, shown in Figure 2.1, located near Geneva, at the border between France and Switzerland. It is installed in the 26.7 km tunnel that was constructed between 1984 and 1989 for the CERN Large Electron Positron (LEP) Collider. The protons are acquired by stripping electrons from hydrogen atoms. They are accelerated by a linear accelerator (Linac2) to 50 MeV, then injected into the Proton Synchrotron Booster (PSB) ring to be accelerated to 1.4 GeV before being sent to the Proton Synchrotron (PS). The energy of both beams is increased to 25 GeV in the PS and boosted to 450 GeV before they are finally transferred to the LHC. The ring includes eight superconducting radio-frequency (RF) cavities, each delivering 2 MV at 400 MHz and operated at 4.5 K. There are 1232 superconducting dipole magnets, providing a total magnetic field of 8.3 T and

operated at 1.9 K.

The beams collide at four interaction points, where the four main experiments, ATLAS, CMS, LHCb, and ALICE, are installed. The largest two, ATLAS and CMS, are general purpose detectors. ALICE studies heavy-ion collisions using dedicated runs of the LHC and focuses on the physics of the strong interaction and the quark gluon plasma at extreme values of energy density and temperature. LHCb is a forward detector specializing in precision measurements of CP violation and rare decays of b-hadrons as well as the search for indirect evidence of new physics in these processes.

2.2 The ATLAS detector

The ATLAS detector [58] is 44 m in length, 25 m in diameter, and about 7000 tons in weight. It covers almost the full solid angle around the interaction point (IP). It is designed for a large range of particle physics studies. These include measurements of Standard Model processes and searches for Higgs bosons or other signatures of new physics.

The detector includes several sub-detector systems (Figure 2.2): the inner detector for charged particle tracking; the electromagnetic and hadronic calorimeters for energy measurement; and the muon spectrometer.

The coordinate system of ATLAS defines the nominal interaction point as the origin. The beam direction is the z-axis and transverse to the beam direction is the x-y plane. The positive x-axis is defined to be pointing from the interaction point to the center of the LHC ring, and the positive y-axis is defined to be pointing upwards. Side-A of the detector is defined to be that with positive z, and side-C is that with negative z. The azimuthal angle ϕ is measured around the beam axis, and

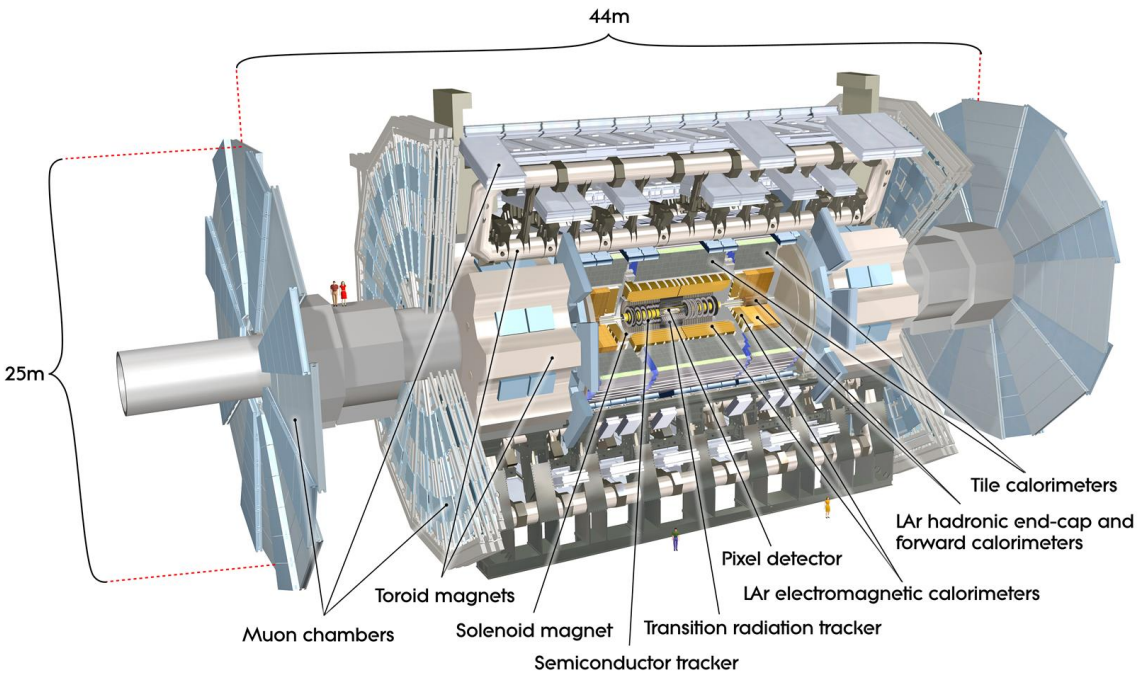

Figure 2.2: The ATLAS detector. [67]

the polar angle θ is the angle from the beam axis. The pseudorapidity is defined as $\eta = -\ln\tan(\theta/2)$, and the distance between two physical objects ΔR in the $\eta - \phi$ plan is defined as $\Delta R = \sqrt{\Delta\eta^2 + \Delta\phi^2}$. [58]

2.2.1 Inner Detector

The ATLAS Inner Detector (ID) (Figure 2.3) is designed to achieve high precision measurements of charged particle momentum. It is about 6 m in length and 2 m in diameter, and it covers a pseudorapidity of $|\eta| \leq 2.5$ with momentum resolution $\sigma_{p_T}/p_T = 0.05\% p_T \oplus 1\%$. The whole ID is immersed in a 2 T magnetic field generated by the central solenoid. The ID includes the pixel detector (PIX), the semiconductor tracker (SCT), and the transition radiation tracker (TRT) in both the barrel and the

endcap regions (Figure 2.4).

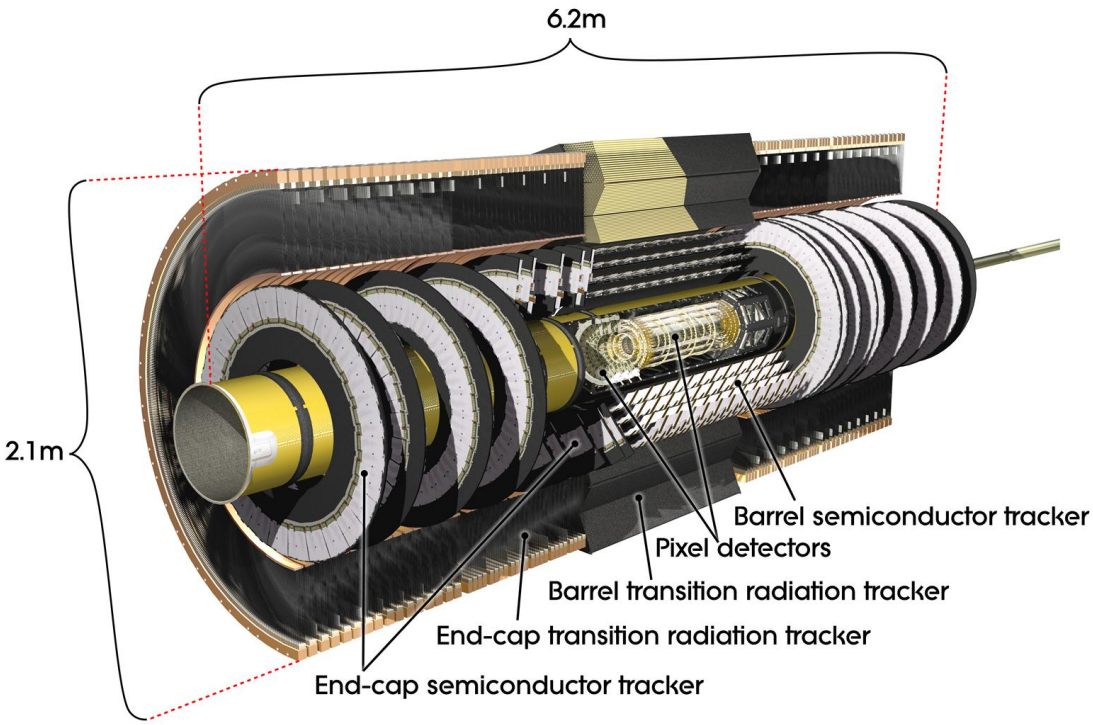

Figure 2.3: The ATLAS Inner Detector. [67]

The Pixel detector

The Pixel detector is located next to the beam pipe to achieve the best possible vertex region. It makes precision measurements of the vertex and trajectories of charged particles as close to the interaction point as possible. It has 3 layers in the barrel and 3 disks in the endcap on each side. All of the pixel sensors are identical n-in-n silicon sensors; the pixel dimensions are 50 μm in $R-\phi$ and 400 μm in z. There are approximately 80.4 million readout channels in total. The precisions in the barrel are 10 μm in $R-\phi$ and 110 μm in z, while in the disks they are 10 μm in $R-\phi$ and 110 μm in R.

The SCT

The SCT is located in the intermediate radial range, where is makes precision measurements of the charged particle momentum, impact parameter, and vertex position by providing eight precision measurements per track. It has 8 layers in the barrel, instrumented at 4 radial points (two layers at the same radial point), and 9 disks in each endcap. All of the SCT sensors are identical p-in-n silicon sensors. The SCT has a set of strips running radially and a set of small angle stereo strips which each cover 40 mrad. There are approximately 6.3 million readout channels in total. The precisions in the barrel are 17 μm in $R-\phi$ and 580 μm in z, while in the disks they are 17 μm in $R-\phi$ and 580 μm in R.

The TRT

The TRT covers the large outer range of the ID. It contributes to pattern recognition and electron identification by its very large number of dense hits provided by the 4 mm diameter straw tubes. It provides information in $R-\phi$ with a precision of 130 μm per straw for charged particle tracks with $\mid \eta \mid < 2.5$ and $p_{\mathrm{T}} > 0.5$ GeV.

2.2.2 Calorimeter

The ATLAS calorimeters (Figure 2.5) are designed for electromagnetic and hadronic shower reconstruction and precise missing transverse energy (E_T^{miss}) measurement within the pseudorapidity range $|\eta| \leq 4.9$. Two calorimeters are instrumented, the Electromagnetic Calorimeter and the Hadronic Calorimeter.

The Electromagnetic (EM) Calorimeter is suited for precision energy measurement of electrons, photons, E_T^{miss}, and jet reconstruction. It includes a presampler detector ($|\eta| < 1.8$) for correction of the energy lost by electrons and photons up-

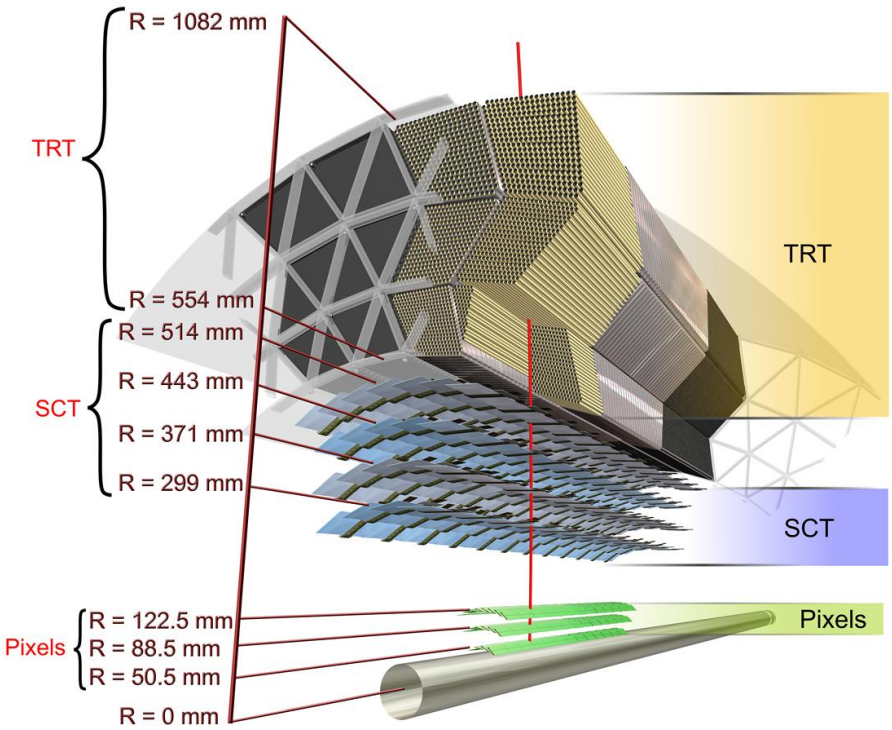

Figure 2.4: The cross section of the Inner Detector. [67]

stream, and a Liquid Argon (LAr) detector using lead as the absorber material and LAr as the active material. The EM calorimeter spans the range of $|\eta| < 3.2$. It contains two identical half-barrels separated by a gap of 4 mm at z_0 with $|\eta| < 1.475$ and two coaxial wheels in each endcap with $1.375 < \eta < 3.2$. The overall resolution of the EM Calorimeter is $\sigma_{\mathrm{E}}/E = 10\%\sqrt{E} \oplus 0.7\%$.

The Hadronic Calorimeter (HC) is suited for recording the energy of hadrons such as protons, neutrons, and mesons within the range of $|\eta| \leq 4.9$. Similar to the EM calorimeter, it detects the particle shower and reconstructs the energy loss. Unlike EM showers, hadronic showers are characterized by their interaction length. The

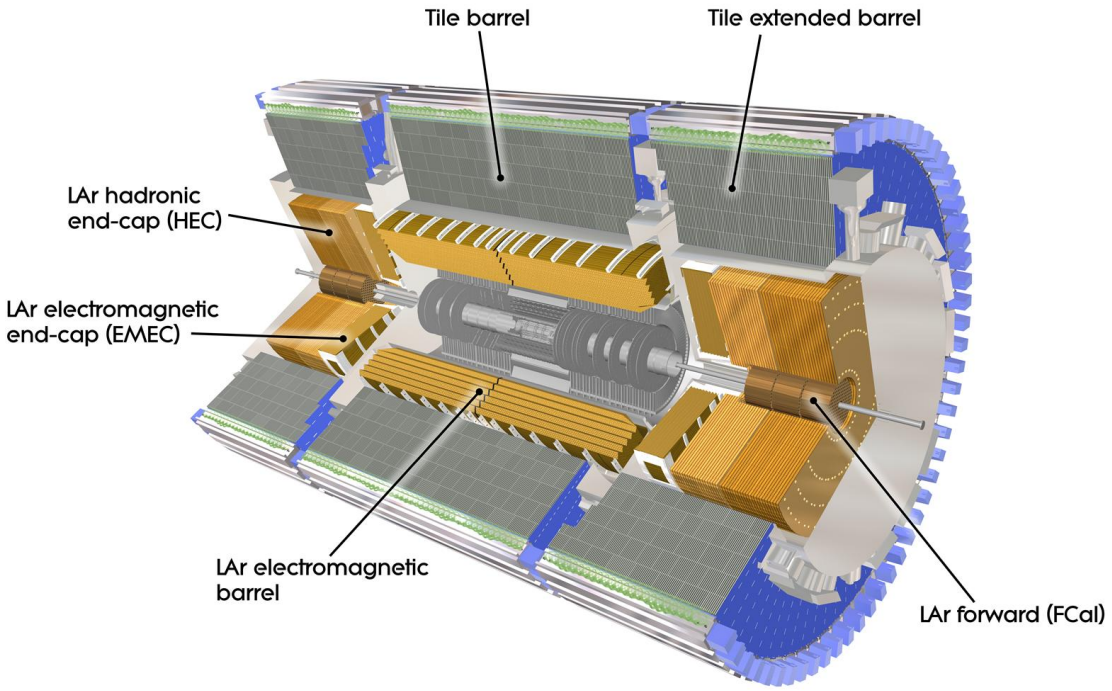

Figure 2.5: The Electromagnetic Calorimeter and Hadronic Calorimeter in ATLAS. [67]

Hadronic Calorimeter is designed to be dense and thick to limit punch-through into the muon system. There are three main components of the Hadronic Calorimeter: (1) the tile calorimeter with a barrel covering $|\eta| \leq 1.0$ plus two extended barrels in the $0.8 < \eta < 1.7$ regions. It uses fiber photomultipliers which point towards the interaction region; (2) the hadron endcap calorimeter ($1.5 < \eta < 3.2$) with two independent wheels constructed from 25 mm parallel copper plates in each endcap, located directly behind the endcap electromagnetic calorimeter and sharing the same LAr cryostats; and (3) the forward calorimeter with three modules in each endcap constructed from a metal matrix, with regularly spaced longitudinal channels filled with the electrode structure. This consists of concentric rods and tubes parallel to the beam axis and is integrated into the endcap cryostats. The resolution in

the barrel and endcap is $\sigma_E/E = 50\%\sqrt{E} \oplus 3\%$ while in the forward region it is $\sigma_E/E = 100\%\sqrt{E} \oplus 10\%$.

2.2.3 Muon Spectrometer

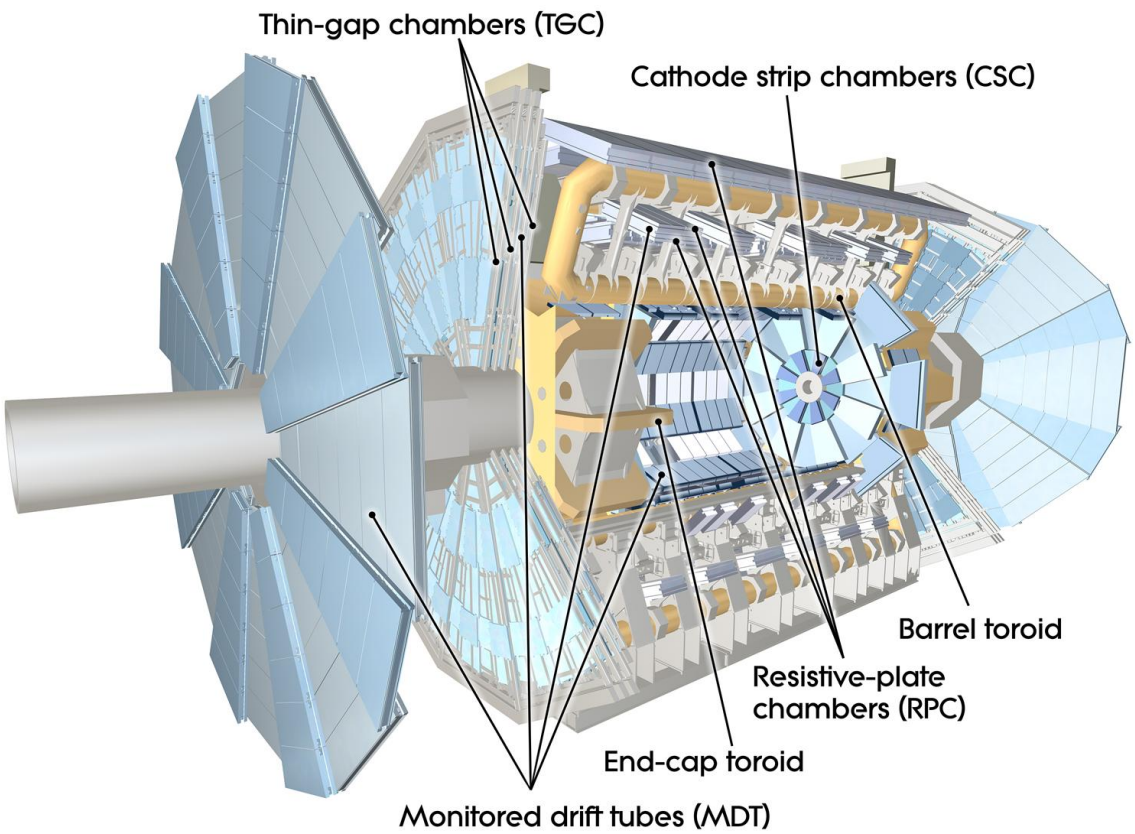

Figure 2.6: The Muon Spectrometer in ATLAS. [67]

The Muon Spectrometer provides detection of muon tracks in the large superconducting air-core toroid magnets. It is instrumented with trigger chambers and high-precision tracking chambers which cover the whole outer range of the ATLAS detector for $|\eta| < 2.7$ (Figure 2.6). The muon tracks are bent by the barrel toroid magnetic field of 1.5 to 5.5 Tm for $|\eta| < 1.4$, or by two small endcap magnets inserted

into the barrel toroid. Those have approximately 1 to 7.5 Tm for $1.6 < \eta < 2.7$. The combination of them is used for $1.4 < \eta < 1.6$ (a transition region with low efficiency). In the barrel region, muons are measured in three layers of chambers around the beam axis while for large pseudorapidities, three layers of chambers are installed perpendicular to the beam.

For most of the η range, the muon tracks are measured in the principal bending direction of the magnetic field by isolated Monitored Drift Tubes (MDTs). At large pseudorapidities, Cathode Strip Chambers (CSC) are used to deal with the high particle fluxes at the innermost plane over $2.0 < \eta < 2.7$. The trigger system uses Resistive Plate Chambers (RPCs) in the barrel and Thin Gap Chambers (TGCs) in the endcap region to provide bunch crossing identication, well defined p_{T} thresholds, and measurement of the muon coordinates. Muons in the p_{T} range 3 GeV to 1 TeV are measured with the best efficiency and resolution. In the case of low p_{T} muons, the resolution deteriorates due to multiple scattering and fluctuation of the energy loss in the calorimeters. The muon resolution is $\sigma_{p_{\mathrm{T}}}/p_{\mathrm{T}} = 10\%$ at $p_{\mathrm{T}} = 1$ TeV.

2.2.4 Trigger and data acquisition

ATLAS uses a three level trigger system, Level-1 (LVL1), Level-2 (LVL2), and event filter (EF) (Figure 2.7). The LVL2 and EF together are called the High-Level Trigger (HLT). The LVL1 trigger searches for signatures of each particular type of object directly from the front-end electronics. The maximum accept rate of LVL1 is 75 kHz. The HLT is computer based. The LVL2 trigger is seeded by Regions-of-Interest (RoIs) identified by the LVL1 trigger and reduces the event rate to below 3.5 kHz. The EF uses offline analysis procedures on fully built events to reduce the event rate to approximately 200 Hz to be recorded for subsequent offline analysis.

The data acquisition system (DAQ) receives and buffers the event data from

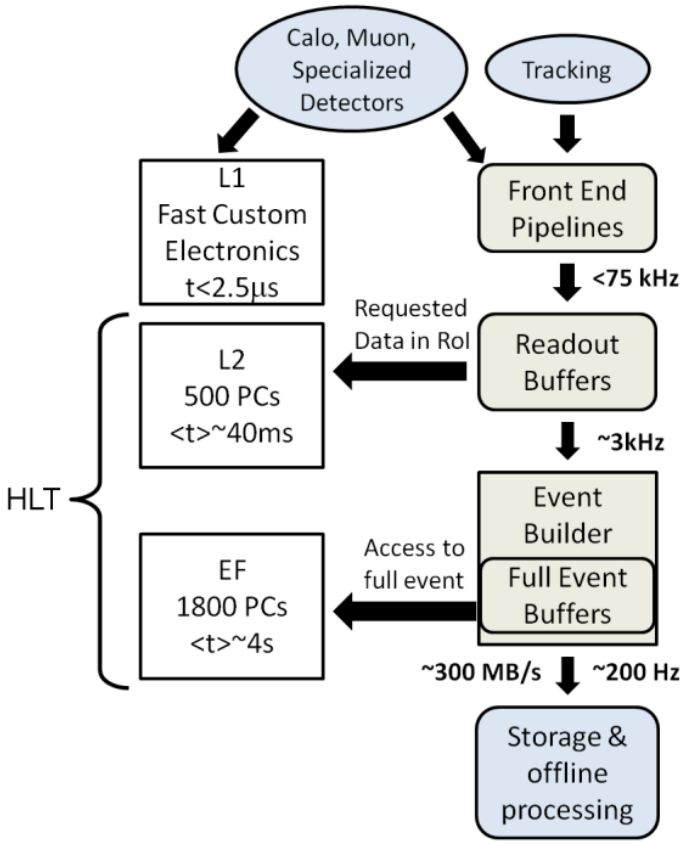

Figure 2.7: The ATLAS three-level trigger system. [71]

specific readout electronics and feeds back to the LVL2 trigger though point-to-point Readout Links (ROLs) if requested. The event-building is performed and moved by the DAQ to the EF, and the events selected by the EF are moved to permanent event storage by the DAQ again. The DAQ provides for the configuration, control, and monitoring of the ATLAS detector during data-taking as well.

2.2.5 Forward detectors and luminosity

The LUCID (Luminosity measurement using Cerenkov Integrating Detector) lies at ± 17 m from the interaction point and detects inelastic pp scattering in the ATLAS

forward direction for the online relative-luminosity monitor.

Using observed interactions per crossing, μ_{vis}, the luminosity is given by

$$\mathscr{L} = \frac{\mu_{vis} n_b f_r}{\sigma_{vis}} \tag{2.1}$$

where $\sigma_{vis} = \varepsilon \sigma_{inel}$ is the total inelastic cross-section multiplied by the efficiency ε

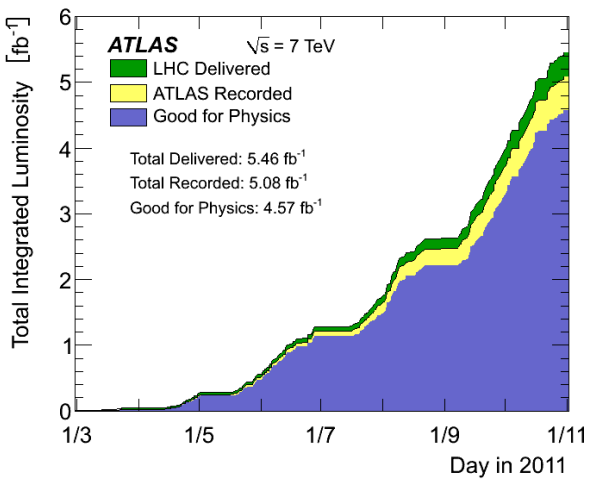

(a)

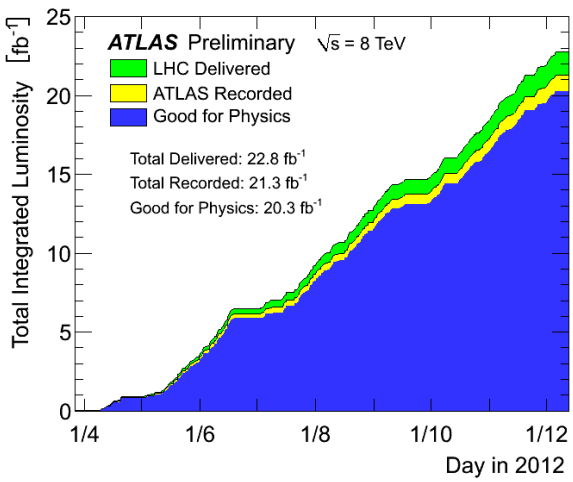

(b)

Figure 2.8: The integrated delivered, recorded, and good for physics luminosities at ATLAS in 2011 (a) and 2012 (b). [66]

of a particular detector with an algorithm obtained from calibration.

The recorded luminosity that was good for physics analysis in 2011 is 4.57 fb^{-1} (Figure 2.8 (a)) with uncertainty of 1.8% while that in 2012 is 20.3 fb^{-1} (Figure 2.8 (b)) with uncertainty of 2.8%. [59]

2.2.6 Particle identification

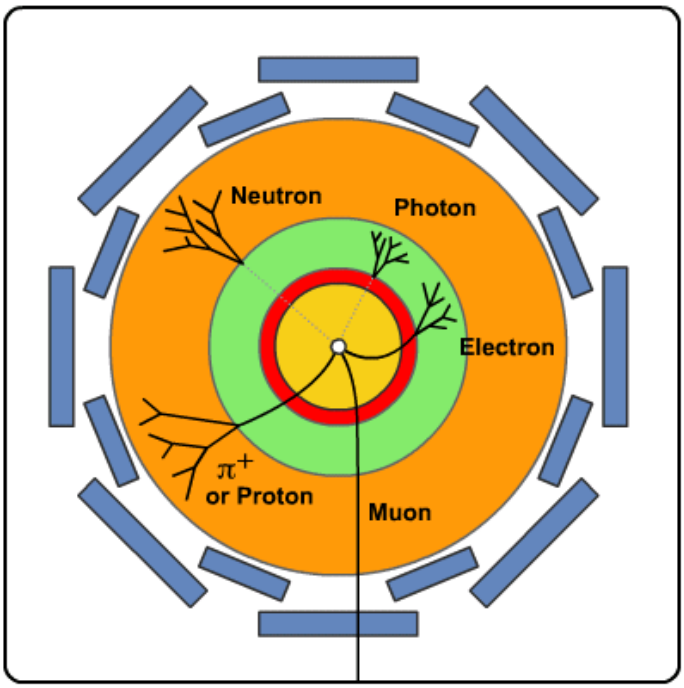

Figure 2.9: Illustration of the responses of the ATLAS subsystems to various particle types. [67]

ATLAS does not have particle identification that can distinguish, for example, between a pion and a kaon. The particles produced from the *pp* collision are identified only by their interactions in subdetectors (Figure 2.9).

The Inner Detector records the charge and momentum of the charged particles in the magnetic field. The Electromagnetic Calorimeter identifies the electrons,

positrons, and photons and measures their energy deposits. The Hadronic Calorimeter measures the energy deposits of the hadrons (protons, neutrons, pions, etc). The Muon Detector measures the charge and momentum of the muons. Neutrinos are only detectable indirectly via missing energy which is not recorded in the calorimeters. The charged tracks registered in the calorimeter and in the muon detector are tagged and matched with the tracks in the Inner Detector.

Chapter 3

The B_C meson and excited B states

This chapter describes the search for the B_c meson and excited B states. The ground state is reconstructed through the hadronic decay mode of $B_c \rightarrow J/\psi\pi$, $J/\psi \rightarrow \mu^+\mu^-$. As a cross check, the $B^+ \rightarrow J/\psi K^+$ which has the same topology has also been studied. The relevant excited B_c states are scanned in the mass difference distribution, which is defined as the mass of the combination of the ground state plus the mass of the two hadronic tracks minus the mass of the ground state and two pions. The excited B_s states are also reconstructed by adding one hadronic track to the B^+ candidate. They are fitted using the same procedure as for the excited B_c states to verify the analysis strategy.

3.1 Data sample

The analysis uses only the data taken when both the ATLAS Inner Detector and Muon Spectrometer subsystems were fully operational, and when LHC beams were stable. Samples in the year 2011 with $\sqrt{s} = 7$ TeV corresponding to integrated luminosity of 4.9 fb^{-1}, and in the year 2012 with $\sqrt{s} = 8$ TeV corresponding to

integrated luminosity of 19.2 fb^{-1}, have been selected for this analysis.

3.2 Triggers used in the analysis for the various data-taking periods

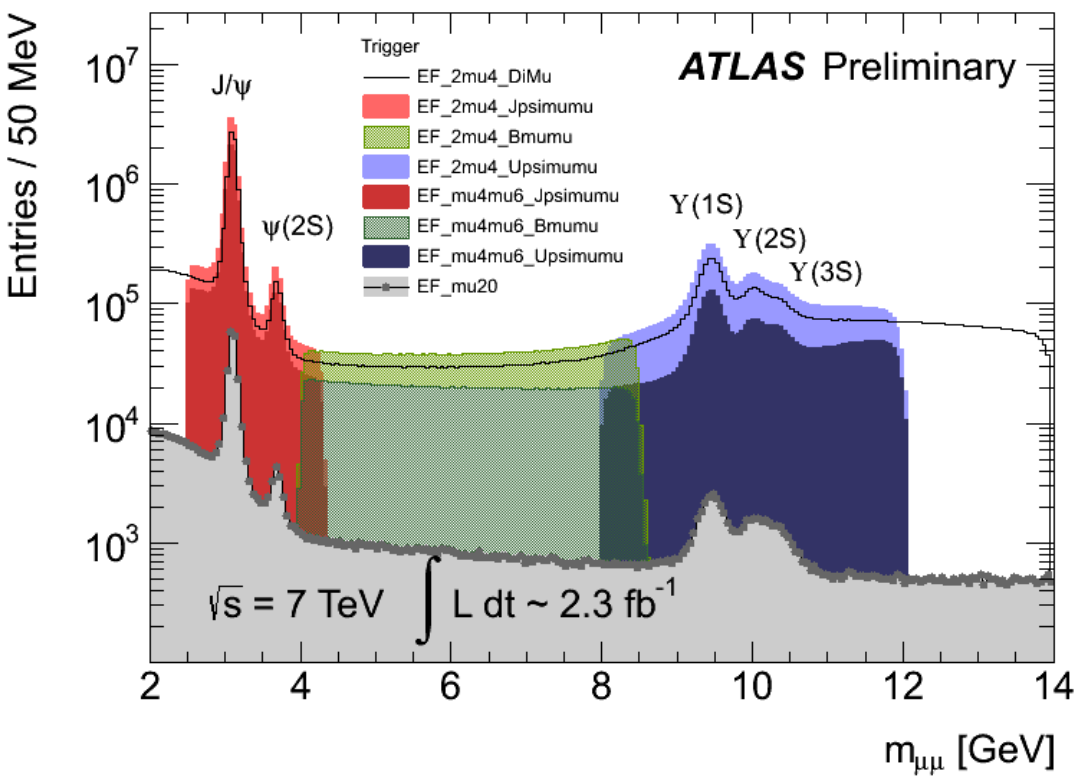

Figure 3.1: The B physics triggers. [66]

The B-triggers in ATLAS include both single muon and di-muon triggers:

- The Single Muon Trigger selects a LVL1 muon confirmed in the Inner Detector and precision muon chambers with kinematic cuts and a channel specified mass

cut. The p_{T} threshold starts from $p_{\mathrm{T}} > 4$ GeV and moves to $p_{\mathrm{T}} > 6$ GeV for high luminosity.

- The Di-Muon Trigger includes different combinations: (1) two LVL1 muons confirmed in the HLT with a good vertex fit and mass cut (this is called the topology di-muon trigger); (2) a LVL1 muon followed by a second muon found at LVL2 inside an RoI about the LVL1 trigger muon; (3) a LVL1 muon followed by a track reconstructed in the ID from a jet in the ROI in LVL1 or a track reconstructed in the TRT from an EM deposit in the ROI in LVL1.

The topology di-muon triggers have specified mass cuts that depend on the decay channels. For $J/\psi \to \mu^+\mu^-$ the mass cut is [2.5, 4.3] GeV, for $B \to \mu^+\mu^-$ the mass cut is [4, 8.3] GeV, and for $\Upsilon \to \mu^+\mu^-$ the mass cut is [8, 12] GeV (Figure 3.1).

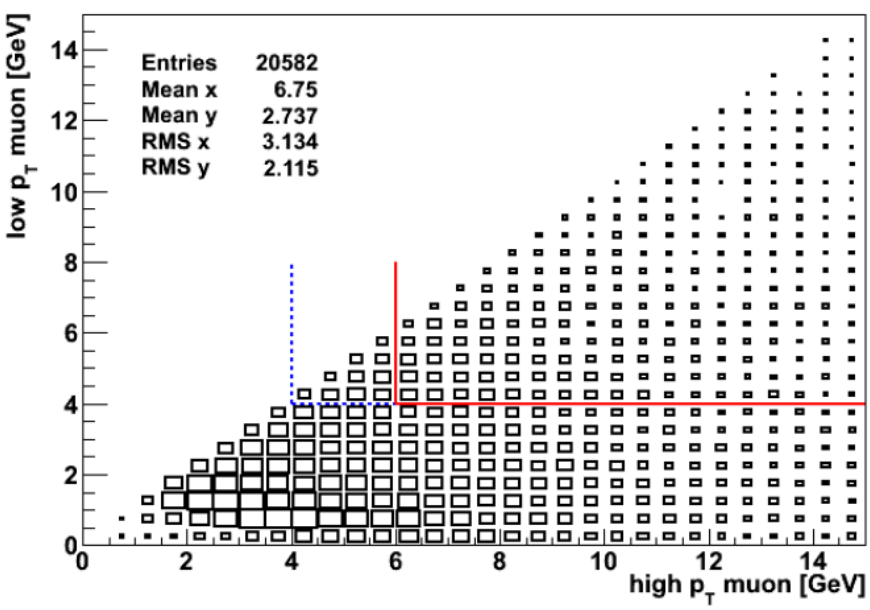

Figure 3.2: The predicted B_c production rate as a function of the transverse momentum of the triggered muons at generator level. [72]

This analysis relies on the topology di-muon triggers. The B_c production density

is shown in Figure 3.2 [72]. The baseline B physics trigger used is the EF_2mu4_Jpsimumu trigger for early 2011 data (periods B–I) and the EF_mu4(T)mu6_Jpsimumu trigger for late 2011 data (periods J–M) and all the 2012 data (Table 3.2). Both the EF_2mu4_Jpsimumu and EF_mu4Tmu6_Jpsimumu triggers are fully unprescaled in 2011. The EF_mu4Tmu6_Jpsimumu trigger is almost unprescaled (with the prescale factor never exceeding 5%) in 2012 data. Selection of the higher thresholds for the late 2011 data allows a cross-check of the consistency of the signal yields in the 2011 and 2012 runs. The lower thresholds in the early 2011 data are used because no higher threshold trigger existed. For 2012 runs, the B-physics stream (where the set of triggers is specified for B physics analysis) data are analyzed. Because this stream became active from period B in 2012, the 0.7 fb^{-1} collected in period A are not included in the analysis.

Periods	Event Filter signatures used
2011 B–F	`EF_mu6_Jpsimumu, EF_2mu4_Jpsimumu, EF_mu6_Jpsimumu_tight, EF_mu10_Jpsimumu`
2011 G–H	`EF_mu4mu6_Jpsimumu, EF_mu6_Jpsimumu EF_2mu4_Jpsimumu, EF_mu6_Jpsimumu_tight EF_mu10_Jpsimumu`
2011 I	`EF_mu4mu6_Jpsimumu, EF_2mu4_Jpsimumu`
2011 J–K	`EF_mu4mu6_Jpsimumu`
2011 L–M	`EF_mu4Tmu6_Jpsimumu, EF_mu6_Jpsimumu`
2012 B–C5	`EF_mu4mu6_Jpsimumu_L2StarA`
2012 C6–L	`EF_mu4mu6_Jpsimumu_L2StarA, EF_mu4mu6_Jpsimumu_L2StarB`

In early 2012 (periods B−C5), a known problem existed with the L2 trigger setting. The L2 trigger tracking algorithm L2StarA resulted in suppression of the events with large muon-track impact parameters. During data-taking that bug was fixed in two ways: starting from the 2012 period C6, a different tracking algorithm called L2StarB became active, and starting from the 2012 period D, a fix was introduced into the L2StarA-based trigger chain itself. The trigger menu thus contained (since period C6) two variants of the J/ψ trigger: EF_mu4Tmu6_Jpsimumu (L2StarA-based

L2 tracking) and EF_mu4Tmu6_Jpsimumu_L2StarB (L2StarB-based L2 tracking). The 2012 analysis uses events triggered by either of these two triggers. The impact of the bias caused by the L2StarA algorithm (affecting only the 2012 periods B-C5) is studied in Section 3.8.

3.3 Monte Carlo generator and samples

3.3.1 PYTHIA_BC generator

All the B_c channels used are generated using the PYTHIA_BC MC generator [75]. Within standard PYTHIA, the fragmentation mechanism for B_c production is implemented only for $p_{\mathrm{T}} > 40$ GeV. For smaller transverse momenta, the dominant mechanism of B_c production is the (unimplemented) recombination mechanism. PYTHIA_BC implements both of these mechanisms. The B_c mesons produced by PYTHIA_BC were marked as stable and then decayed within the EvtGen package [76] with specified decay matrix elements set as a default.

3.3.2 PYTHIA_B generator

All the $b\bar{b}$ and B hadron MC samples except the B_c channels are generated using the PYTHIA_B MC generator. PYTHIA_B is an extension of the PYTHIA_I interface with some extra features used by the B physics group mainly to filter b events. It was written in Fortran for PYTHIA6 initially and fully rewritten in C++ for PYTHIA8 [78]. Three mechanisms to produce the b quark are provided: flavor creation ($gg \to b\bar{b}$, $qq \to b\bar{b}$), flavor excitation ($gb \to gb$), and gluon splitting ($g \to b\bar{b}$). All the beauty production parameters are provided as a default. PYTHIA_B provides choices for user specified decay channels and limits on the p_{T} and η of the $b\bar{b}$ quarks to speed up the

simulation. [79]

3.3.3 Monte Carlo data sample

The MC samples used in this analysis are:

- Signal:
  - $B_c^+ \to J/\psi\pi^+$
- Exclusive background:
  - $B_c^+ \to J/\psi K^+$, where the K^+ is misidentified as a π^+.
  - $B_c^+ \to J/\psi\rho^+$, $\rho \to \pi^0\pi^+$, where the neutral pion goes undetected.
  - $B_c^+ \to J/\psi\mu^+\nu$, where the μ^+ is misidentified as a π^+.
  - $B_c^+ \to J/\psi\pi^0\pi^+$, where the neutral pion goes undetected.
  - $B_c^+ \to J/\psi\pi^+\pi^-\pi^+$, where only one π^+ is observed.
- Combinatorial background:
  - $b\bar{b} \to J/\psi X$
  - $pp \to J/\psi X$
- The cross check channel:
  - $B^+ \to J/\psi K^+$

The B_c signal and exclusive background channel samples are generated using the *Pythia_Bc* MC generator. The $b\bar{b}$ and B^+ samples are generated using the *Pythia_B* MC generator. The pp samples are generated with the *Pythia*8 MC generator. They have been tuned to the data. The ATLAS detector is simulated with the Geant4

package [80]. Those events are fully reconstructed with the same software that is used to process the data from the detector.

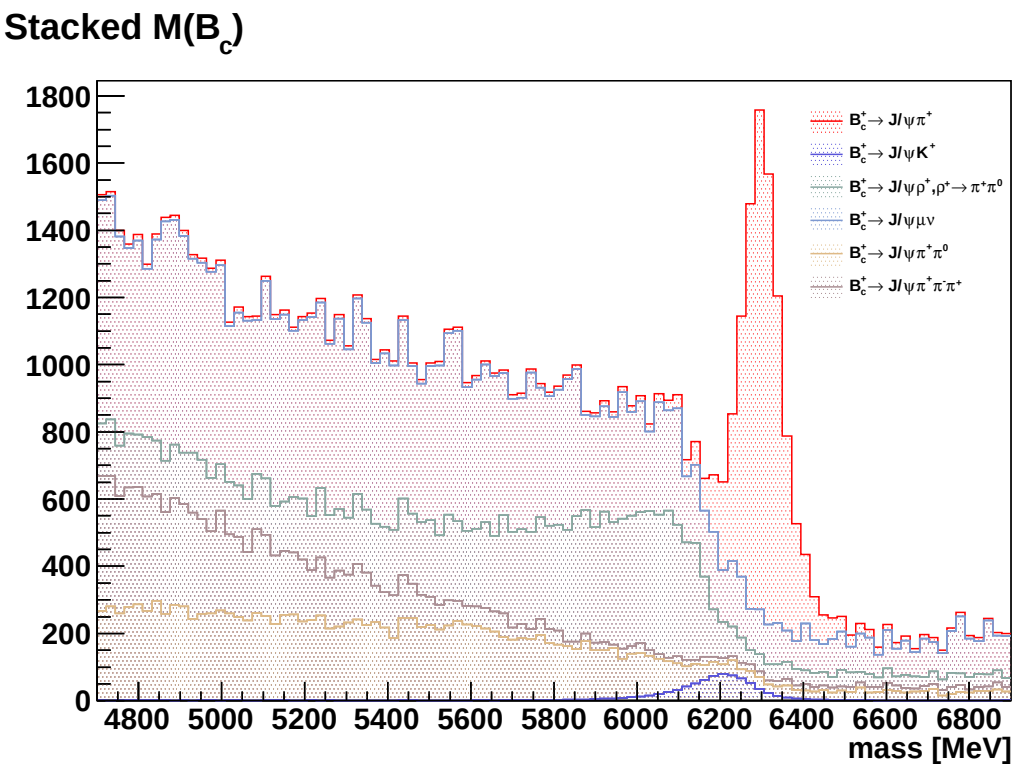

Figure 3.3: The stacked mass distribution of the B_c signal channel plus 5 exclusive decay channels. Each entry has been scaled to its predicted production cross section.

The two muons are generated to have $p_{\mathrm{T}} > (6, 4)$ GeV in 2011 or $p_{\mathrm{T}} > 2.5$ GeV in 2012. Hadronic tracks are generated to have $p_{\mathrm{T}} > 500$ MeV. Final state particles are required to have $|\eta| < 2.5$. For the signal sample and for the exclusive backgrounds, $p_{\mathrm{T}}(B_c) > 10$ GeV at the generator level is required.

There are two kinds of combinatorial backgrounds: (1) the combination of produced J/ψ directly at the collision point with a hadronic track, and (2) the combination of a J/ψ daughter of a b quark decay with a hadronic track. These are the main sources of background under the B_c peak. The exclusive backgrounds raise the

left sideband of the B_c peak (Figure 3.3).

The cross check decay $B^{\pm} \to J/\psi K^{\pm}$ has a very similar topology to the decay $B_c^{\pm} \to J/\psi \pi^{\pm}$, and due to its 10^3 times higher rate of production, may result in a background contribution to the B_c signal region. A study of a 10M event MC12 sample of $B^{\pm} \to J/\psi K^{\pm}$ decay (muon threshold (2.5, 2.5) MeV) shows that only 4 of 10M events survive the B_c offline cuts. Due to the smallness of this number of events, it is not possible to extrapolate the shape of the background, and the contribution of this exclusive background to the B_c region [5630, 6820] MeV is estimated to be of the level of 5-10%.

3.4 Track reconstruction

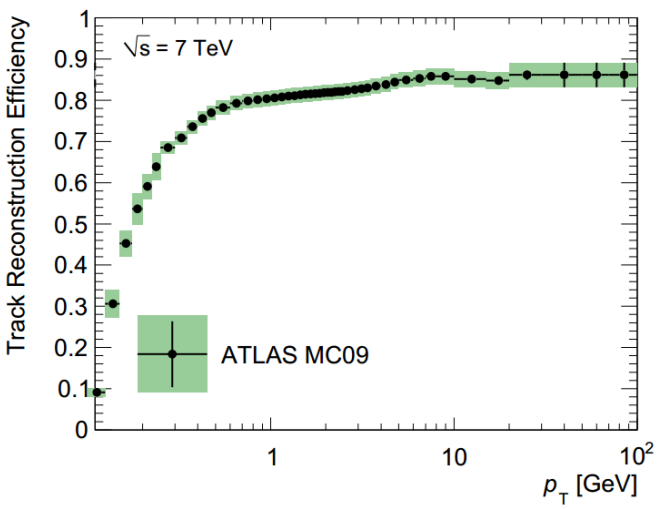

Figure 3.4: MC efficiency for reconstructing and selecting primary charged particles as a function of generated track p_{T}. Uncertainties due to limited MC statistics are shown as vertical error bars, while the combined systematic uncertainty is indicated by the green band (averaged over η). [73]

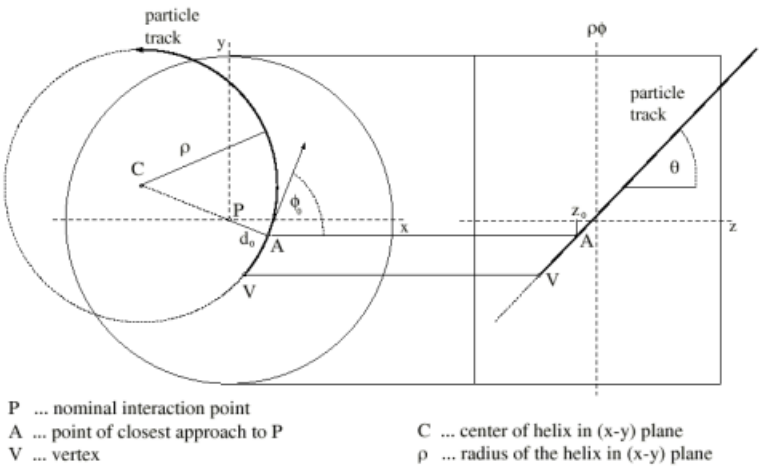

Figure 3.5: The definition of ATLAS perigee parameters [74].

The ID tracks used in this analysis are reconstructed with a tracking algorithm that starts from 3-point seeds in the silicon detectors. These tracks are extended into the TRT by adding hits from tracks moving away from the interaction point. ID tracks with transverse momentum greater than 400 MeV (the study [73] of the track reconstruction efficiency is in Figure 3.4) and magnitude of pseudorapidity less than 2.5 are reconstructed. The ID track is required to have at least three hits in the silicon detectors of the inner tracker ($\geqslant 1$ hit in the Pixel Detector and $\geqslant 2$ hits in the SCT). The perigee parameters ($d_0,\ z_0,\ \phi_0,\ \theta,\ q/p$), as defined in Figure 3.5, are calculated by the tracking algorithm for each reconstructed track.

3.5 Muon reconstruction

Muon reconstruction in ATLAS makes use of the Inner Detector and the Muon Spectrometer. Muons pass through the calorimeters and reach the MS if their momentum is above about 3 GeV. Two categories of reconstructed muons are used at ATLAS:

- Combined muons; the candidate is formed from a stand-alone MS track which is matched with an ID track. The pseudorapidity coverage is $|\eta| < 2.5$.

- Tagged muons; these consist of ID tracks extrapolated to the Muon Spectrometer and matched to patterns of MS hits. This reconstruction is particularly important for low-p_{T} (< 6 GeV) muons, which do not have a stand-alone MS track because their p_{T} is not large enough to reach more than one Muon Spectrometer super-layer. The pseudorapidity coverage of tagged muons is $|\eta| < 2.5$.

For both combined and tagged muons, the ID track is required to have at least three hits in the silicon detectors of the inner tracker ($\geqslant 1$ hit in the Pixel Detector and $\geqslant 2$ hits in the SCT). Although both the ID and the MS provide momentum measurements, in the p_{T} range relevant to this analysis, the MS momentum resolution is worse than that of the ID due to energy loss in the calorimeters. Therefore the MS is used only to identify muons, and the p_{T} measurement is taken from the ID. In this analysis only combined muons have been used.

3.6 Reconstruction of the B ground state and excited state candidates

3.6.1 Reconstruction of the B ground state candidates

The B_c meson is reconstructed through its decay channel $B_c \to J/\psi\pi$. The $B^+ \to J/\psi K$ decay channel, with the same topology, is used for a cross check.

The J/ψ candidates are reconstructed from pairs of triggered oppositely charged muons fitted to a common vertex. The invariant mass $m(\mu^+\mu^-)$ calculated from

the refitted track parameters is required to lie in the mass window $\pm 3\sigma$ around the PDG mass $m_{J/\psi}$, 3096.916 MeV [23], where the J/ψ width σ varies depending on the detector resolution (three times higher in endcaps than in barrel) in the three different regions of pseudorapidity. (Those are: (1) both muons have $|\eta| < 1.05$, (2) one has $|\eta| < 1.05$ while one has $1.05 < |\eta| < 2.5$, and (3) both muons have $1.05 < |\eta| < 2.5$ [60].) The width also depends on the period of data-taking due to the different trigger settings (Table 3.2).

The B_c meson and B^+ meson are reconstructed by combining a hadronic track with the reconstructed J/ψ candidate by performing a vertex fit on all three tracks with the VKalVrt fitter [61] with the J/ψ mass constrained to the PDG mass. No pointing constraint is required for the ground state vertex fit. The primary vertex (PV) is refitted with those tracks removed. All the parameters related to the PV are recalculated according to the refitted one. In each event, only the reconstructed B candidate with the best $\chi^2/N.d.o.f$ is chosen.

3.6.2 Reconstruction of the B excited state candidates

In this analysis, only the hadronic $B_c(2S)$ decays to the B_c ground state are reconstructed. The state is predicted to have a mass in the range 6856–6917 MeV[27]. The next S-wave state, $B_c(3S)$ [25], is predicted to have a mass above the threshold for decay into a BD meson pair, hence it does not contribute to the ground state topology. Transitions between the spin states occur through soft photon radiation which escapes identification. They can not be separated by this analysis.

B candidates are required to be within a mass window of 3σ ($\sigma = 40$ MeV) around the B PDG mass. The two daughter pions from the $B_c(2S)$ decay are predicted to be very soft, therefore all reconstructed Inner Detector hadronic tracks (with $p_{\mathrm{T}} > 400$ MeV) are considered. Hadronic tracks from the same reconstructed primary vertex

to which the B_c (B^+) ground state total momentum is pointing are used. Two (one) are/is combined with the reconstructed ground state candidate. A simultaneous cascade fit is applied to all those 5(4) tracks with a J/ψ mass constraint, no pointing constraint to the primary vertex is required. Those fitted vertices with larger $N.d.o.f$ are rejected to avoid cases in which the fitted vertex is located in front of the primary vertex. The wrong charge combinations are collected for the background comparison. No additional cuts or constraints are applied for the excited state reconstruction in order to avoid selection bias, except the $\Delta z0$ (the difference between the $z0$ of the hadron track and the $z0$ of the leading muon) cut to reduce the effect of pile-up in the 2012 data. In each event, only the reconstructed excited candidate with the best $\chi^2/N.d.o.f$ is chosen.

Wrong charge combinations ($B_c^{\pm}\pi^+\pi^+$ and $B_c^{\pm}\pi^-\pi^-$, or $B^{\pm}\pi^{\pm}$) are kept separately for the combinatorial background shape determination.

3.7 Selection of 2011 data

Channel	Events	Generator-level cuts on J/ψ muons	Cross section σ
$B_c^+ \to J/\psi(\mu^+\mu^-)\pi^+$, signal	65K	$p_{\mathrm{T}} > (6, 4)$ GeV	17.63 pb
$B_c^+ \to J/\psi(\mu^+\mu^-)K^+$	50K	$p_{\mathrm{T}} > (6, 4)$ GeV	1.49 pb
$B_c^+ \to J/\psi(\mu^+\mu^-)\rho(\pi^+\pi^-)$	50K	$p_{\mathrm{T}} > (6, 4)$ GeV	54.25 pb
$B_c^+ \to J/\psi(\mu^+\mu^-)\mu\nu$	50K	$p_{\mathrm{T}} > (6, 4)$ GeV	258 pb
$B_c^+ \to J/\psi(\mu^+\mu^-)\pi^+\pi^0$	50K	$p_{\mathrm{T}} > (6, 4)$ GeV	47.5 pb
$B_c^+ \to J/\psi(\mu^+\mu^-)\pi^+\pi^-\pi^+$	33K	$p_{\mathrm{T}} > (6, 4)$ GeV	51.5 pb
$pp \to J/\psi(\mu^+\mu^-)X$	1M	$p_{\mathrm{T}} > (2.5, 2.5)$ GeV	425 nb
$b\bar{b} \to J/\psi(\mu^+\mu^-)X$	2M	$p_{\mathrm{T}} > (2.5, 2.5)$ GeV	55.68 nb

Table 3.1: Details of Monte Carlo samples for the signal and various backgrounds, for the 2011 conditions.

Selection requirements to extract the B_c ground state signal from the background

are chosen by comparing parameter distributions versus cut values for the B_c signal channel and the backgrounds. The background MC samples were checked for inclusion of signal events to avoid double counting. Individual MC samples are weighted by the corresponding cross sections. The number of events in those MC background samples, the generator-level cuts on them, and the corresponding cross sections in 2011 are listed in Table 3.1.

3.7.1 Event selection

Every selected event is required to be associated with a primary vertex reconstructed from at least 3 tracks. Different kinds of reconstructed primary vertices are recorded by ATLAS:

- The Type 1 vertex is the one whose constituent tracks (the tracks used to build it) have the greatest summed p_{T}.
- The Type 3 vertices are the ones attributed to the pile-up.
- Tracks which are not used to build any primary vertices are associated with a dummy primary vertex which has the code 0. It is usually a copy of the type 1 vertex, unless this does not exist, in which case it is a copy of the beam spot.

In 2011, only Type 1 vertices are used as the true vertex from which the B meson decays.

3.7.2 J/ψ selection

The triggered di-muon pairs are selected with transverse momentum thresholds of (6,4) GeV (Figure 3.6(a), (b)). The muon tracks are required to pass the 2011

ID hits requirements [69], with offline cuts on number of pixel hits larger than 1, number of SCT hits larger than 6, and a loose vertex cut of $\chi^2/N.d.o.f.(J/\psi) < 15$ (Figure 3.6(c)).

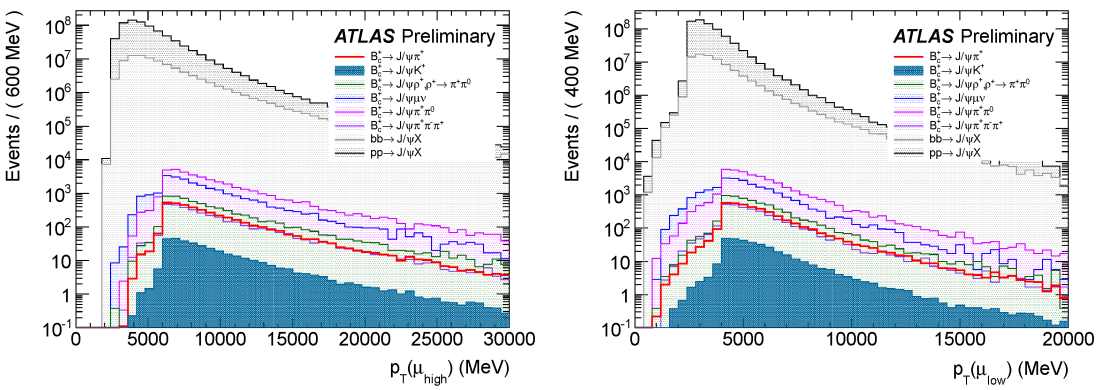

Figure 3.6: (a) The p_{T} distribution of the higher p_{T} muon, (b) the p_{T} distribution of the lower p_{T} muon, (c) the $\chi^2/N.d.o.f$ of the reconstructed J/ψ vertex.

The non-zero width of the J/ψ peak is attributed to detector resolution. The difference in the muon reconstruction efficiency in the ATLAS barrel and endcap regions manifests itself in the different widths of the J/ψ candidates' invariant mass distributions. A sum of Gaussian and Crystal Ball functions with common mean m_0 and width s is used to fit the peak in order to account for the radiative effects. A

linear function is used to describe the background. The Crystal Ball function $f_{CB}(m)$ combines a Gaussian core and a power-law tail with an exponent n to account for energy loss due to final-state photon radiation,

$$f_{CB}(m) = \begin{cases} \frac{N}{\sqrt{2\pi}\sigma} \exp(-\frac{(m-m_0)^2}{2\sigma^0}), & \frac{m-m_0}{\sigma} > -\alpha; \\ \frac{N}{\sqrt{2\pi}\sigma}(\frac{n}{|\alpha|})^n \exp(-\frac{(|\alpha|)^2}{2})(\frac{n}{|\alpha|} - |\alpha| - \frac{m-m_0}{\sigma})^{-n}, & \frac{m-m_0}{\sigma} \leq -\alpha. \end{cases} \tag{3.1}$$

The parameter α defines the transition between the Gaussian and the power-law functions. For each period using different trigger settings (Table 3.2), the J/ψ mass distribution has been fitted for four cases with both muons: (1) in the barrel region, (2) one in the barrel and one in the endcap, (3) both in the endcaps, and (4) all candidates (Figures 3.7–3.26). The di-muon mass is required to be within 3σ of the J/ψ PDG mass in those three η ranges (Table 3.2).

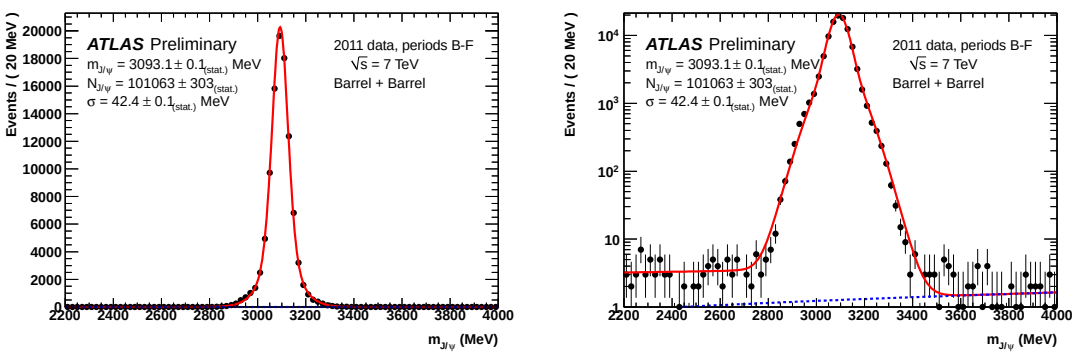

(a) (b)

Figure 3.7: The J/ψ candidate invariant mass distribution, for events in which both muons are in the barrel region, with linear scale (a) and with log scale (b), for the periods B–F. The distributions are fitted with an unbinned maximum likelihood fit (solid line) with a sum of Gaussian and Crystal Ball functions for the signal plus a linear function for the background (dotted line).

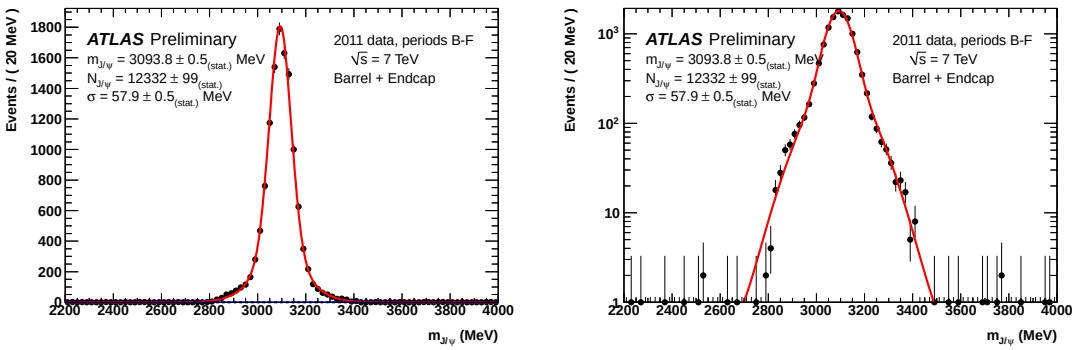

(a) (b)

Figure 3.8: The J/ψ candidate invariant mass distribution, for events in which one muon in barrel and one muon in endcap, with linear scale (a) and with log scale (b), for the periods B–F. The distributions are fitted with an unbinned maximum likelihood fit (solid line) with a sum of Gaussian and Crystal Ball functions for the signal plus a linear function for the background (dotted line).

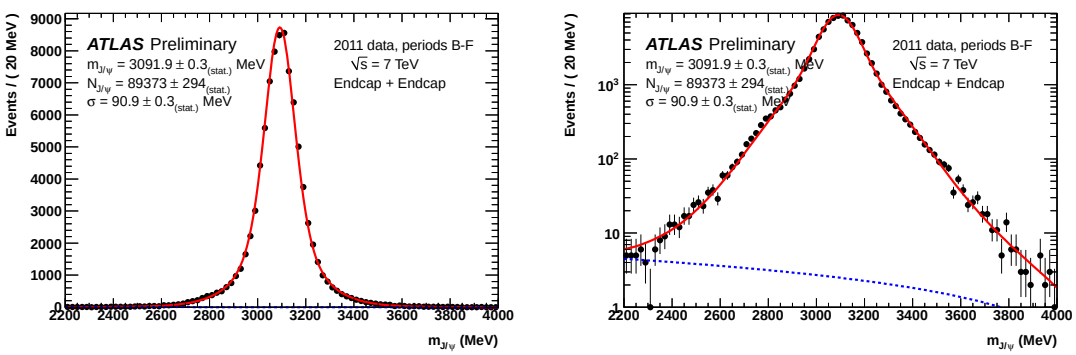

(a) (b)

Figure 3.9: The J/ψ candidate invariant mass distribution, for events in which both muons are both in endcap region, with linear scale (a) and with log scale (b), for the periods B–F. The distributions are fitted with an unbinned maximum likelihood fit (solid line) with a sum of Gaussian and Crystal Ball functions for the signal plus a linear function for the background (dotted line).

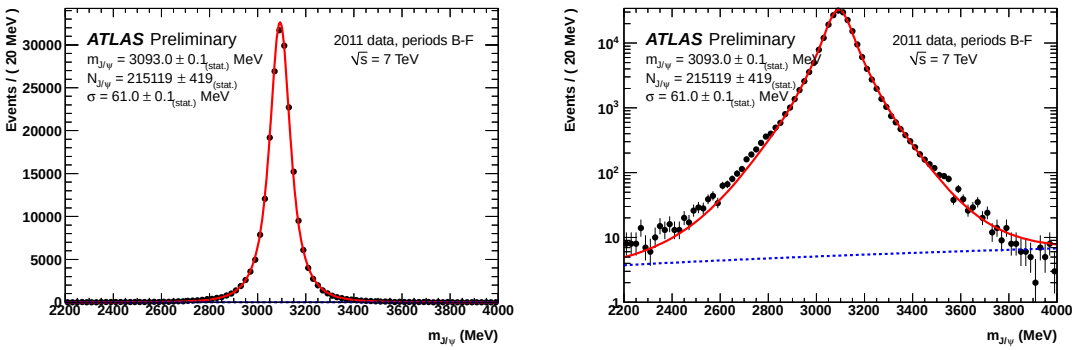

(a) (b)

Figure 3.10: The J/ψ candidate invariant mass distribution, for all candidates, with linear scale (a) and with log scale (b), for the periods B–F. The distributions are fitted with an unbinned maximum likelihood fit (solid line) with a sum of Gaussian and Crystal Ball functions for the signal plus a linear function for the background (dotted line).

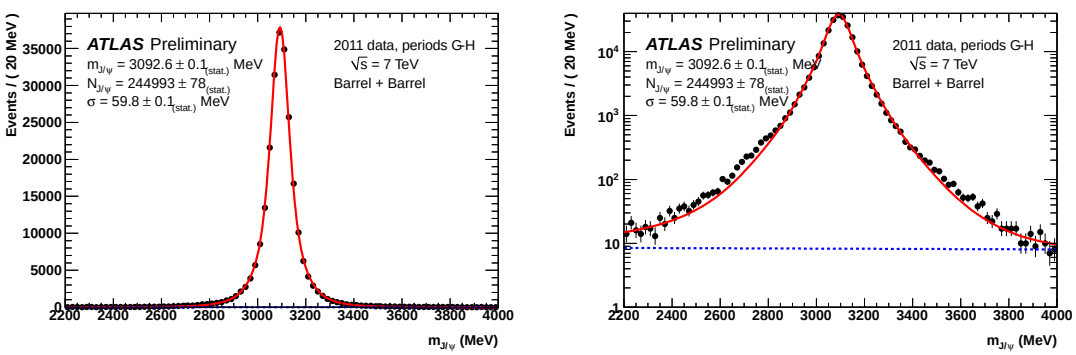

(a) (b)

Figure 3.11: The J/ψ candidate invariant mass distribution, for events in which both muons are in the barrel region, with linear scale (a) and with log scale (b), for the periods G–H. The distributions are fitted with an unbinned maximum likelihood fit (solid line) with a sum of Gaussian and Crystal Ball functions for the signal plus a linear function for the background (dotted line).

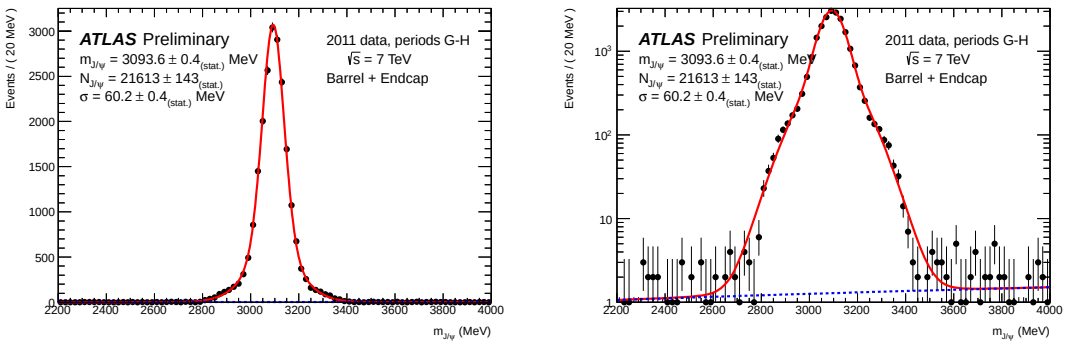

(a) (b)

Figure 3.12: The J/ψ candidate invariant mass distribution, for events in which one muon in barrel and one muon in endcap, with linear scale (a) and with log scale (b), for the periods G–H. The distributions are fitted with an unbinned maximum likelihood fit (solid line) with a sum of Gaussian and Crystal Ball functions for the signal plus a linear function for the background (dotted line).

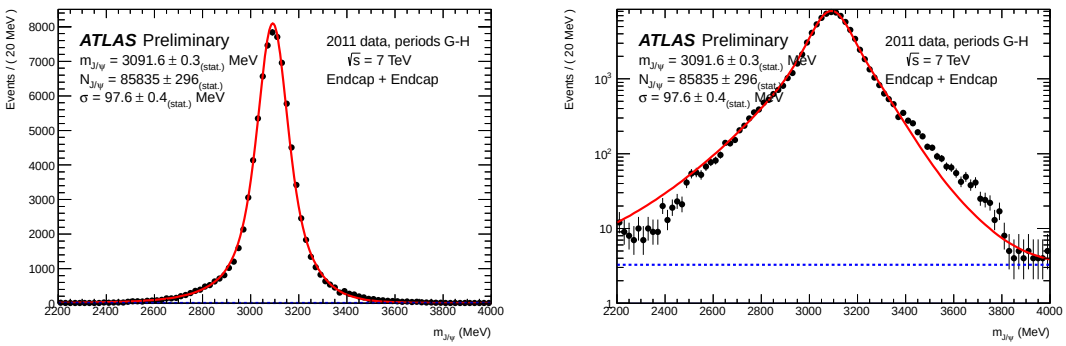

(a) (b)

Figure 3.13: The J/ψ candidate invariant mass distribution, for events in which both muons are both in endcap region, with linear scale (a) and with log scale (b), for the periods G–H. The distributions are fitted with an unbinned maximum likelihood fit (solid line) with a sum of Gaussian and Crystal Ball functions for the signal plus a linear function for the background (dotted line).

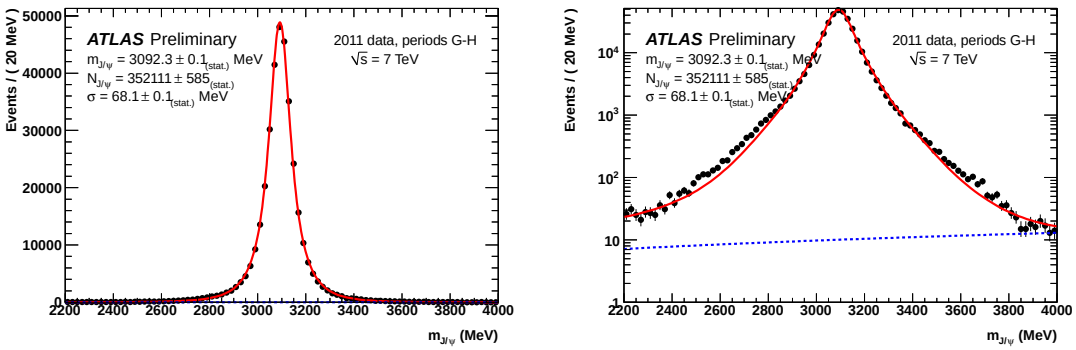

(a) (b)

Figure 3.14: The J/ψ candidate invariant mass distribution, for all candidates, with linear scale (a) and with log scale (b), for the periods G–H. The distributions are fitted with an unbinned maximum likelihood fit (solid line) with a sum of Gaussian and Crystal Ball functions for the signal plus a linear function for the background (dotted line).

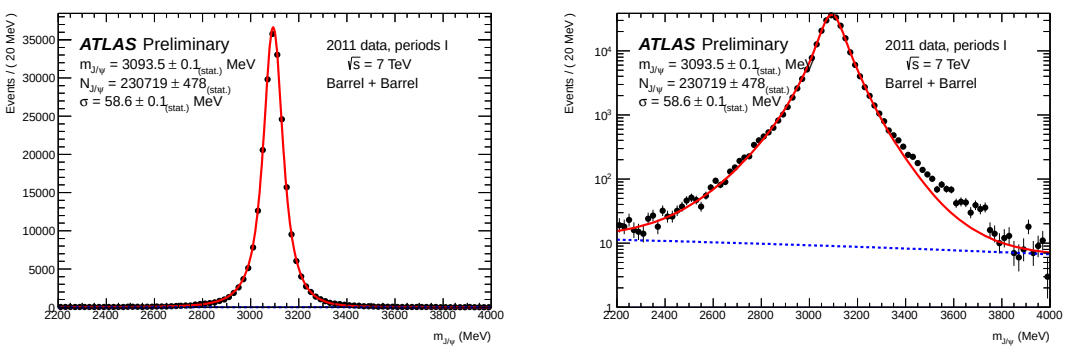

(a) (b)

Figure 3.15: The J/ψ candidate invariant mass distribution, for events in which both muons are in the barrel region, with linear scale (a) and with log scale (b), for the periods I. The distributions are fitted with an unbinned maximum likelihood fit (solid line) with a sum of Gaussian and Crystal Ball functions for the signal plus a linear function for the background (dotted line).

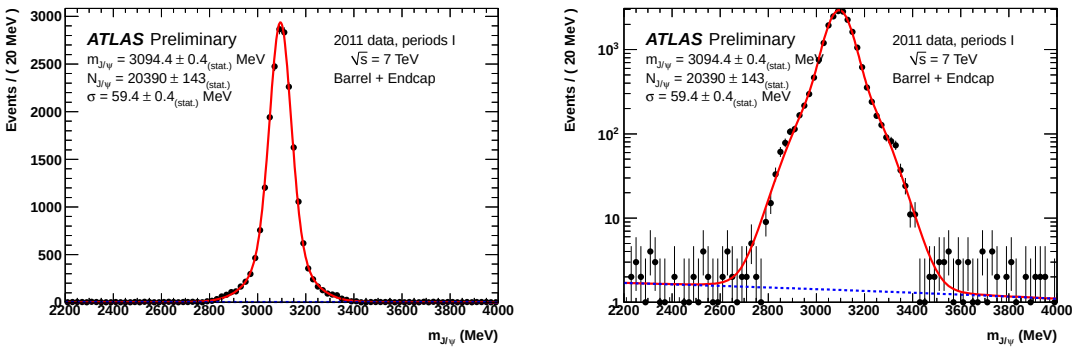

(a) (b)

Figure 3.16: The J/ψ candidate invariant mass distribution, for events in which one muon in barrel and one muon in endcap, with linear scale (a) and with log scale (b), for the periods I. The distributions are fitted with an unbinned maximum likelihood fit (solid line) with a sum of Gaussian and Crystal Ball functions for the signal plus a linear function for the background (dotted line).

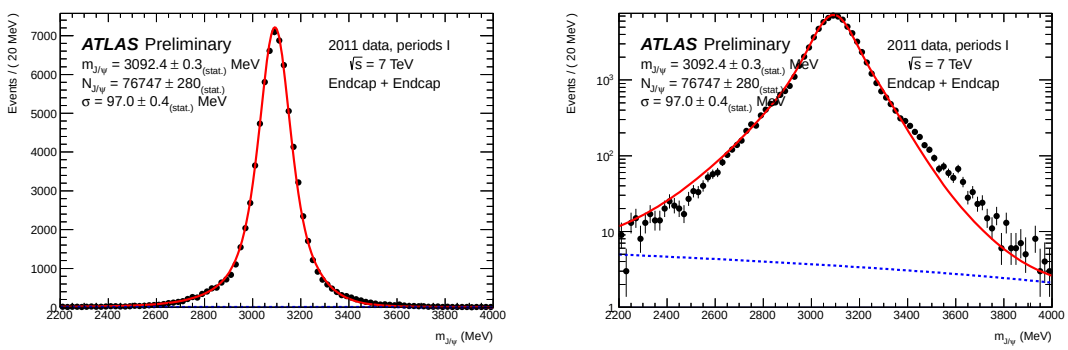

(a) (b)

Figure 3.17: The J/ψ candidate invariant mass distribution, for events in which both muons are both in endcap region, with linear scale (a) and with log scale (b), for the periods I. The distributions are fitted with an unbinned maximum likelihood fit (solid line) with a sum of Gaussian and Crystal Ball functions for the signal plus a linear function for the background (dotted line).

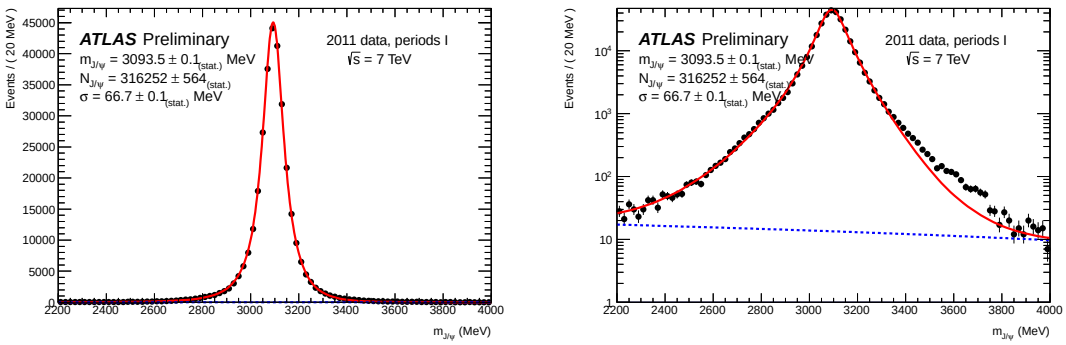

(a) (b)

Figure 3.18: The J/ψ candidate invariant mass distribution, for all candidates, with linear scale (a) and with log scale (b), for the periods I. The distributions are fitted with an unbinned maximum likelihood fit (solid line) with a sum of Gaussian and Crystal Ball functions for the signal plus a linear function for the background (dotted line).

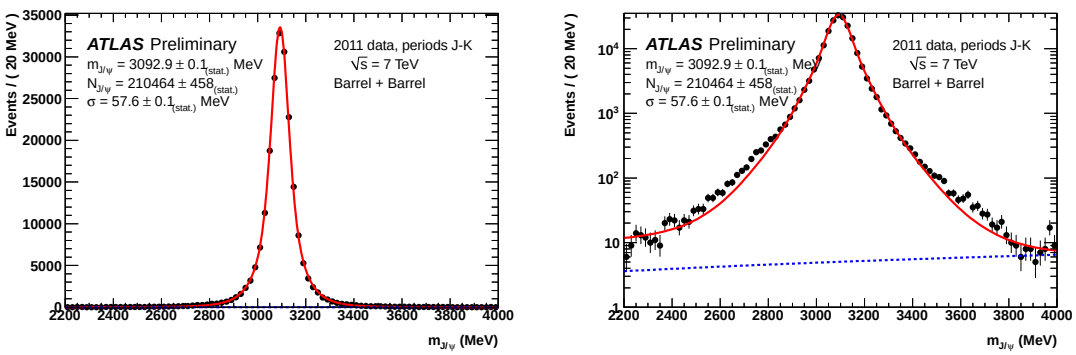

(a) (b)

Figure 3.19: The J/ψ candidate invariant mass distribution, for events in which both muons are in the barrel region, with linear scale (a) and with log scale (b), for the periods J–K. The distributions are fitted with an unbinned maximum likelihood fit (solid line) with a sum of Gaussian and Crystal Ball functions for the signal plus a linear function for the background (dotted line).

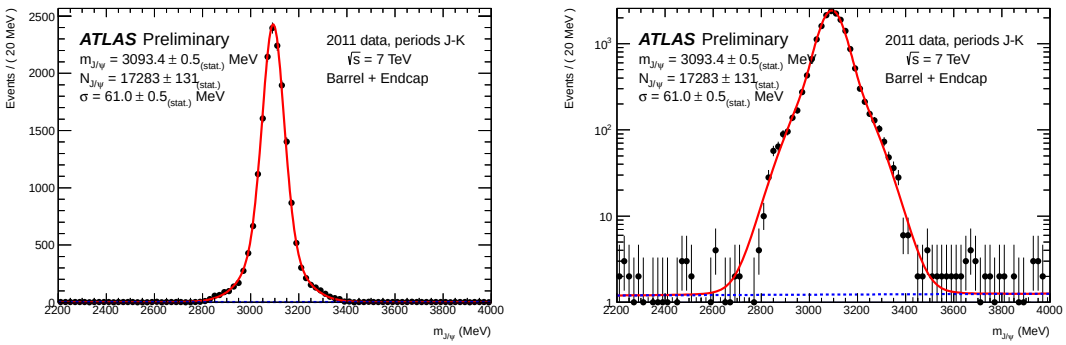

(a) (b)

Figure 3.20: The J/ψ candidate invariant mass distribution, for events in which one muon in barrel and one muon in endcap, with linear scale (a) and with log scale (b), for the periods J–K. The distributions are fitted with an unbinned maximum likelihood fit (solid line) with a sum of Gaussian and Crystal Ball functions for the signal plus a linear function for the background (dotted line).

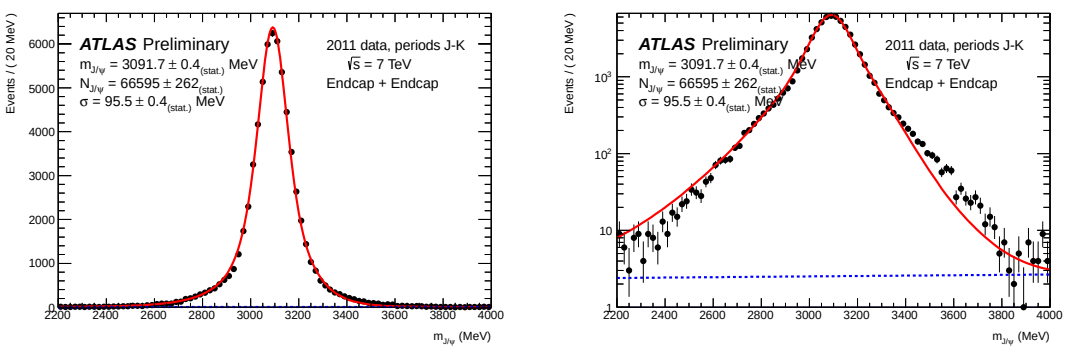

(a) (b)

Figure 3.21: The J/ψ candidate invariant mass distribution, for events in which both muons are both in endcap region, with linear scale (a) and with log scale (b), for the periods J–K. The distributions are fitted with an unbinned maximum likelihood fit (solid line) with a sum of Gaussian and Crystal Ball functions for the signal plus a linear function for the background (dotted line).

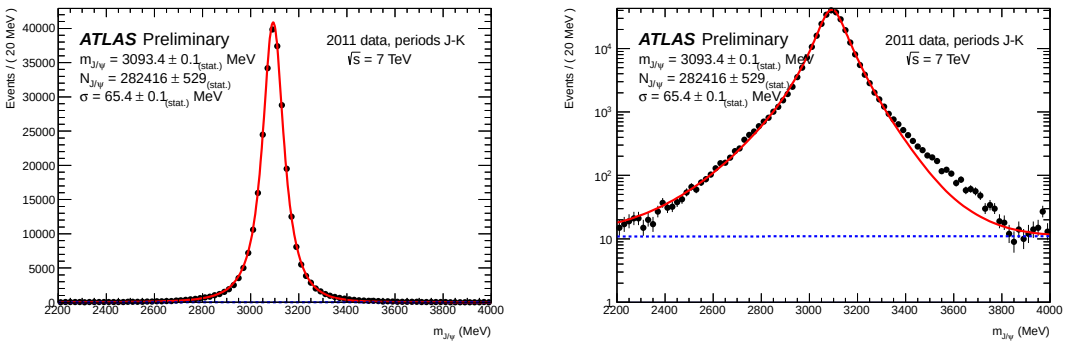

(a) (b)

Figure 3.22: The J/ψ candidate invariant mass distribution, for all candidates, with linear scale (a) and with log scale (b), for the periods J–K. The distributions are fitted with an unbinned maximum likelihood fit (solid line) with a sum of Gaussian and Crystal Ball functions for the signal plus a linear function for the background (dotted line).

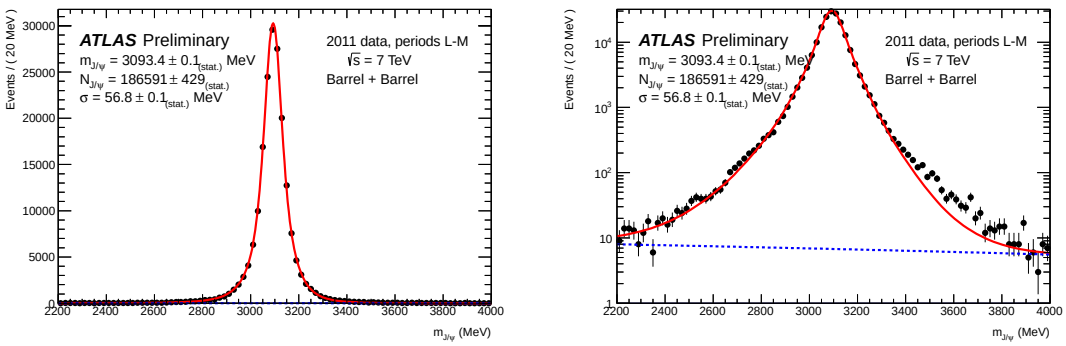

(a) (b)

Figure 3.23: The J/ψ candidate invariant mass distribution, for events in which both muons are in the barrel region, with linear scale (a) and with log scale (b), for the periods L–M. The distributions are fitted with an unbinned maximum likelihood fit (solid line) with a sum of Gaussian and Crystal Ball functions for the signal plus a linear function for the background (dotted line).

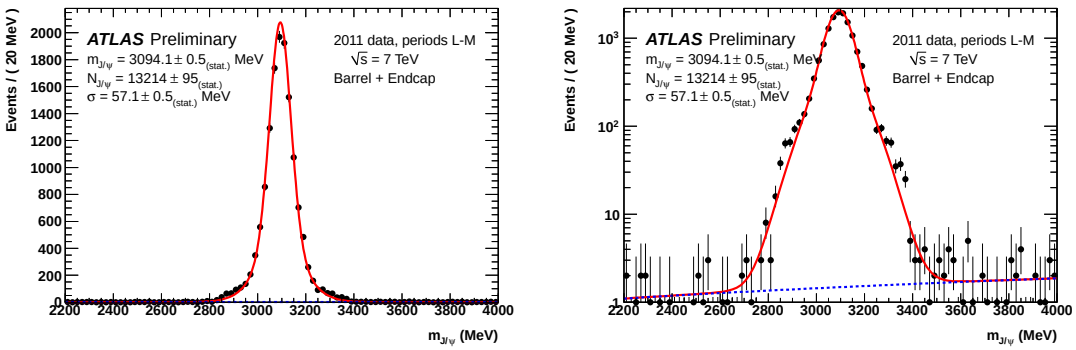

(a) (b)

Figure 3.24: The J/ψ candidate invariant mass distribution, for events in which one muon in barrel and one muon in endcap, with linear scale (a) and with log scale (b), for the periods L–M. The distributions are fitted with an unbinned maximum likelihood fit (solid line) with a sum of Gaussian and Crystal Ball functions for the signal plus a linear function for the background (dotted line).

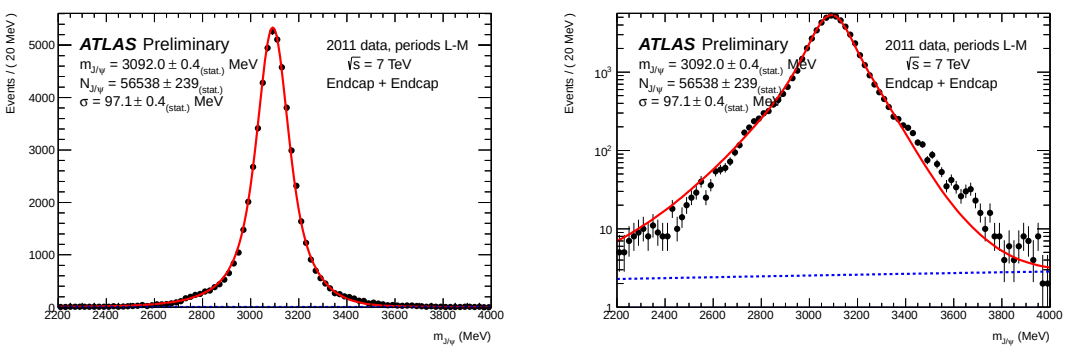

(a) (b)

Figure 3.25: The J/ψ candidate invariant mass distribution, for events in which both muons are both in endcap region, with linear scale (a) and with log scale (b), for the periods L–M. The distributions are fitted with an unbinned maximum likelihood fit (solid line) with a sum of Gaussian and Crystal Ball functions for the signal plus a linear function for the background (dotted line).

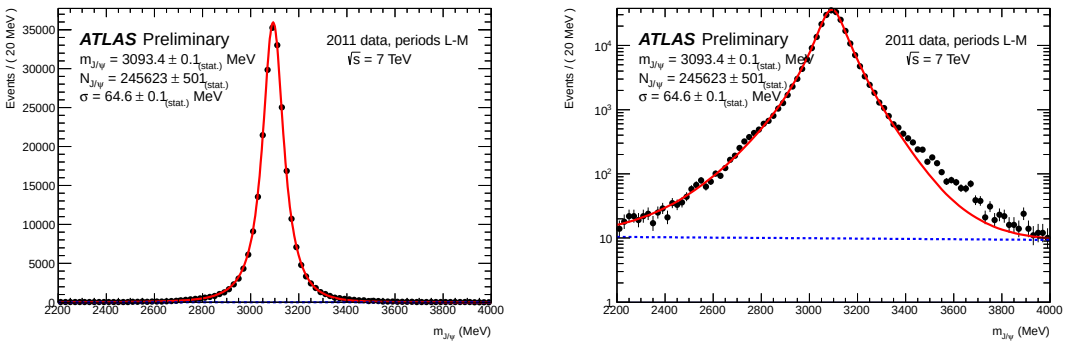

(a) (b)

Figure 3.26: The J/ψ candidate invariant mass distribution, for all candidates, with linear scale (a) and with log scale (b), for the periods L–M. The distributions are fitted with an unbinned maximum likelihood fit (solid line) with a sum of Gaussian and Crystal Ball functions for the signal plus a linear function for the background (dotted line).

Data-taking periods	J/ψ mean MeV	BB sigma, MeV	BE sigma MeV	EE sigma MeV	Yield
B–F	$3093.1\pm0.1_{stat}$	$42.4\pm0.1_{stat}$	$57.9\pm0.5_{stat}$	$90.9\pm0.3_{stat}$	561668
G–H	$3092.3\pm0.1_{stat}$	$59.8\pm0.1_{stat}$	$60.2\pm0.4_{stat}$	$97.6\ \pm0.4_{stat}$	433634
I	$3093.5\pm0.1_{stat}$	$58.6\pm0.1_{stat}$	$59.4\pm0.4_{stat}$	$97.0\pm0.4_{stat}$	817188
J–K	$3093.4\pm0.1_{stat}$	$57.6\pm0.1_{stat}$	$61.0\pm0.5_{stat}$	$95.5\pm0.4_{stat}$	326115
L–M	$3093.4\pm0.1_{stat}$	$56.8\pm0.1_{stat}$	$57.1\pm0.5_{stat}$	$97.1\pm0.4_{stat}$	296526

Table 3.2: The summary table of the mean of the J/ψ invariant masses and the Gaussian widths (BB: both muons in barrel; BE: one muon in barrel, one muon in endcap; EE: both muons in endcap) and yields for every data-taking period. The masses are consistent from period to period. The differences above the statistical error may give an impression of the order of the detector-related systematics.

3.7.3 Hadronic track selection

For 2011 data, the hadronic tracks with transverse momentum $p_{\mathrm{T}}(\pi) > 4$ GeV (Figure 3.27(a)), number of pixel hits larger than 1, and number of silicon hits larger

than 6 [68] are considered. Unlike the case of the B^+, the short B_c meson lifetime means that lifetime cuts are not efficient in separating the B_c signal from direct J/ψ combinations. The transverse impact parameter significance ($d^0_{xy}/\sigma(d^0_{xy})$) of the pion track related to the primary vertex is more efficient because of the pion's relatively low momentum compared to the B^+. As is shown in Figure 3.27(b), this is required to be larger than 5.

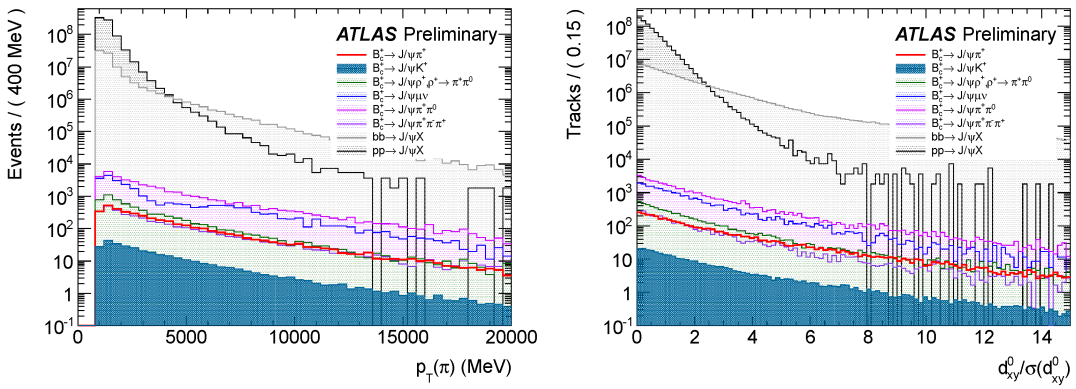

(a) (b)

Figure 3.27: (a) The track p_{T} and (b) d^0_{xy} significance distributions.

Two uncertainties contribute to the uncertainty of the hadronic track d^0_{xy}: the uncertainty on the hadronic track resolution and the uncertainty on the primary vertex resolution ($\sigma(PV)$). The distributions of track resolution uncertainty are shown in Figure 3.28(a) for the various periods of ATLAS data-taking. The mean uncertainty on the primary vertex position in the transverse plane is about two times smaller than the uncertainty on the track resolution. The distributions of this uncertainty are shown in Figure 3.28(b) for the various periods of ATLAS data-taking. The shape and the mean value of this uncertainty do not deviate much from period to period despite different pile-up conditions.

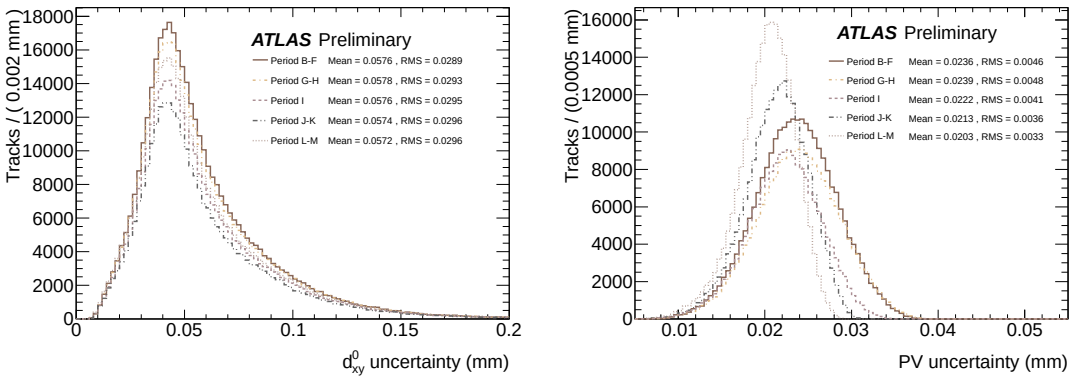

(a) (b)

Figure 3.28: (a) The $\sigma(d^0_{xy})$ of the hadronic tracks in periods with different trigger settings, and (b) The $\sigma(PV)$ of the primary vertex associated with the reconstructed B candidates in periods with different trigger settings.

3.7.4 B candidate selection

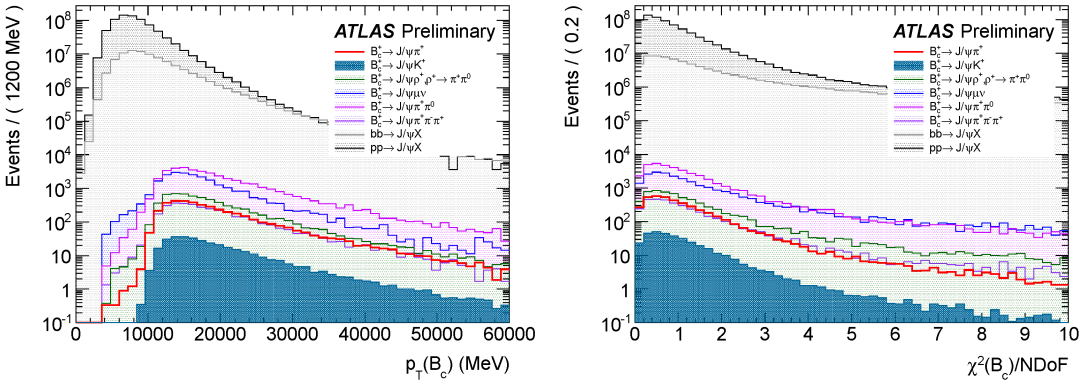

(a) (b)

Figure 3.29: (a) The p_{T} and (b) the $\chi^2/N.d.o.f.$ distributions of the reconstructed B vertex.

To reduce the combinatorial backgrounds, a p_{T} cut is applied on the reconstructed B candidates. They are required to have p_{T} larger than 15 GeV as shown in Figure 3.29(a). The B candidates with the best $\chi^2/N.d.o.f.$ have been selected for each

event, and that value is required to be less than 2 (Figure 3.29(b)). This reduces the number of fake B_c candidates and other badly reconstructed candidates contributing to the background. On average, about 0.1 additional ground state candidates per event have been removed.

3.7.5 B_c excited state selection

All reconstructed hadronic tracks ($p_{\mathrm{T}} > 400$ MeV) were considered. The excited state's decay vertex is very close to its production (primary) vertex. In this analysis the hadronic tracks associated with the excited state are required to originate in the same reconstructed primary vertex with which the B ground state is associated. Offline track quality cuts on the number of pixel hits (larger than 0) and silicon hits (larger than 6) are applied to reduce the fake rate [68].

3.8 Yields of the B^+ and B_c in 2011 and 2012 data

The stability of the yield ratio B_c/B^+ for the two years was checked. In the yield study, the cuts were frozen to their 2011 values, to confirm the existence of the $B_c(2S)$ signal. A single `EF_mu4Tmu6_Jpsimumu` trigger was used. As mentioned in Section 3.2, this trigger was unprescaled in 2011 and almost unprescaled in 2012. For comparison, the 2011 periods L and M were used since they have the same trigger setting as the 2012 data.

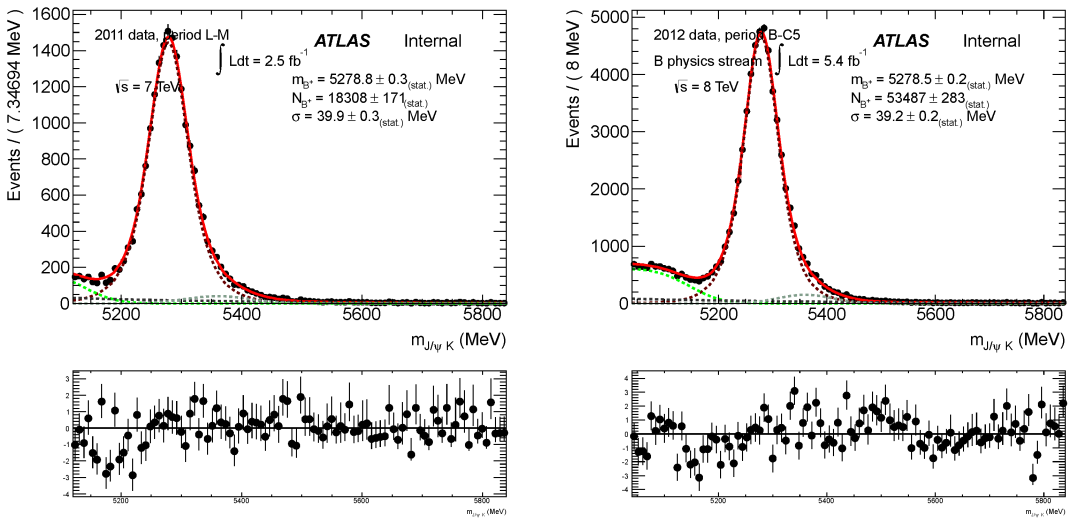

(a) 2011 period L-M

(b) 2012 period B-C5

(c) 2012 period C6-E

(d) 2012 period G-L

Figure 3.30: Fits of the B^+ candidates' invariant mass distribution for the various data-taking periods with the unbinned maximum likelihood fit. The signal is described with a Gaussian; the background is described using an exponential plus an error function for the partially reconstructed candidates; the $B^+ \to J/\psi K$ is fitted using a Gaussian with a fixed mean mass value from the PDG. Both 2011 and 2012 data are analyzed with the 2011 cuts and a muon p_{T} threshold of (6,4) GeV. The datasets have been separated according to the change in the trigger settings and the size of their integrated luminosity. (a) 2011 periods L-M, 2.48 fb^{-1} (b) 2012 periods B-C5, 5.42 fb^{-1} (c) 2012 periods C6-E, 6.79 fb^{-1} (d) 2012 periods G-L, 7.04 fb^{-1}.

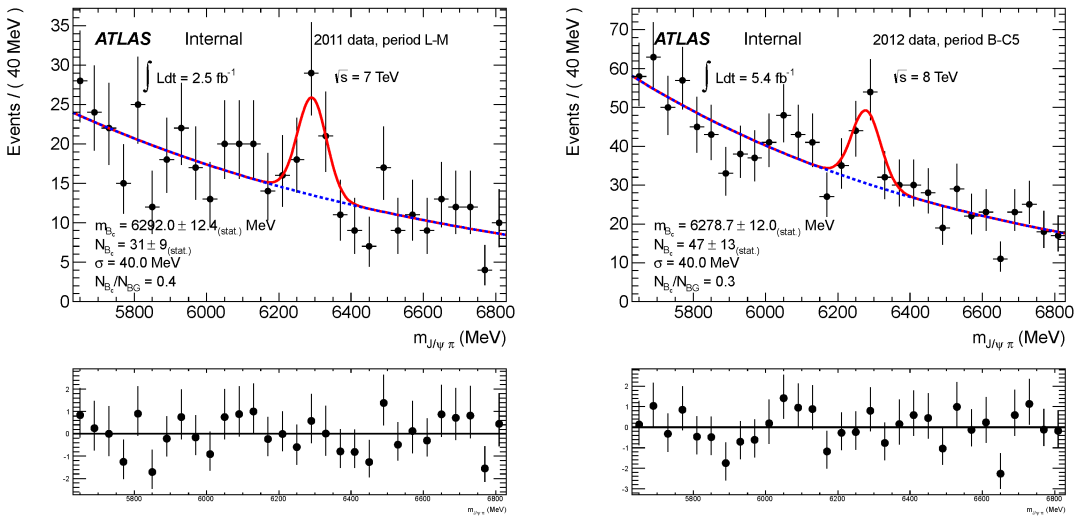

(a) 2011 period L-M

(b) 2012 period B-C5

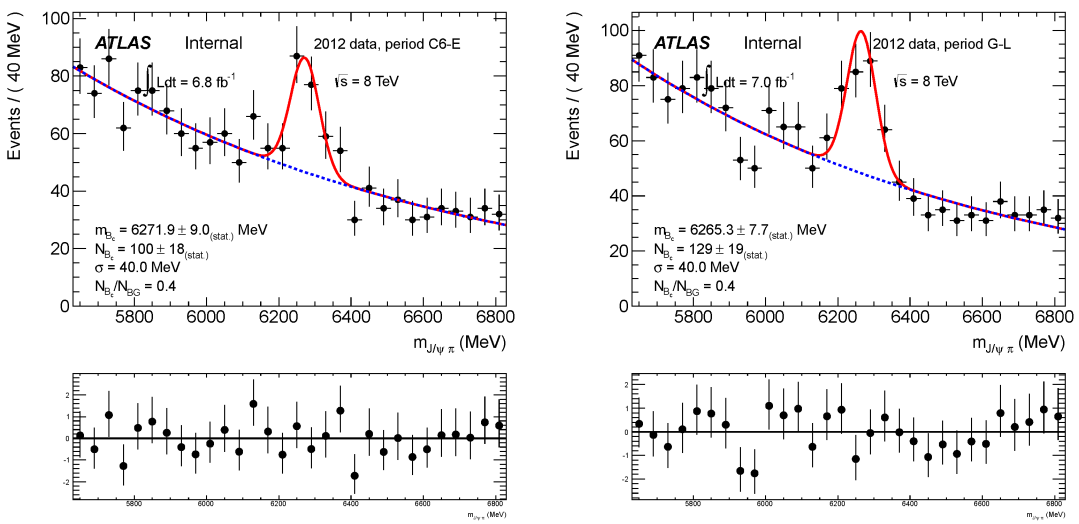

(c) 2012 period C6-E

(d) 2012 period G-L

Figure 3.31: Fits of the B_c candidates' invariant mass distribution for the various data-taking periods using the unbinned maximum likelihood function. The signal is fitted with a fixed width Gaussian, the width having been fixed to that of the B^+; the background is described using an exponential. The analysis of both 2011 and 2012 data use the 2011 cuts and muon p_{T} threshold of (6,4) GeV. (a) 2011 period L-M, 2.48fb^{-1} (b) 2012 period B-C5, 5.42 fb^{-1} (c) 2012 period C6-E, 6.79 fb^{-1} (d) 2012 period G-L, 7.04 fb^{-1}.

The number of B^+ events is extracted using an unbinned maximum likelihood fit with per event error (Figure 3.30). The number of B_c events is extracted using an unbinned maximum likelihood fit with a fixed width single Gaussian (Figure 3.31). The Gaussian width is fixed to the width of the B^+ peak (40 MeV). The observed increase in the number of background events is attributed to the higher pile-up in 2012. The relative increase in the B_c ground state production between the 7 and 8 TeV MC samples is found to be approximately 3%.

	2011 L-M	2012 B-C5	2012 C6-E	2012 G-L
L2	L2*A	broken L2*A	fixed L2*A and L2*B	fixed L2*A and L2*B
Event Filter	$\mu4\mu6$	$\mu4\mu6$	$\mu4\mu6$	$\mu4\mu6$
$\int \mathcal{L}dt$ (fb^{-1})	2.48	5.42	6.79	7.04
$N(B^+)$/fb^{-1}	7382 ± 69	9870 ± 52	11619 ± 53	11933 ± 41
$N(B_c)$/fb^{-1}	13 ± 4	9 ± 2	15 ± 3	18 ± 3
$N(B_c)/N(B^+)$(%)	16.9 ± 4.8	8.8 ± 2.4	12.7 ± 2.2	15.4 ± 2.2

Table 3.3: The yield of B^+ and B_c events per 1 fb^{-1} integrated luminosity and their relative yield in different periods. Events were selected using the EF_mu4Tmu6_-Jpsimumu trigger and 2011 cuts.

The 2011 MC samples are the B_c with di-muon p_{T} thresholds of (6, 4) GeV and the B^+ with di-muon p_{T} thresholds of (4, 4) GeV. The 2012 MC samples are the B_c with di-muon p_{T} thresholds of (2.5, 2.5) GeV and B^+ with di-muon p_{T} thresholds of (0, 0) GeV. To study the cut efficiency, both the number of generated true B^+ or B_c and the number of reconstructed true B^+ or B_c after the 2011 cuts had been applied were needed (Table 3.4). Since those samples are produced with different muon and B transverse momentum cuts, a set of preselection cuts were applied before counting the generated events. The muons are required to have transverse momentum larger than (6, 4) GeV and pseudorapidity less than 2.5. The hadronic tracks are required to have pseudorapidity magnitude less than 2.5. The B mesons are required to have transverse momentum larger than 15 GeV.

	B^+ generated	B^+ after cuts	B_c generated	B_c after cuts
MC11	354176	4430	56859	1483
MC12 L2StarA	8831	134	9644	158
MC12 L2StarB	8831	154	9644	168

Table 3.4: The number of B^+ and B_c events generated with preselection cuts on $p_{\mathrm{T}}(B) > 15$ GeV, $|\eta(\mu)| < 2.5$, $|\eta(\pi)| < 2.5$, and $p_{\mathrm{T}}(\mu_1, \mu_2) > (6, 4)$ GeV, the number of reconstructed B^+ and B_c events with 2011 cuts applied, and the EF_mu4Tmu6_Jpsimumu L2StarA or L2StarB trigger applied.

The ratio of the cut efficiencies between the 2011 and 2012 L2StarA and the ratio between the 2012 L2StarA and 2012 L2StarB triggers has been calculated for both B^+ and B_c to minimize the uncertainty from the production cross-section prediction. The relative efficiencies for ratios for B_c over B^+ were calculated as well. This largely cancels the uncertainties from the reconstruction efficiency.

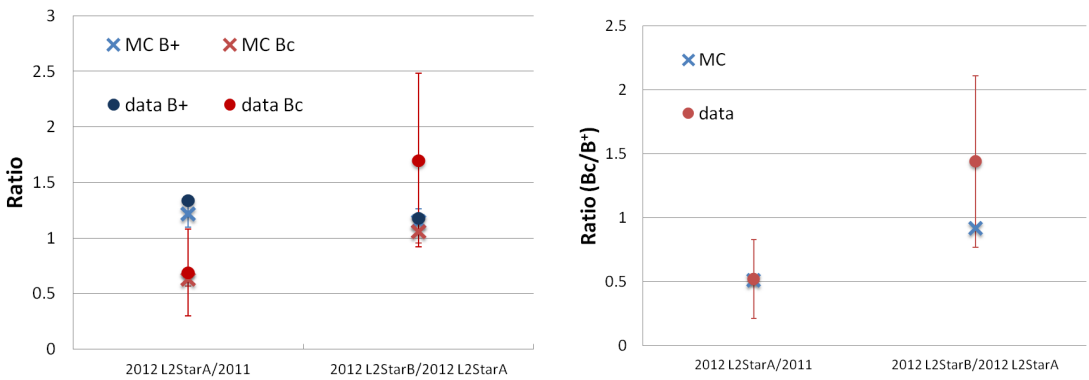

(a) (b)

Figure 3.32: (a) The ratio of the B^+ to B_c cut efficiencies for the 2011 and 2012 L2StarA trigger and the ratio between the L2StarA and L2StarB triggers in both data and MC. (b) The relative cut efficiency ratio of B_c over B^+ between the 2011 and 2012 L2StarA trigger and the one between the L2StarA and L2StarB triggers in both data and MC.

In Figure 3.32(a), one can see that these two ratios are in good agreement for data and MC for the B^+ and consistent within the uncertainties for the B_c. In

Figure 3.32(b), one can see that the relative ratios between the data and the MC are in good agreement within the uncertainties as well. We conclude from this that the change in B^+ and B_c yields from 2011 to 2012 is mainly caused by the change of the cut efficiency for these two years.

3.9 Selection of 2012 data

Channel	Events	Generator-level cuts on J/ψ muons	cross section σ
$B_c^+ \to J/\psi(\mu^+\mu^-)\pi^+$, signal	65K	$p_{\mathrm{T}} > (2.5, 2.5)$ GeV	17.63 pb
$B_c^+ \to J/\psi(\mu^+\mu^-)K^+$	50K	$p_{\mathrm{T}} > (2.5, 2.5)$ GeV	1.49pb
$B_c^+ \to J/\psi(\mu^+\mu^-)\rho(\pi^+\pi^-)$	50K	$p_{\mathrm{T}} > (2.5, 2.5)$ GeV	54.25 pb
$B_c^+ \to J/\psi(\mu^+\mu^-)\mu\nu$	50K	$p_{\mathrm{T}} > (2.5, 2.5)$ GeV	258 pb
$B_c^+ \to J/\psi(\mu^+\mu^-)\pi^+\pi^0$	50K	$p_{\mathrm{T}} > (2.5, 2.5)$ GeV	47.5 pb
$B_c^+ \to J/\psi(\mu^+\mu^-)\pi^+\pi^-\pi^+$	33K	$p_{\mathrm{T}} > (2.5, 2.5)$ GeV	51.5 pb
$pp \to J/\psi(\mu^+\mu^-)X$	1M	$p_{\mathrm{T}} > (2.5, 2.5)$ GeV	75.2 nb
$b\bar{b} \to J/\psi(\mu^+\mu^-)X$	2M	$p_{\mathrm{T}} > (4, 4)$ GeV	13.4 nb
$B^+ \to J/\psi(\mu^+\mu^-)K^+$	2.5M	$p_{\mathrm{T}} > (2.5, 2.5)$ MeV	1.9 μb

Table 3.5: Details of Monte Carlo samples for the signal and various backgrounds in 2012.

As shown in Section 3.8, the 2011 cuts are not optimized for 2012 data. As the center of mass energy and the pile-up condition grow, there is much more background in the B_c analysis region. To improve the signal to background ratio for 2012 data, the cuts have been re-optimized for the 2012 conditions. The cut values are determined by optimizing the signal over the square root of the signal plus background. The background MC samples were checked for inclusion of signal events to avoid double counting. Individual MC samples are weighted by the corresponding cross sections. The number of events in the five MC background samples, the generator-level cuts on them, and the corresponding cross sections are listed in Table 3.5.

3.9.1 Event selection

In 2012, the Type 1 vertex is not always the true primary vertex any more. Every selected event is still required to be associated with a primary vertex reconstructed from at least 3 tracks, but the primary vertex is chosen to have the smallest three-dimensional impact parameter (a_0) relative to the reconstructed B candidate momentum. The B momentum should point to the primary vertex especially in the longitudinal plane where those reconstructed primary vertices are well separated in space.

3.9.2 J/ψ selection

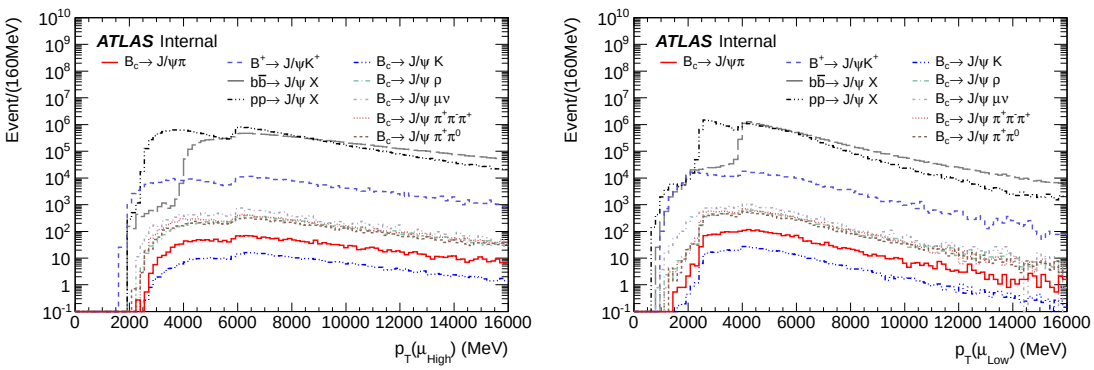

(a) (b)

Figure 3.33: (a) The p_{T} distribution of the higher p_{T} muon. (b) The p_{T} distribution of the lower p_{T} muon.

The 2012 di-muon pairs are still selected with transverse momentum thresholds of (6, 4) GeV (Figure 3.33). The muon tracks are required to pass the 2012 ID hits requirements [70] instead of the 2011 ID hits requirements, with offline cuts on the number of pixel hits (larger than 1) and the number of SCT hits (larger than 6). The di-muon mass is required to be within a 3σ window around the J/ψ PDG mass in each

η range (see Figures 3.34–Figure 3.45) with a loose vertex cut of $\chi^2/N.d.o.f. < 15$.

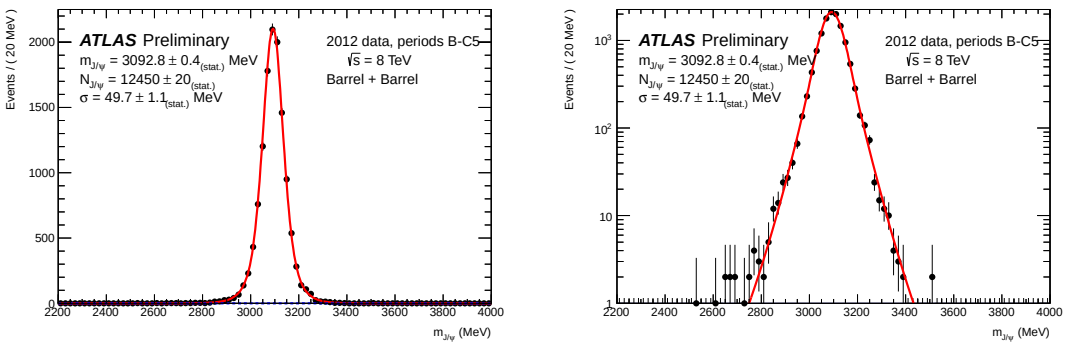

(a) (b)

Figure 3.34: The J/ψ candidate invariant mass distribution, for events in which both muons are in the barrel region, with linear scale (a) and with log scale (b), for the periods B–C5. The distributions are fitted with an unbinned maximum likelihood fit (solid line) with a sum of Gaussian and Crystal Ball functions for the signal plus a linear function for the background (dotted line).

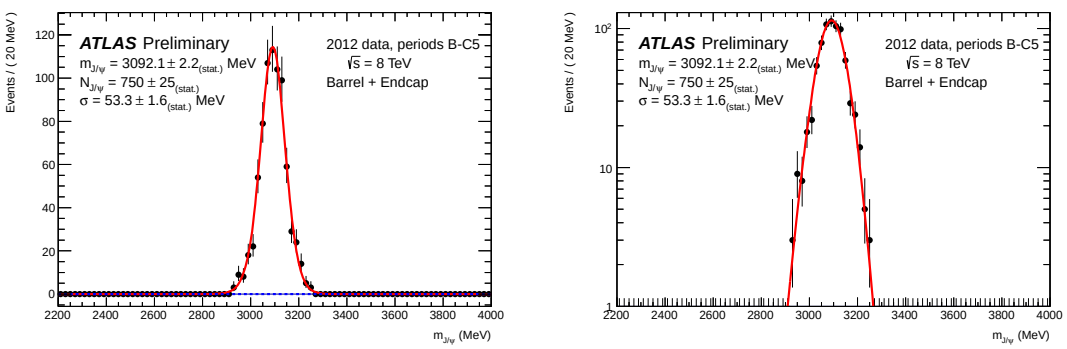

(a) (b)

Figure 3.35: The J/ψ candidate invariant mass distribution, for events in which one muon in barrel and one muon in endcap, with linear scale (a) and with log scale (b), for the periods B–C5. The distributions are fitted with an unbinned maximum likelihood fit (solid line) with a sum of Gaussian and Crystal Ball functions for the signal plus a linear function for the background (dotted line).

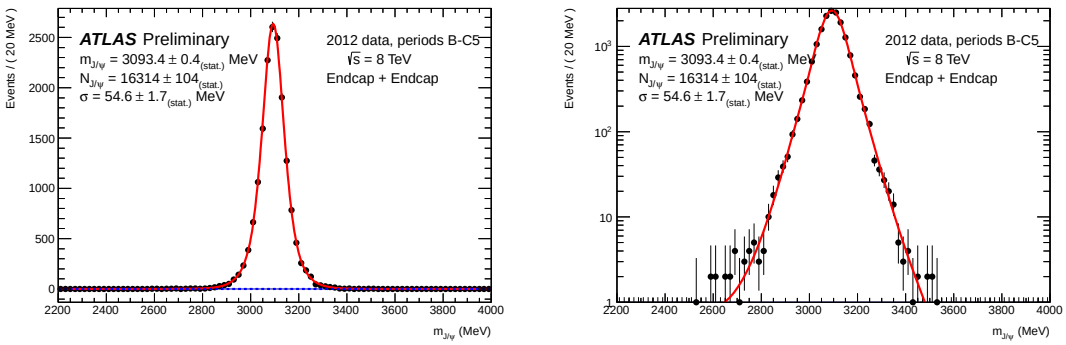

(a) (b)

Figure 3.36: The J/ψ candidate invariant mass distribution, for events in which both muons are both in endcap region, with linear scale (a) and with log scale (b), for the periods B–C5. The distributions are fitted with an unbinned maximum likelihood fit (solid line) with a sum of Gaussian and Crystal Ball functions for the signal plus a linear function for the background (dotted line).

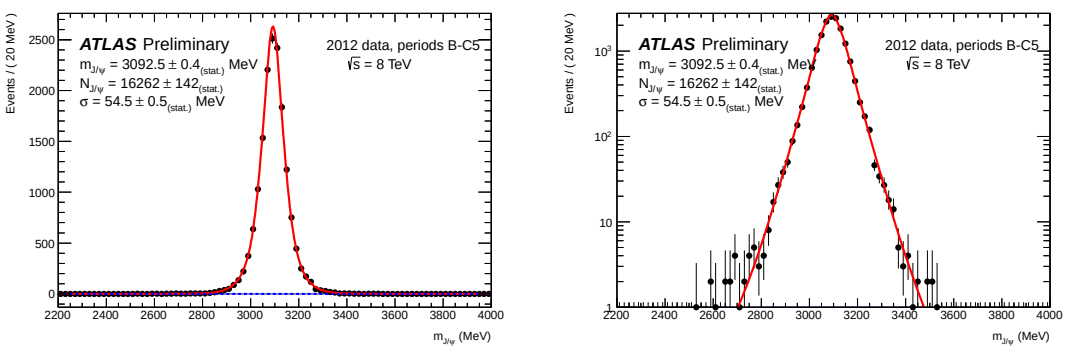

(a) (b)

Figure 3.37: The J/ψ candidate invariant mass distribution, for all candidates, with linear scale (a) and with log scale (b), for the periods B–C5. The distributions are fitted with an unbinned maximum likelihood fit (solid line) with a sum of Gaussian and Crystal Ball functions for the signal plus a linear function for the background (dotted line).

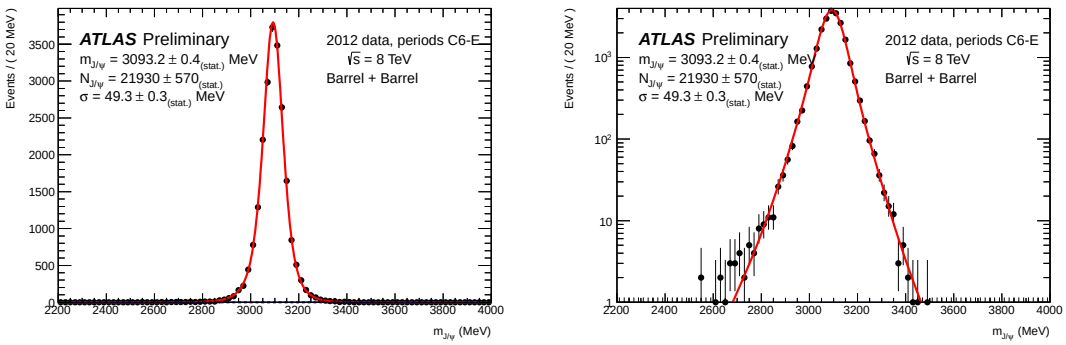

(a) (b)

Figure 3.38: The J/ψ candidate invariant mass distribution, for events in which both muons are in the barrel region, with linear scale (a) and with log scale (b), for the periods C6–E. The distributions are fitted with an unbinned maximum likelihood fit (solid line) with a sum of Gaussian and Crystal Ball functions for the signal plus a linear function for the background (dotted line).

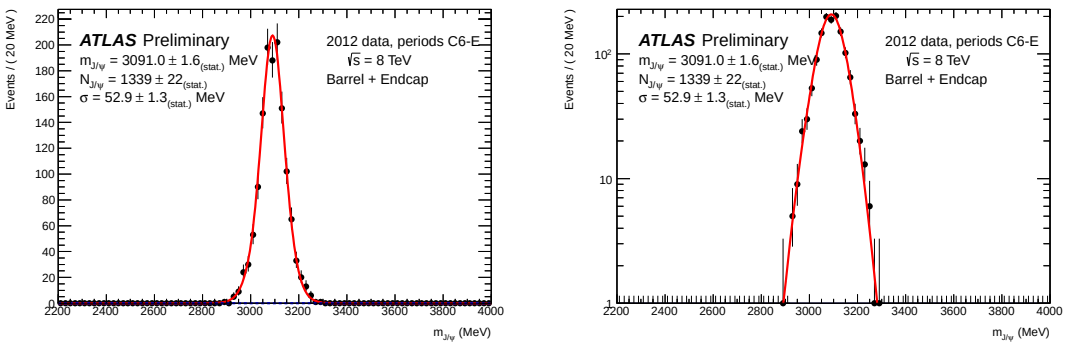

(a) (b)

Figure 3.39: The J/ψ candidate invariant mass distribution, for events in which one muon in barrel and one muon in endcap , with linear scale (a) and with log scale (b), for the periods C6–E. The distributions are fitted with an unbinned maximum likelihood fit (solid line) with a sum of Gaussian and Crystal Ball functions for the signal plus a linear function for the background (dotted line).

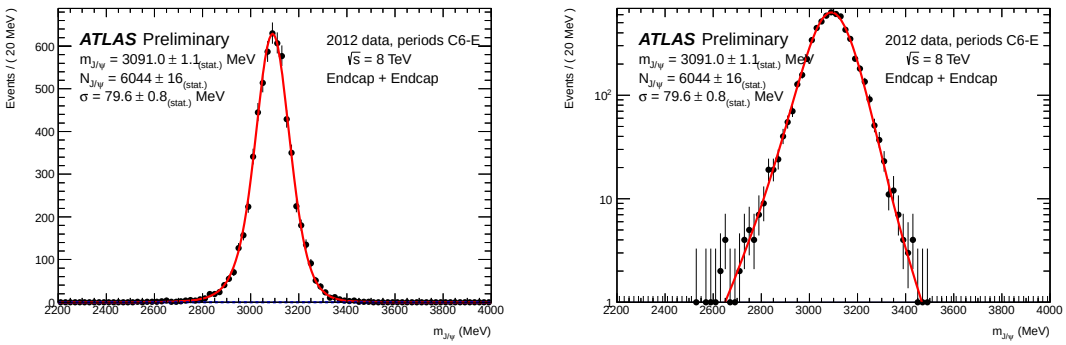

(a) (b)

Figure 3.40: The J/ψ candidate invariant mass distribution, for events in which both muons are both in endcap region, with linear scale (a) and with log scale (b), for the periods C6–E. The distributions are fitted with an unbinned maximum likelihood fit (solid line) with a sum of Gaussian and Crystal Ball functions for the signal plus a linear function for the background (dotted line).

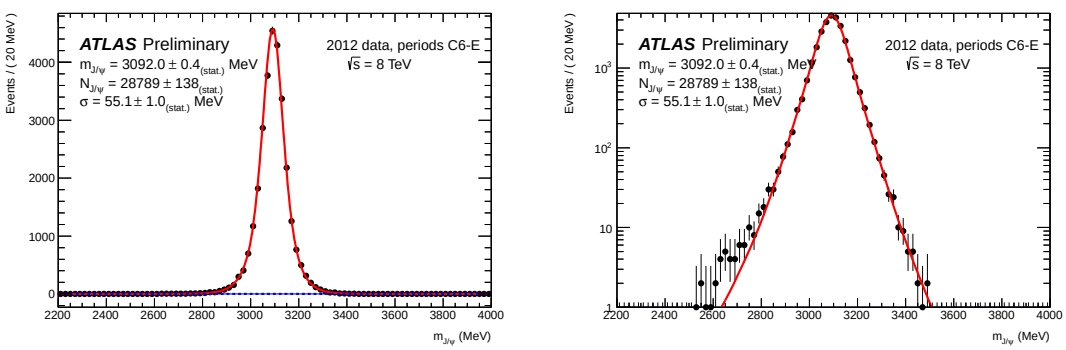

(a) (b)

Figure 3.41: The J/ψ candidate invariant mass distribution, for all candidates, with linear scale (a) and with log scale (b), for the periods C6–E. The distributions are fitted with an unbinned maximum likelihood fit (solid line) with a sum of Gaussian and Crystal Ball functions for the signal plus a linear function for the background (dotted line).

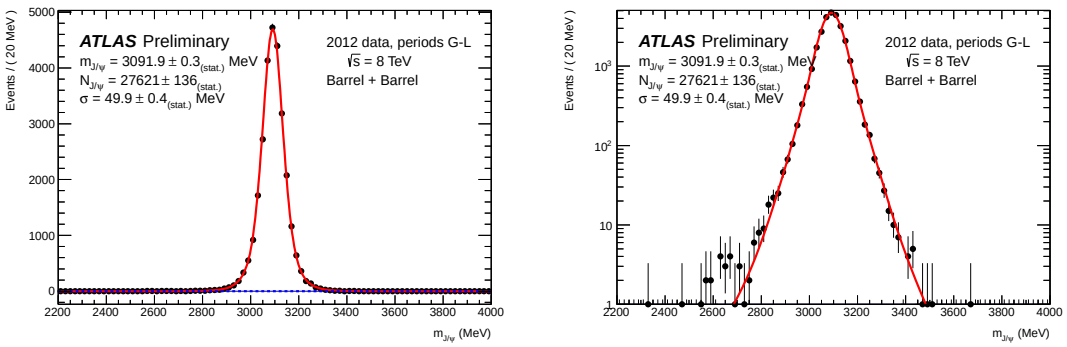

(a) (b)

Figure 3.42: The J/ψ candidate invariant mass distribution, for events in which both muons are in the barrel region, with linear scale (a) and with log scale (b), for the periods G–L. The distributions are fitted with an unbinned maximum likelihood fit (solid line) with a sum of Gaussian and Crystal Ball functions for the signal plus a linear function for the background (dotted line).

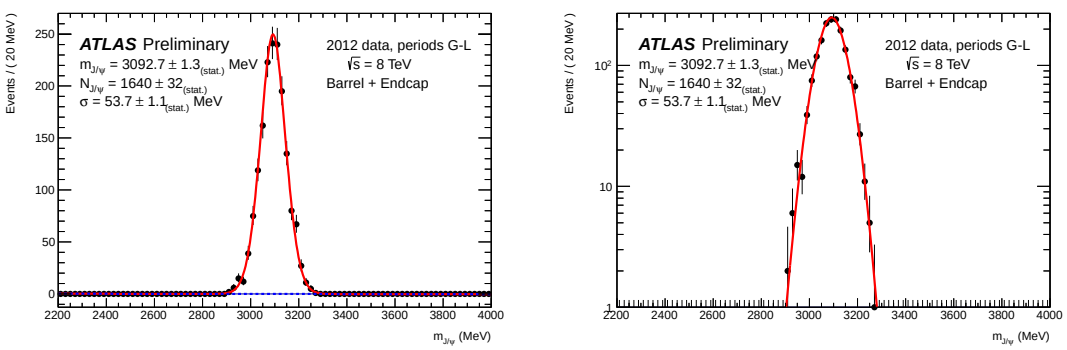

(a) (b)

Figure 3.43: The J/ψ candidate invariant mass distribution, for events in which one muon in barrel and one muon in endcap, with linear scale (a) and with log scale (b), for the periods G–L. The distributions are fitted with an unbinned maximum likelihood fit (solid line) with a sum of Gaussian and Crystal Ball functions for the signal plus a linear function for the background (dotted line).

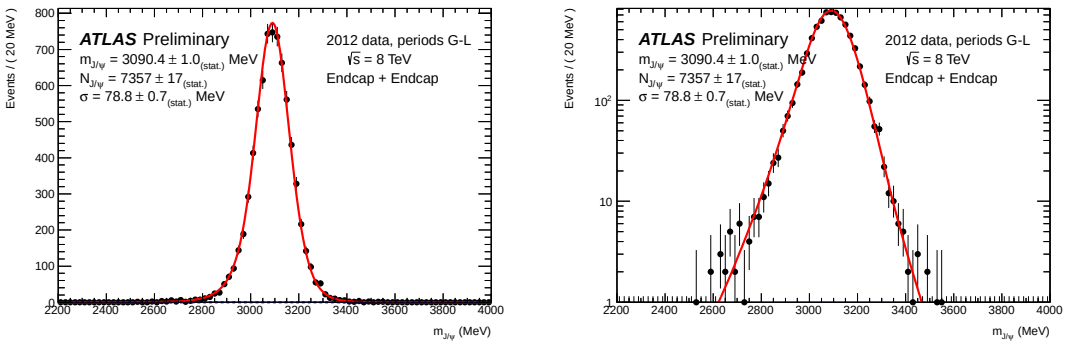

(a) (b)

Figure 3.44: The J/ψ candidate invariant mass distribution, for events in which both muons are both in endcap region, with linear scale (a) and with log scale (b), for the periods G–L. The distributions are fitted with an unbinned maximum likelihood fit (solid line) with a sum of Gaussian and Crystal Ball functions for the signal plus a linear function for the background (dotted line).

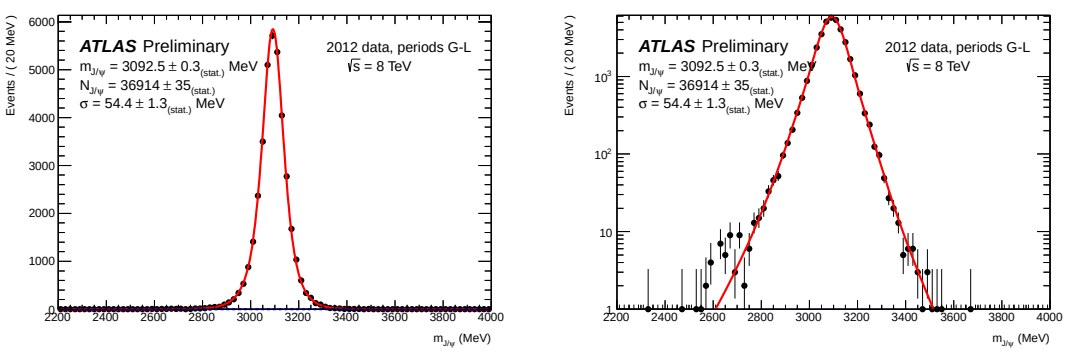

(a) (b)

Figure 3.45: The J/ψ candidate invariant mass distribution, for all candidates, with linear scale (a) and with log scale (b), for the periods G–L. The distributions are fitted with an unbinned maximum likelihood fit (solid line) with a sum of Gaussian and Crystal Ball functions for the signal plus a linear function for the background (dotted line).

Data-taking periods	J/ψ mean MeV	BB sigma, MeV	BE sigma MeV	EE sigma MeV	Yield
B–C5	$3092.5\pm0.4_{stat}$	$49.7\pm1.1_{stat}$	$53.3\pm1.6_{stat}$	$54.6\pm1.7_{stat}$	318900
C6–E	$3092.0\pm0.4_{stat}$	$49.3\pm0.3_{stat}$	$52.9\pm1.3_{stat}$	$79.6\ \pm0.8_{stat}$	488000
G–L	$3092.5\pm0.3_{stat}$	$49.9\pm0.4_{stat}$	$53.7\pm1.1_{stat}$	$78.8\ \pm0.7_{stat}$	524200

Table 3.6: The summary table of the mean of the J/ψ invariant masses and the Gaussian widths (BB: both muons in barrel; BE: one muon in barrel, one muon in endcap; EE: both muons in endcap) and yields for every data taking period. The masses are consistent from period to period. The differences above the statistical error may give an impression of the order of the detector-related systematics.

3.9.3 Hadronic track and B candidate selection

The cut values are chosen as maxima of the $S/\sqrt{S+B}$ plots as shown in Figure 3.47. S here refers to the number of MC signal events surviving a given cut value (with all the other cuts applied), B refers to the corresponding number of background MC events surviving the given cut value (with all the other cuts applied) scaled accordingly to the production cross section relative to the signal channel.

The transverse momentum of the reconstructed B candidates is higher in the 2012 MC than in the 2011 MC as is shown in Figure 3.46(a). The cut value of 18 GeV was selected as the lowest possible value around the maximum of the cut efficiency of the $p_{\mathrm{T}}(B_c)$ shown in Figure 3.47(a).

According to a study of the performance of the track and vertex reconstruction in the high pile-up condition [68], the total number of silicon hits of a hadronic track (Figure 3.46(b)) should be larger than 8 to reduce the fake rate of the reconstructed tracks and vertex. The plateau shown reflects the implied ID hit requirements. The final value is taken to be larger than 9 to optimize the signal over the square root of signal plus background (Figure 3.47(b)).

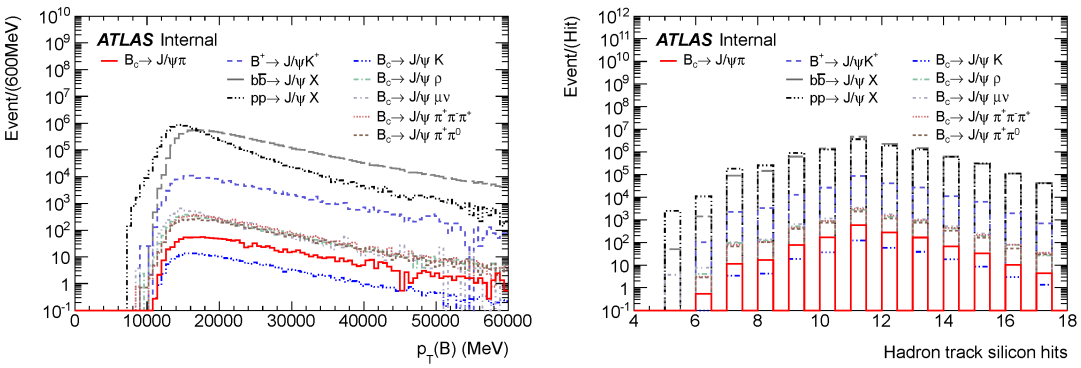

(a)

(b)

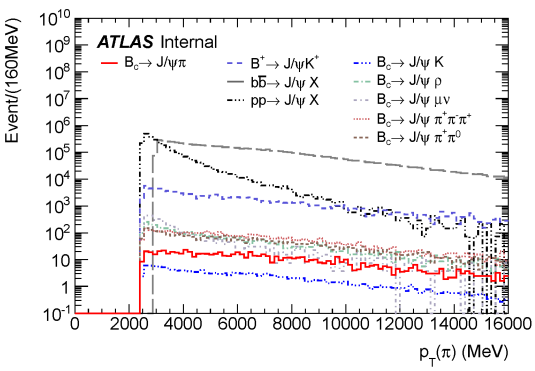

(c)

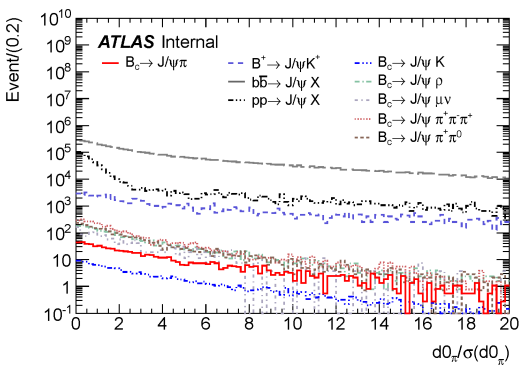

(d)

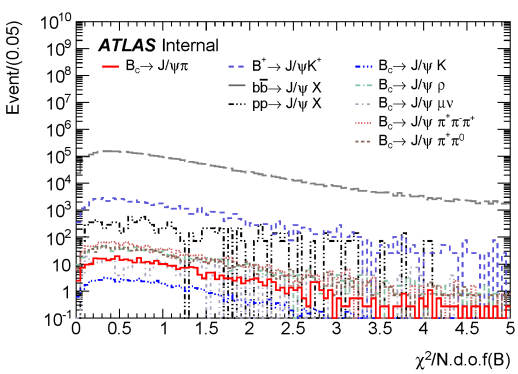

(e)

Figure 3.46: The Monte Carlo distributions of the B_c signal and all of the background channels. (a) The p_{T} of the hadronic track. (b) The total amount of Inner Detector silicon hits. (c) The track transverse momentum. (d) The track transverse impact parameter significance ($d^0_{xy}/\sigma(d^0_{xy})$). (e) The $\chi^2/N.d.o.f.$ of the reconstructed B vertex.

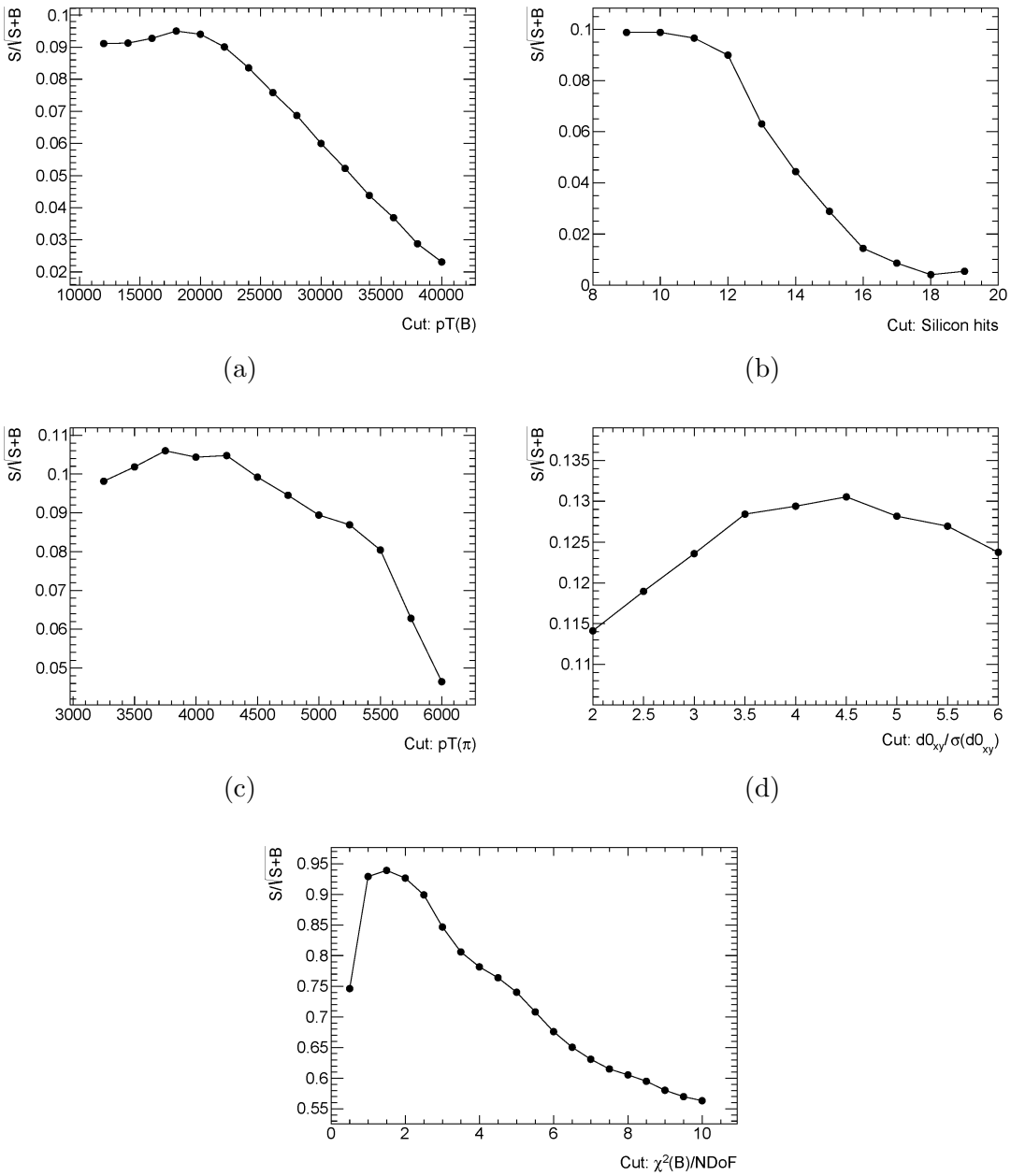

Figure 3.47: The signal over the square root of signal plus background distribution versus $p_{\mathrm{T}}(B)$ (a), number of the track silicon hits (b), track p_{T} (c), $d^0_{xy}/\sigma(d^0_{xy})$ (d), and $\chi^2/N.d.o.f.$ (e).

The cut value of $d^0_{xy}/\sigma(d^0_{xy})$ is chosen to be higher than 4.5, according to Figure 3.46(d). Lowering this cut value results in a steep increase of the background in the $B_c(2S)$ signal region due to the contribution from the random prompt J/ψ combinations.

As is shown in Figure 3.46(e), with other cuts applied, the direct J/ψ background has been highly suppressed while the $b\bar{b}$ background has not. Thus based on Figure 3.47(e), the cut value on $\chi^2/N.d.o.f.$ must be tightened to reduce the $b\bar{b}$ background. On average about 0.05 additional ground state candidates per event have been removed.

3.9.4 B_c excited state selection

The 2012 selection begins identically to the 2011 selection. Then, to improve the track association with the primary vertex in 2012, the difference in the longitudinal impact parameter ($z0$) of the hadronic tracks and the leading muon is required to be less than 1 mm. Tight offline track quality cuts on the number of silicon holes (equal to 0) and number of silicon hits (larger than 8) are applied to reduce the fake rate for the much higher pile-up condition in 2012 [68].

3.10 Selection summary

	2011 data	2012 data
PV	tracks> 3, Type 1	tracks > 3, smallest a_0 to the B momentum
$\mu^{\pm}$	both are combined muons, 2011 MCP cuts, $p_{\mathrm{T}}(\mu^{\pm}) >$ (6, 4) GeV, Pixel Hits > 0, SCT Hits > 6	both are combined muons, 2012 MCP cuts, $p_{\mathrm{T}}(\mu^{\pm}) >$ (6, 4) GeV, Pixel Hits > 0,SCT Hits > 6
J/ψ	$\lvert M(J/\psi) - PDG\rvert < 3\sigma$ $\chi^2/N.d.o.f(J/\psi) < 15$	$\lvert M(J/\psi) - PDG\rvert < 3\sigma$, $\chi^2/N.d.o.f(J/\psi) < 15$
π	$p_{\mathrm{T}} > 4$ GeV, Pixel Hits > 0, Silicon Hits > 6, $d^0_{xy}/\sigma(d^0_{xy}) > 5$	$p_{\mathrm{T}} > 4$ GeV, Silicon Hits > 9, Silicon Holes < 1 $d^0_{xy}/\sigma(d^0_{xy}) > 4.5$
B	$p_{\mathrm{T}}(B) > 15$ GeV, $\chi^2/N.d.o.f.(J/\psi) < 2$ $\lvert M(B) - PDG\rvert < 3\sigma$ for B_c^*	$p_{\mathrm{T}}(B) > 18$ GeV, $\chi^2/N.d.o.f.(J/\psi) < 1.5$ $\lvert M(B) - PDG\rvert < 3\sigma$ for B_c^*
$\pi^{\pm}$	Pixel Hits > 0, Silicon Hits > 6 $p_{\mathrm{T}} > 400$ MeV, from same PV as B candidates	Silicon Hits > 8, Silicon Holes < 1 $p_{\mathrm{T}} > 400$ MeV, $\Delta z0 < 1$ mm from same PV as B candidates, $\Delta z0 < 1$ mm

Table 3.7: The selection requirements critical for analysis of the 2011 and 2012 data. The quality cuts on the muons in 2011 and 2012 are given by the Muon Combined Performance (MCP) group [69, 70].

3.11 Fit to the mass distribution

3.11.1 Ground state fit

The mean mass and the number of signal events of the $B_c^{\pm}$ ground state are extracted using an unbinned maximum likelihood fit with per event error from the data. The

likelihood function is defined as follows:

$$L = \prod_{i=1}^{N} \left[f_{sig} \mathcal{F}_{sig}(m^i_{J/\psi\pi} | \delta(m^i_{J/\psi\pi})) + (1 - f_{sig}) \mathcal{F}_{bkg}(m^i_{J/\psi\pi}) \right] . \tag{3.2}$$

Here N is the total number of $J/\psi\pi^{\pm}$ candidates in the fitted mass window of $5630 < m(J/\psi\pi) < 6830$ MeV; f_{sig} denotes the fraction of signal candidates; and $\mathcal{F}_{sig}$ and $\mathcal{F}_{bkg}$ are the probability density functions (PDF) that model the $B_c^{\pm}$ signal and background mass shapes, respectively, in this mass window.

For the signal, the mass is modelled with a Gaussian distribution:

$$\mathcal{F}_{sig}(m^i_{J/\psi\pi}) = \frac{1}{\sqrt{2\pi} S \delta m^i_{J/\psi\pi}} exp \left(\frac{-(m^i_{J/\psi\pi} - M_{B_c})^2}{2 S \delta m^i_{J/\psi\pi}} \right) . \tag{3.3}$$

Here M_{B_c} is the hypothesized mass of the B_c meson. Its width is the product of the scale factor S times the mass error $\delta m^i_{J/\psi\pi}$. The scale factor S accounts for the differences between the per-event errors on the candidate masses (calculated from tracking parameters) and the overall mass resolution; ideally its value is 1. The mass error $\delta m^i_{J/\psi\pi}$ is calculated for each $J/\psi\pi$ candidate from the covariance matrix associated with the three-track vertex fit. The main contributions to the background are the combinatorial events corresponding to a linear shape and the B^+ tail. The background is modelled using an exponential distribution:

$$\mathcal{F}_{bkg}(m^i_{J/\psi\pi}) = \exp(c \cdot m^i_{J/\psi\pi}). \tag{3.4}$$

The fit has four free parameters: f_{sig}, M_{B_c}, S, and c. Their values and covariance matrix returned by the fit are used to calculate the number of B_c signal decays N_{sig}, the mass resolution σ_M, and the number of background events N_{bkg} in the mass interval $M_{B_c} \pm 3\sigma_M$. The mass resolution σ_M is defined as the width of the B_c mass distribution for which the integral of F_{signal} retains 68.3% of N_{sig} symmetrically around the fitted mass M_{B_c}. The uncertainty on σ_M is calculated using the covariance matrix of the fit.

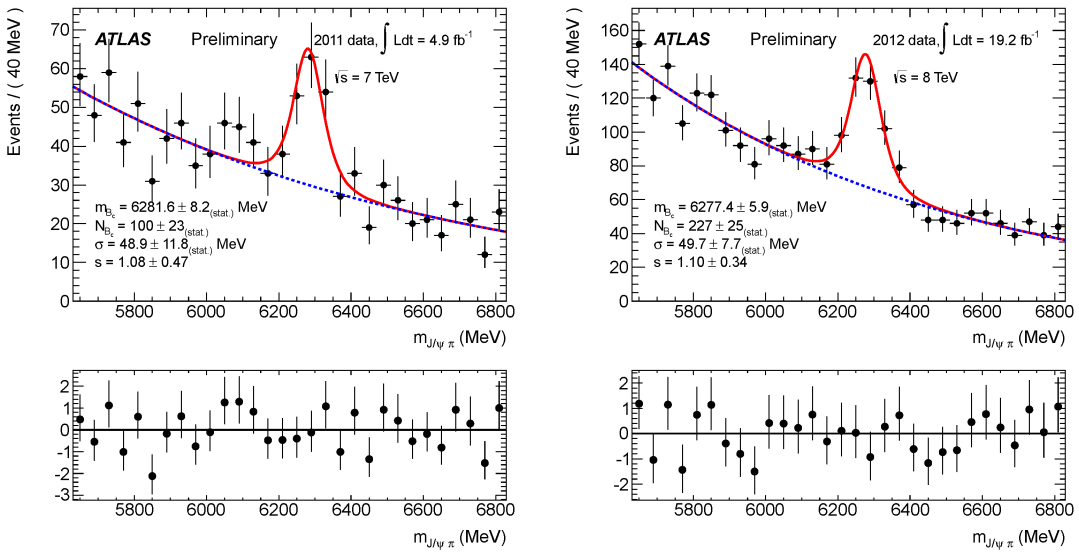

(a) (b)

Figure 3.48: Invariant mass distributions of the reconstructed $B_c^{\pm} \to J/\psi\pi^{\pm}$ candidates in 2011 data [19] (a) and in 2012 data (b). The data are points with error bars. The solid line is the projection of the results of the unbinned maximum likelihood fit for all candidates in the mass window of 5630 to 6820 MeV. The dashed line is the projection of the background component of the same fit.

The results of the B_c ground state mass fits (Figure 3.48) are summarized in Table 3.8.

Year	Signal events	Peak mean, MeV	Peak width, MeV
2011	$100\pm23_{stat.}$	$6282\pm8_{stat.}$	$49\pm12_{stat.}$
2012	$227\pm25_{stat.}$	$6277\pm6_{stat.}$	$50\pm8_{stat.}$

Table 3.8: The results of the unbinned maximum likelihood fits to the invariant mass distribution of the $B_c^{\pm}$ candidates.

The $B^{\pm}$ ground state candidates in the cross check are reconstructed in exactly the same way as the B_c, except the kaon mass is attributed to the hadronic track instead of the pion mass. Figure 3.49 shows the invariant mass distributions for the $B^{\pm}$ candidates with 2011 (left) and 2012 (right) data. The mean mass and the

number of signal events of the $B^{\pm}$ ground state are extracted using an unbinned maximum likelihood fit with per event error from the data as well. The likelihood function is defined as follows:

$$L = \prod_{i=1}^{N} \left[f_{sig} \mathcal{F}_{sig}(m^i_{J/\psi K} | \delta(m^i_{J/\psi K})) + (1 - f_{sig}) \mathcal{F}_{bkg}(m^i_{J/\psi K}) \right]. \tag{3.5}$$

Here N is the total number of $J/\psi K$ candidates in the fitted mass window of $5040 < m(J/\psi K) < 5840$ MeV; f_{sig} denotes the fraction of signal candidates; and $\mathcal{F}_{sig}$ and $\mathcal{F}_{bkg}$ are the probability density functions (PDF) that model the $B^{\pm}$ signal and background mass shapes, respectively, in this mass window.

Like the B_c, the $B^{\pm}$ signal is modelled with a Gaussian distribution:

$$\mathcal{F}_{sig}(m^i_{J/\psi K}) = \frac{1}{\sqrt{2\pi} S \delta m^i_{J/\psi K}} \exp\left(\frac{-(m^i_{J/\psi K} - M_{B^{\pm}})^2}{2 S \delta m^i_{J/\psi K}} \right), \tag{3.6}$$

where $M_{B^{\pm}}$ is the hypothesized mass of the $B^{\pm}$ meson. Its width is the product of the scale factor S times the mass error $\delta m^i_{J/\psi K}$. For the background, there are several contributions:

- The combinatorial background from the $b\bar{b}$ decay. It is described by an exponential distribution:

$$\mathcal{F}_{bkg1}(m^i_{J/\psi K}) = \exp(c \cdot m^i_{J/\psi K}). \tag{3.7}$$

- Partially reconstructed $B^{\pm}$ candidates (e.g. $B^{+/0} \to J/\psi (K^*/K^+\pi)^{+/0}$). This is described by a complementary error function distribution:

$$\mathcal{F}_{bkg2}(m^i_{J/\psi K}) = \frac{2}{\sqrt{\pi}} \int_{\frac{m^i_{J/\psi K} - \mu}{s}}^{\infty} e^{-t^2} \mathrm{d}t, \tag{3.8}$$

  where μ (~ 5130 MeV) and s are respectively its mean and standard deviation.

- The Cabibbo suppressed decay $B^{\pm} \to J/\psi\pi$ is modelled with a Gaussian distribution:

$$\mathcal{F}_{bck3}(m^i_{J/\psi K}) = \frac{1}{\sqrt{2\pi} \sigma m^i_{J/\psi K}} \exp\left(\frac{-(m^i_{J/\psi K} - m_0)^2}{2 \sigma m^i_{J/\psi K}} \right), \tag{3.9}$$

where m_0 is fixed to 5360 MeV from the PDG.

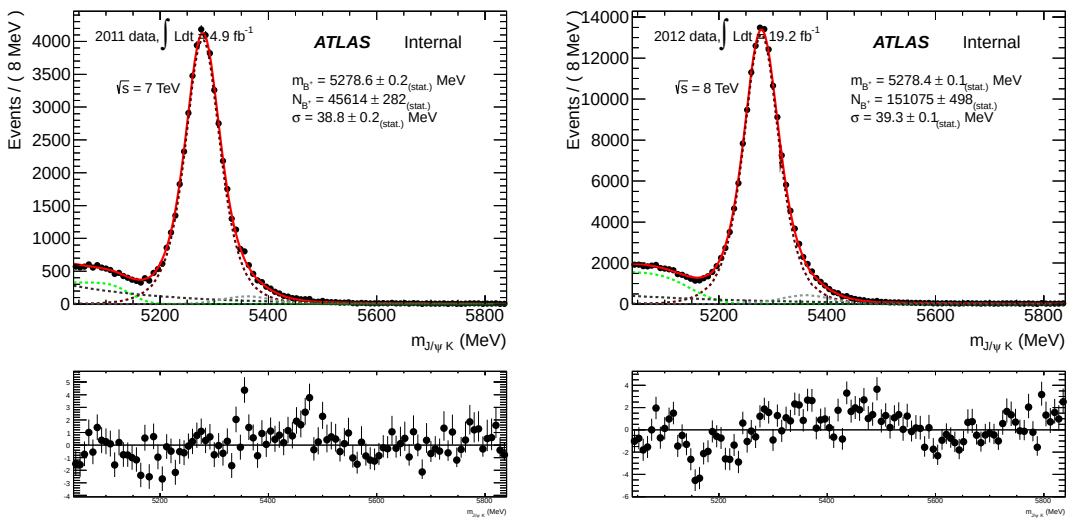

(a) (b)

Figure 3.49: Invariant mass distributions of the reconstructed $B^{\pm} \to J/\psi K^{\pm}$ candidates in 2011 (left) and 2012 (right) data. The data are points with error bars. The solid line is the projection of the results of the unbinned maximum likelihood fit for all candidates in the mass window 4800 to 5800 MeV. The dashed line is the projection of the background component of the same fit.

Year	Signal events	Peak mean, MeV	Peak width, MeV
2011	$45614 \pm 282_{stat.}$	$5278.6 \pm 0.2_{stat.}$	$38.8 \pm 0.2_{stat.}$
2012	$151075 \pm 408_{stat.}$	$5278.4 \pm 0.1_{stat.}$	$39.3 \pm 0.1_{stat.}$

Table 3.9: The results of the unbinned maximum likelihood fits to the invariant mass distribution of the $B^{\pm}$ candidates.

The fit has seven free parameters: f_{sig}, $M_{B^{\pm}}$, S, c, μ, s, and σ. Their values and covariance matrix returned by the fit are used to calculate the number of $B^{\pm}$ signal decays N_{sig} and the mass resolution σ_M. Like the B_c fit, the mass resolution σ_M is defined as the width of the $B^{\pm}$ mass distribution for which the integral of F_{signal} retains 68.3% of N_{sig} symmetrically around the fitted mass $M_{B^{\pm}}$. The uncertainty on σ_M is calculated using the covariance matrix of the fit.

The total number of signal events, central value, and width resulting from the $B^{\pm}$ mass fit (Figure 3.49) are summarized in Table 3.9. The central mass value extracted from the fit is consistent with the PDG value.

3.11.2 Excited B state fit

Slightly differently than for the excited B_c state, the cross check channel excited B states [55, 56] candidates are formed by combining the ground state candidate with a single hadronic track from the primary vertex of reconstructed $B^{\pm}$ candidates. The excited B states are sought in the mass difference distribution $Q = m(B^{\pm}K^{\mp}) - m(B^{\pm}) - m_{PDG}(K)$ for the proper charge combinations $B^{\pm}K^{\mp}$. This technique has the advantage that various uncertainties propagated from the ground state candidates to the excited state candidates cancel.

Two resonances, the B_{s1} ($m_{PDG}(B_{s1}) = 5828.7 \pm 0.4$ MeV) and B^2_{s2} ($m_{PDG}(B_{s1}) = 5839.96 \pm 0.20$ MeV) [23] have been fitted. The two signals are modeled by Gaussians and the background is modeled by a threshold function. The fitted mass difference distribution is shown in Figure 3.50, and the wrong charge combinations are shown in Figure 3.51.

The Q values of the B_{s1} and B^*_{s2} states are in good agreement with the PDG values and with each other between those two years. Because the cuts are optimized for the B_c, not the B^+, the signal is low in 2011.

The excited B_c state is sought in the mass difference distribution $Q = m(B_c^{\pm}\pi\pi) - m(B_c^{\pm}) - 2m_{PDG}(\pi)$ for the proper charge combinations $B_c^{\pm}\pi^+\pi^-$.

For the proper charge combinations, an unbinned maximum likelihood fit is performed. Due to the dominance of the detector resolution, if the resonance is fitted with a sum of Gaussian and Breit-Wigner functions, the Breit-Wigner contribution is

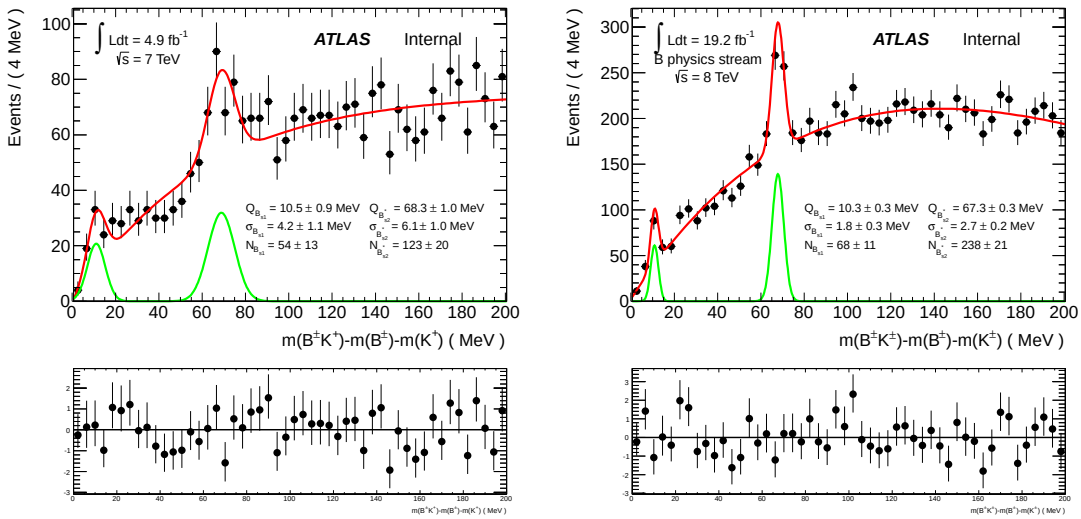

(a) (b)

Figure 3.50: The $m(B^{\pm}K) - m(B^{\pm}) - m_{PDG}(K)$ mass difference distribution for the proper charge combinations in 2011 data (a) and 2012 data (b). The data are points with error bars. The solid line is the projection for the results of the unbinned maximum likelihood fit for all candidates in the range [0, 210] MeV.

found to be negligible, so the Gaussian function alone is used for the signal. The distributions of the wrong charge combinations in 2011 and 2012 are shown on the same plots in Figure 3.52 with the total number normalized to the background number of the proper charge combination, taken from the fit. The background is modelled with a third order polynomial. Alternative functions have been used to estimate the systematics.

As was discussed in Section 1.2.2, the 2^3S_1 decay will result in a negative shift of about 30 MeV in the Q value distribution relative to the 2^1S_0 decay. Given the approximatly 10 MeV shift in the B_c mass between the 1^3S_1 state and the 1^1S_0 state, in total the 1^3S_1 state in the Q value distribution should be about 20-40 MeV to the left of the 1^1S_0 state. For an 18 MeV resolution (obtained from a simple Gaussian fit), these two peaks can not be separated.

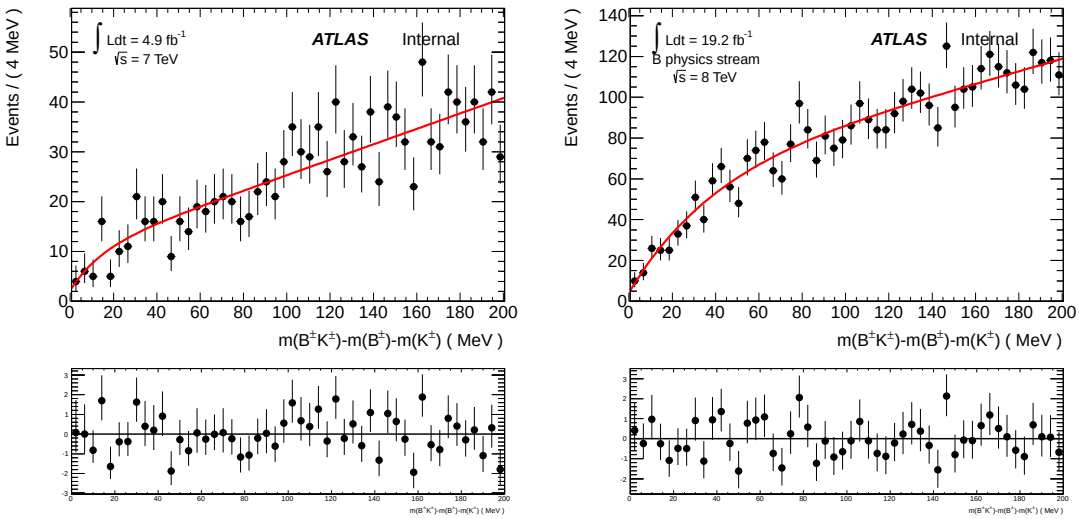

(a) (b)

Figure 3.51: The $m(B^{\pm}K) - m(B^{\pm}) - m_{PDG}(K)$ mass difference distribution for the wrong charge combinations in 2011 data (a) and 2012 data (b). The data are points with error bars. The solid line is the projection of the results of the unbinned maximum likelihood fit to all candidates in the range [0, 210] MeV.

The production cross section of the 2^3S_1 state is about two to three times higher to the 2^1S_0 state. Thus we expect about six 2^1S_0 candidates in 2011 and about ten 2^1S_0 candidates in 2012. These should contribute to the right of the 2^3S_1 peak. At low statistics, this small peak can not be extracted by an additional Gaussian.

The total likelihood function is given as:

$$-\ln L \;=\; -\sum_{i=1}^{N} \ln(N_{sig}\,\mathcal{F}_{sig}(Q^i) + N_b\,\mathcal{F}_{bkg}(Q^i)) + (N_{sig}+N_{bkg}) - N\ln\left(N_{sig}+N_{bkg}\right), \tag{3.10}$$

where

$$\mathcal{F}_{sig}(Q^i) = \frac{1}{\sqrt{2\pi}\sigma} exp\left(\frac{-(Q^i - Q^0)^2}{\sigma}\right), \tag{3.11}$$

and

$$\mathcal{F}_{bkg}(Q^i) = a_0 + a \times Q^i + b \times (Q^i)^2 + c \times (Q^i)^3. \tag{3.12}$$

Here $Q = m(B_c^{\pm}\pi\pi) - m(B_c^{\pm}) - 2m_{PDG}(\pi)$; N is the total number of entries; N_{sig}

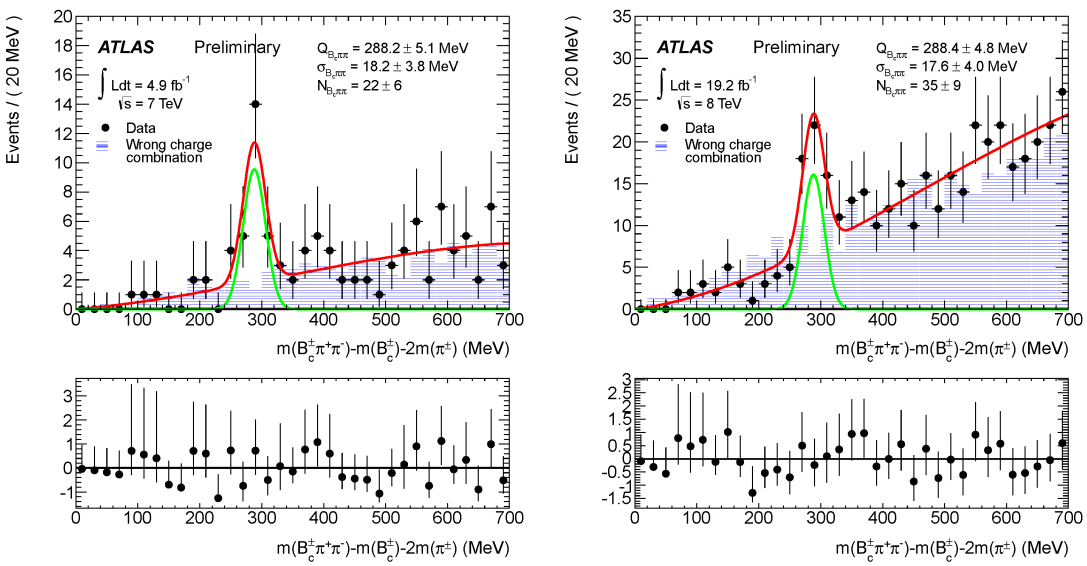

(a) (b)

Figure 3.52: The $m(B_c^{\pm}\pi\pi) - m(B_c^{\pm}) - 2m(\pi_{PDG})$ mass difference distribution for the proper charge combinations (solid dots) and for the wrong charge combinations (dashed squares) in 2011 data (a) and in 2012 data (b). The data are points with error bars. The solid line is the projection of the results of the unbinned maximum likelihood fit for all candidates in the range [0,700] MeV.

denotes the number of signal candidates; N_{bkg} denotes the number of background candidates; Q^0 is the hypothesized mass difference; σ is the Gaussian width; and a, b, and c are the coefficients of the third order polynomial.

As is shown in Figure 3.52, a new structure is clearly seen in the proper charge mass difference distribution but not in the wrong charge combination.

The Q-value of the peaks returned by the fit is 288.2 ± 5.1 MeV in the 2011 data and 288.4 ± 4.8 MeV in the 2012 data, consistent within uncertainty. The fit yields

22 ± 6 signal events in the 2011 data and 35 ± 9 events in the 2012 data. The Gaussian width of the resonance is found to be 18.2 ± 3.8 MeV in the 2011 data, consistent with the 17.6 ± 4.0 in the 2012 data, within uncertainty.

3.12 Systematic uncertainties

There are two sources of fit-related systematics. One comes from the fitting procedure of the B_c ground state and the other involves systematics coming from the fit of the Q value distribution itself. Uncertainty on the mass of the ground state of the $B_c^{\pm}$ is dominated by the fitting procedure and estimated (as described below) to be about 3 MeV. The contribution of the uncertainty on the hadronic momentum p_{T} scale for $B_c^{\pm}$ is 1.2 MeV (Appendix C). The uncertainties associated with the mass of the $B_c^{\pm}$ are largely cancelled in the mass difference distribution. The residual uncertainty of the order of $\Delta m_{B_c} \times (m_{B_c})/m_{B_c(2S)}$ is found to be negligible in comparison with the other contributions.

The contribution of the uncertainty on the hadronic momentum p_{T} scale for the mass difference distribution of the $B_c(2S)$ is 0.15 MeV (Appendix C). The systematic uncertainty on the mass difference introduced by the fitting procedure is estimated by:

- the uncertainty on the B_c ground state mass itself (negligible in the Q-value distribution);
- varying the background model. An exponential threshold function ($f_\theta(x) \sim 1 - e^{-x/\theta}$) and second and fourth order polynomials were considered as alternatives (about 3.4 MeV);
- varying the fit mass range from [0, 700] MeV to [0, 1000] MeV (about 1.2 MeV);

- using different models for the signal. A single Breit-Wigner, a Breit-Wigner combined with a Gaussian, and a double Gaussian were considered (negligible).

The largest difference between any of the variations above and the final fit model is used as the systematic uncertainty.

The various sources of systematic uncertainty are treated as uncorrelated. The total systematic uncertainty propagated to the mass value of the new resonance is estimated to be 4 MeV.

3.13 The significance of the observation of the excited state

The significance calculation is based on the ratio of logs of maximum likelihoods. These are obtained by a fit for the baseline model hypothesis, lnL, and for a particular null hypothesis, lnL^0 [81, 82].

The $-2ln(L/L^0)$ is interpreted as a χ^2 variable to derive the probability of a fluctuation as large as the signal hypothesis, assuming the null hypothesis is true. The number of degrees of freedom is equal to the difference between the hypotheses in the number of floating parameters.

The 2011 and 2012 data are tested separately using the following hypothesis. The model of signal upon background hypothesis is reflected by L, where

$$-\ln L \;=\; -\sum_{i=1}^{N} \ln(N_{sig}\,\mathcal{F}_{sig}(Q^i) + N_b\,\mathcal{F}_{bkg}(Q^i)) + (N_{sig}+N_{bkg}) - N\ln\left(N_{sig}+N_{bkg}\right). \tag{3.13}$$

The Gaussian signal peak is reflected by

$$\mathcal{F}_{sig}(Q^i) = \frac{1}{\sqrt{2\pi}\sigma} exp\left(\frac{-(Q^i - Q^0)^2}{\sigma}\right). \tag{3.14}$$

A third order polynomial background is parameterized as

$$\mathcal{F}_{bkg}(Q^i) = a_0 + a \times Q^i + b \times (Q^i)^2 + c \times (Q^i)^3. \tag{3.15}$$

Here the 7 parameters ($N_{sig},\ N_{bkg},\ Q^0,\ \sigma,\ a,\ b,$ and c) are floating.
The null hypothesis is the third order polynomial background L^0, given by

$$-\ln(L^0) = -\sum_{i=1}^{N}(N_{bkg}\mathcal{F}_{bkg}(Q^i)). \tag{3.16}$$

Here the 4 parameters ($N_{bkg},\ a,\ b,$ and c) are floating.
The difference in the number of degree of freedom associated with L and L^0 is $\Delta N.d.o.f = 3$.

To understand the systematics on this fit, we carry out a separate study in which we replace the background function by a fourth order polynomial:

$$\mathcal{F}_{bkg}(Q^i) = a_0 + a \times Q^i + b \times (Q^i)^2 + c \times (Q^i)^3 + d \times (Q^i)^4, \tag{3.17}$$

Here the 8 parameters ($N_{sig},\ N_{bkg},\ Q^0,\ \sigma,\ a,\ b,\ c,$ and d) are floating.
For the null hypothesis, with this fourth order polynomial background, 5 parameters ($N_{bkg},\ a,\ b,\ c,$ and d) are floating, and $\Delta N.d.o.f. = 3$.

The $-ln(L/L^0)$ is the value at $N_{sig} = 0$ in the profile likelihood ratio [83] (Figure 3.53 (a) for 2011 and Figure 3.53 (b) for 2012). For the plots in Figure 3.52, the significance is 4.58σ in the 2011 dataset and 4.54σ in the 2012 dataset, using the third order polynomial background.

A combined fit is performed to test the total significance. The baseline approach is a fit to the merged 2011 and 2012 dataset. The model of signal upon background is a Gaussian peak and a third order polynomial, including 7 floating parameters (N_{sig},

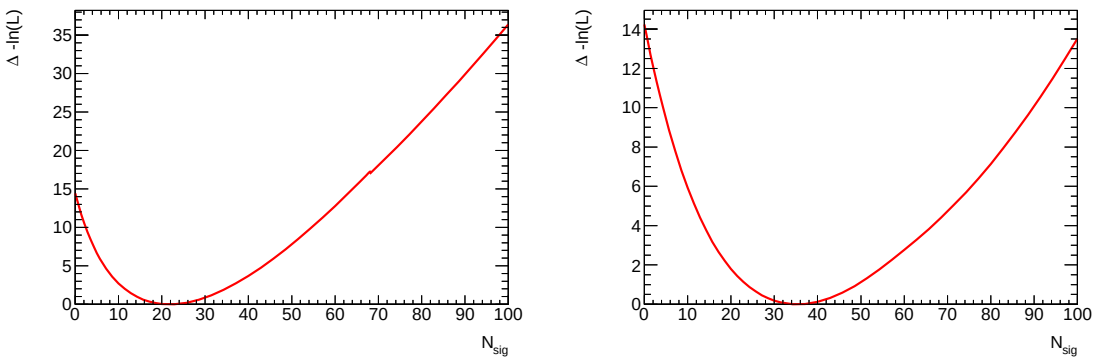

(a) (b)

Figure 3.53: The profile of the negative logarithm of the likelihood ($-ln(L)$) versus N_{sig} for (a) 2011 and (b) 2012 data. The negative log likelihood is offset by its value at the minimum, and this is represented by the symbol Δ on the vertical axis label.

N_{bkg}, Q^0, σ, a, b, c). The null hypothesis is a fourth order polynomial background, including 4 floating parameters (N_{bkg}, a, b, c). Here $\Delta N.d.o.f. = 3$.

We study the stability of this approach with three more conservative choices.

- In method 2, the model for signal upon background is a Gaussian peak and a fourth order polynomial background, including 8 floating parameters (N_{sig}, N_{bkg}, Q^0, σ, a, b, c, d). The null hypothesis is a third order polynomial, including 5 floating parameters (N_{bkg}, a, b, c, d). Here $\Delta N.d.o.f. = 3$.

- The other two approaches involve a simultaneous fit to the individual 2011 and 2012 datasets, where

$$-2ln(L/L^0) = -2[ln(L(A)/L^0(A)) + log(L(B)/L^0(B))]. \tag{3.18}$$

  – In method 3, the model for signal upon background is two Gaussian peaks and two third order polynomials, including 14 floating parameters ($N_{sig}(A)$, $N_{bkg}(A)$, $Q^0(A)$, $\sigma(A)$, $a(A)$, $b(A)$, $c(A)$, $N_{sig}(B)$, $N_{bkg}(B)$, $Q^0(B)$, $\sigma(B)$, $a(B)$, $b(B)$, and $c(B)$). The null hypothesis is two third

order polynomials, including 8 floating parameters ($N_{bkg}(A)$, $a(A)$, $b(A)$, $c(A)$, $N_{bkg}(B)$, $a(B)$, $b(B)$, and $c(B)$). Here $\Delta N.d.o.f. = 6$.

– In method 4, the model for signal upon background is two Gaussian peaks and two fourth order polynomials, including 16 floating parameters ($N_{sig}(A)$, $N_{bkg}(A)$, $Q^0(A)$, $\sigma(A)$, $a(A)$, $b(A)$, $c(A)$, $d(A)$, $N_{sig}(B)$, $N_{bkg}(B)$, $Q^0(B)$, $\sigma(B)$, $a(B)$, $b(B)$, $c(B)$ and $d(B)$). The null hypothesis is two fourth order polynomials, including 10 floating parameters ($N_{bkg}(A)$, $a(A)$, $b(A)$, $c(A)$, $d(A)$, $N_{bkg}(B)$, $a(B)$, $b(B)$, $c(B)$ and $d(B)$). Here $\Delta N.d.o.f. = 6$.

Figure 3.54 is the profile likelihood ratio of the merged dataset.

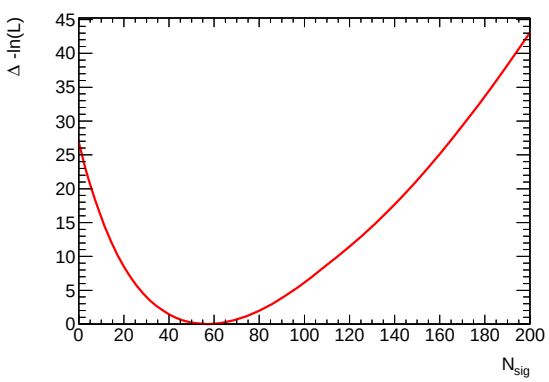

Figure 3.54: The profile of the negative logarithm of the likelihood ($-ln(L)$) versus N_{sig} for the merged 2011 and 2012 data. The negative log likelihood is offset by its value at the minimum, and this is represented by the symbol Δ on the vertical axis label.

The significance calculations are recorded in Table 3.10.

Null Hypothesis	$2 \cdot \Delta(-\ln L)$	ΔNDF	Prob(χ^2)	N_σ
2011 3^{rd} poly	$2 \cdot 14.458$	3	$2.33 \cdot 10^{-6}$	4.58
2011 4^{th} poly	$2 \cdot 11.941$	3	$2.64 \cdot 10^{-5}$	4.04
2012 3^{rd} poly	$2 \cdot 14.241$	3	$2.88 \cdot 10^{-6}$	4.54
2012 4^{rd} poly	$2 \cdot 11.167$	3	$5.56 \cdot 10^{-5}$	3.86
merged 3^{rd} poly	$2 \cdot 26.824$	3	$1.33 \cdot 10^{-11}$	6.66
merged 4^{th} poly	$2 \cdot 20.659$	3	$5.60 \cdot 10^{-9}$	5.71
simul 3^{rd} poly	$2 \cdot 28.699$	6	$1.52 \cdot 10^{-10}$	6.30
simul 4^{rd} poly	$2 \cdot 23.108$	6	$2.68 \cdot 10^{-8}$	5.44

Table 3.10: Significance of the signals, calculated separately for: the 2011 dataset; the 2012 dataset; a fit to the merged 2011 plus 2012 dataset, and a simultaneous fit to the individual 2011 and 2012 datasets.

3.14 Conclusion

The mass difference distribution $m(B_c^{\pm}\pi^+\pi^-) - m(B_c^{\pm}) - 2m_{PDG}(\pi)$ has been reconstructed using data collected by the ATLAS experiment at 7 (8) TeV center of mass energy in 2011 (2012). A new state is observed at mass[1] $6845 \pm 7_{stat.} \pm 4_{syst.}$ MeV. The significance of the observation is 6.7 standard deviations. The mass of the new structure is calculated by summing the PDG mass of the ground state, two times the PDG mass of the pion, and the observed Q-value. Within the uncertainties it is consistent with the predicted mass of the $B_c(2S)$ state. This state is interpreted as the $B_c(2S)$.

[1]The average mass is calculated as the barycenter of the 2011 and 2012 values.

Chapter 4

LHC upgrades for further physics

This chapter describes the plans for the LHC machine and ATLAS detecter upgrades for high luminosity. We described the preparation for increased precision and new physics beyond the Standard Model. New materials and techniques are under investigation, especially for the Pixel detector, as it will face a much harsher radiation environment. Diamond is a candidate for upgrade tracking due to its extreme radiation hardness. To characterize the electrical properties of diamond sensors designed for ATLAS, the leakage current is measured at various bias voltages, for a range of temperatures and irradiation fluences.

4.1 Development of technologies for experiments at the upgraded LHC

Prior to the 2013 shutdown, the LHC was operating with a center-of-mass energy for proton-proton collisions at 8 TeV. This will increase to 14 TeV. A maximum instantaneous luminosity of 10^{34} $\mathrm{cm}^{-2}\mathrm{s}^{-1}$ is planned. In order to achieve an instantaneous

luminosity of 5×10^{34} cm^{-2}s^{-1}, in a few years, the LHC will undergo a series of upgrades towards the High Luminosity LHC (HL-LHC). The detectors will acquire an expected total integrated luminosity of about 3000 fb^{-1} after ten years of HL-LHC operation.

This will enhance studies that require the highest energy scale, such as those of the electroweak symmetry breaking mechanism and signatures of new physics predicted by models such as SUSY and extra dimensions in the TeV region [84, 85]. It will also give unprecedented access to rare B decays.

The LHC is undergoing its first long shutdown during 2013-2014, during which time consolidation of the superconducting circuits of the LHC machine is being performed. Until 2018, the LHC will continue operation at the center-of-mass energy of 13-14 TeV, with an instantaneous luminosity of around 10^{34} cm^{-2}s^{-1}. In the second long shutdown (beginning 2018), injectors and collimators will be upgraded. This will allow the instantaneous luminosity to reach 10^{35} cm^{-2}s^{-1}. Data-taking will resume in 2019. In the third long shutdown (in 2022), the LHC will install IR magnets and crab cavities, to become the HL-LHC.

4.2 ATLAS upgrades

The current ATLAS detector[58] is designed to exploit physics with a center-of-mass energy of the proton-proton collisions up to 14 TeV and a maximum instantaneous luminosity of 10^{34} cm^{-2}s^{-1} [84]. When the LHC upgrades to become the HL-LHC, the radiation environment will be much harsher, and occupancies of detectors will be significantly higher. This requires significant changes to most of the ATLAS systems.

During the 2013-2014 shutdown, detector consolidation work will be done, including the completion of the MS, installation of a new tracker evaporative cooling

plant, and detector maintenance. One important addition is a new Insertable B-Layer (IBL) [86] inside the B-layer of the present pixel detector, at radius 33 mm. For the IBL, newly developed 3D silicon sensors are being used together with planar silicon sensors.

During the 2018 shutdown, new Muon Small Wheels and a finer granularity Level-1 readout for the LAr calorimeter will be installed. The very forward taggers will be upgraded [87].

Following the upgrade to the HL-LHC around 2022, due to the increase in the instantaneous luminosity and the accumulated radiation damage, the Inner Detector will no longer be suitable for operation and will be fully replaced. New technologies and materials with higher granularity, lower material budget, and increased radiation hardness are under investigation for the high occupancy and high radiation environment. Testbeams are underway for those new technologies. New muon and calorimeter electronics will be installed and new trigger schemes will be introduced [85].

4.3 Test beam

To develop technologies for the upgrade, new designs and materials have to be characterized under conditions similar to the LHC. Especially for silicon and diamond sensors, testing is needed since they will be instrumented near the beam, where the radiation environment is extreme.

Tests are done using the 24 GeV proton beam at CERN, the 4 GeV positron beam at DESY, and so forth. Typical testbeams for silicon or diamond pixel sensors are operated with samples installed in the beam line with bias voltage applied and signal monitored using a telescope made of crossed silicon strip sensors plus a scintillator

trigger. For tests of the strip sensors, the alternative setup is to use planar pixel silicon sensors for monitoring. The events are collected under different threshold settings, bias voltages, and temperatures. They are stored for analysis.

4.4 Diamond sensors

4.4.1 Introduction

Diamond is expected to have extreme radiation hardness due to its large band gap (5.5 eV) and displacement energy (42 eV/atom), no leakage current increase with radiation, no space charge to deplete, low capacitance, and a large operational temperature range as shown in Table 4.1.

Properties	Diamond	Silicon
Density (gm^{-3})	3.5	2.32
Band gap (eV)	5.5	1.1
Resistivity (Ω-cm)	$> 10^{12}$	10^3
Breakdown voltage (V/cm)	10^7	10^3
Electron mobility ($cm^3V^{-1}s^{-1}$)	1800	1500
Hole mobility ($cm^3V^{-1}s^{-1}$)	1200	500
Dielectric constant	5.6	11.7
Energy per e-h pair (eV)	13	3.6
Av. min. ionizing signal per 100 μm (e)	3600	8000

Table 4.1: The properties of diamond and silicon.

Diamond is being developed [95] for use in vertexing and tracking detectors for the ATLAS inner layers. Chemical vapor deposition (CVD) diamond has already been used for beam monitoring [93,94]. At distances shorter than about 24 cm from an LHC collision (that covered by pixel layers in ATLAS), the dominant source of radiation damage is charged particles. To characterize candidate technologies for

tracking particles at the HL-LHC, studies are conducted as a function of charged particle fluence up to 10^{16} n_{eq}/cm^2.

At the HL-LHC, the sensors' readout electronics will require cooling for maximal radiation lifespan and optimal operation. Additionally there will be periods of intentional or unintentional warm-up during the lifetime of the detector, and it is important to anticipate their effect.

Since any effect of radiation damage upon the resistivity of the detection material will, if uncompensated, propagate to the leakage current, all assessments of the material properties that depend upon leakage current measurement, including active volume and charge collection distance, must be understood. The resistivity of polycrystalline CVD diamonds has been studied for a range of temperatures and proton fluences.

4.4.2 Irradiation at LANSCE

The irradiation of the diamonds has been done using the 800 MeV proton beam at the Los Alamos Neutron Scattering Center (LANSCE), Los Alamos. The beam spot is a Gaussian of diameter roughly 2 cm.

The radiation fluence is monitored using an array of *pin* semiconductor diodes whose forward voltage is linear with fluence up to 10^{15} p/cm^2. The final fluence is measureed using aluminum foils irradiated simultaneously with each sample [88]. The uncertainty on the measured fluence is less than 30%.

All diamond sensors are irradiated without removal of the metals on both sides, to account for the radiation's effect on the metal as in the real collider.

4.4.3 Test setup

Two CVD polycrystalline diamond sensors are used for this study (Table 4.2). They are taken from the same series 1006115, produced in 2008 by Element Six [96] with metalized pads and backplane (Figure 4.1). The cleaning and metalization process is based on a technique in [97]. That process begins with application of three heavily oxidizing acids to remove all organic residues and leave the surface oxygen terminated. The sequence is HCl-HNO_3 (3:1), H_2SO_4 (3:2), then H_2SO_4-H_2O_2 (1:1). This is followed by an oxygen plasma etch for 4 minutes. After the high energy sputter by composite TiW, the contacts are annealed for another 4 minutes at 450°C in an inert atmosphere. The thicknesses of these two diamond sensors were measured with an Eichhorn and Hausmann Contactless Wafer Thickness and Geometry Gauge (model MX 203-6-33) and confirmed optically with a microscope. Their lengths and widths were measured optically.

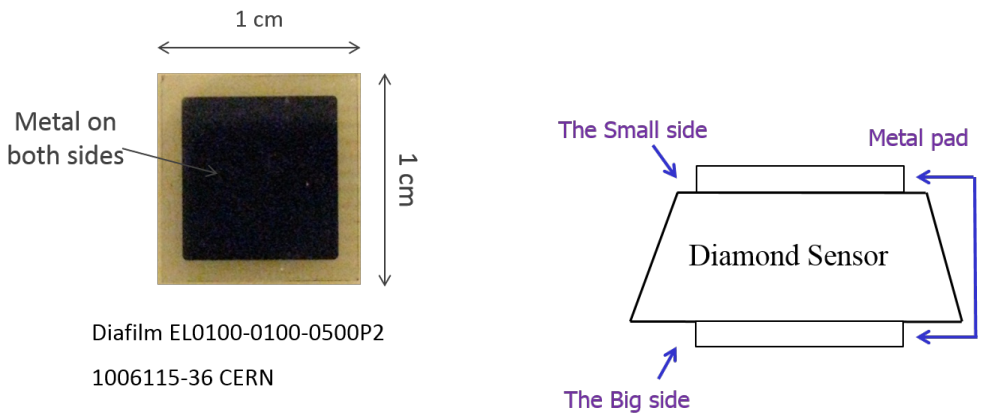

(a) (b)

Figure 4.1: The structure of the diamond sensor. (a) The top view of the sensor and (b) a drawing of the cross section of the sensor (the difference in length between small side and big side is within 0.001 cm).

Two slightly different setups, Figure 4.2, were used for the leakage current versus

Diamond sensor	Dimensions (cm×cm×μm)
1006115-36	$1.016 \times 1.017 \times 440$
1006115-46	$1.007 \times 1.008 \times 432$

Table 4.2: Dimensions and features of the diamond sensors used in this study. Representative uncertainties on these lengths are 0.002 cm on the transverse dimensions and 10 μm on the thickness.

bias voltage measurement in order to quantify the uncertainty associated with the instrument configuration. In both of those setups, the diamond is placed on a thermal chuck inside of a dark box to avoid any effects from light. The high voltage is applied through the probe from the Keithley 237, and the leakage current data are acquired by the Keithley source measure unit (Keithley high voltage source 237 in Configuration 1 or Keithley electrometer 617 in Configuration 2). They are controlled by Laboratory Virtual Instrument Engineering Workbench (LabVIEW). The data are acquired at a rate of one point per second. Dry N_2 is applied continuously to the environment to prevent condensation. The temperature is adjusted through the chuck and measured using a thermal sensor attached to the chuck.

In order to cover the full operational temperature range of the pixel detector in ATLAS, the sensors' temperature is maintained at -10°C, 0°C, 10°C and 20°C by the thermal chuck on which the sensor rests.

Fluence	-10° C	0° C	10° C	20° C
1006115-36 0 p/cm^2	Conf 1	Conf 1	Conf 1	Conf 1
1006115-36 3.85×10^{15} p/cm^2	Conf 1	Conf 1	Conf 1	Conf 1
1006115-36 1.11×10^{16} p/cm^2	Conf 1	Conf 1	Conf 1	Conf 1
1006115-36 1.36×10^{16} p/cm^2	Conf 1	Conf 1	Conf 1	Conf 1
1006115-36 1.63×10^{16} p/cm^2	Conf 2	Conf 2	Conf 1	Conf 1&2
1006115-46 2.76×10^{15} p/cm^2	Conf 2	Conf 2	Conf 2	Conf 2
1006115-46 7.5×10^{15} p/cm^2	Conf 2	Conf 2	Conf 2	Conf 2

Table 4.3: The configuration used for each temperature and fluence point.

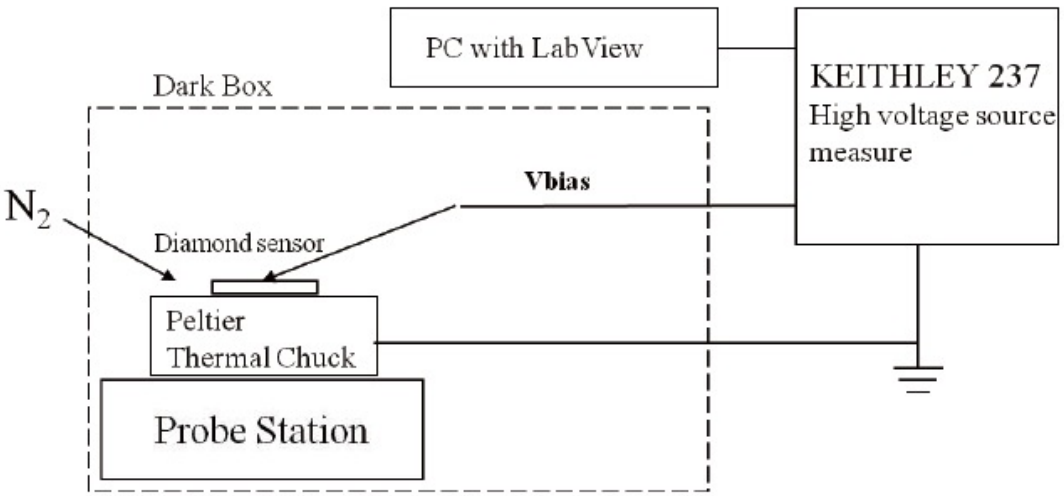

(a) Measurement Configuration 1

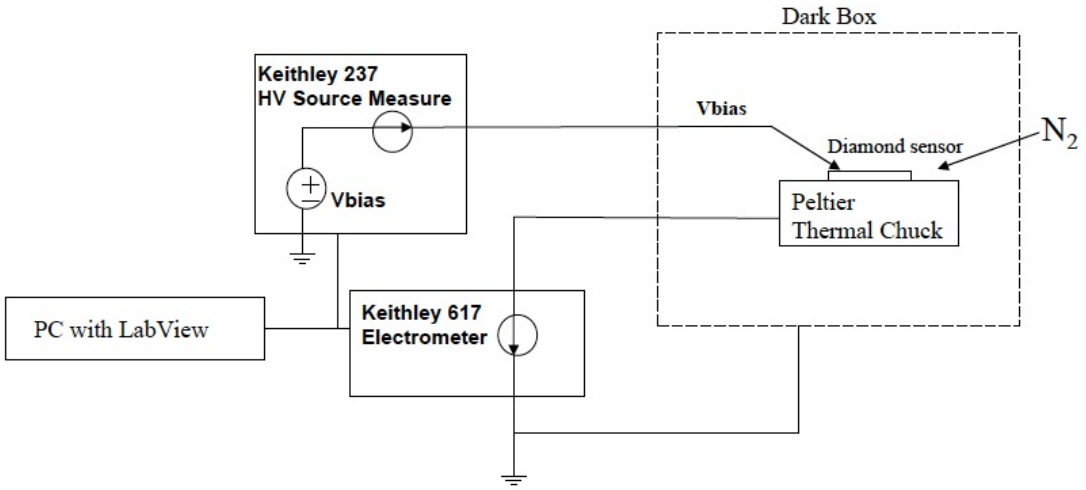

(b) Measurement Configuration 2

Figure 4.2: The experimental setups for measuring leakage current as a function of bias voltage and temperature.

As is shown in Table 4.3, Configuration 2 was used for the measurements of diamond 1006115-36 at fluence 1.63×10^{16} p/cm^2 with temperature points 20°C, 0°C, and −10°C and for diamond 1006115-46 at fluences 2.75×10^{15} p/cm^2 and 7.5×10^{15} p/cm^2 at all temperature points. Measurements of diamond 1006115-36 at 20°C after fluence 1.63×10^{16} p/cm^2 were made with both setups for uncertainty studies.

4.4.4 Electrical breakdown

Diamond 1001615-36 showed breakdown at ±500 V prior to irradiation (e.g. Figure 4.3 (a)) which set the scale for our studies. After being irradiated, the samples do not break down even up to 1000 V (e.g. Figure 4.3 (b)). At a fluence of 1.63×10^{16} p/cm^2, diamond 1006115-36 starts to break down again just above 500 V.

Diamond 1006115-46 shows similar behavior: it breaks down near 500 V before irradiation but remains stable up to 800 V affter irradiation.

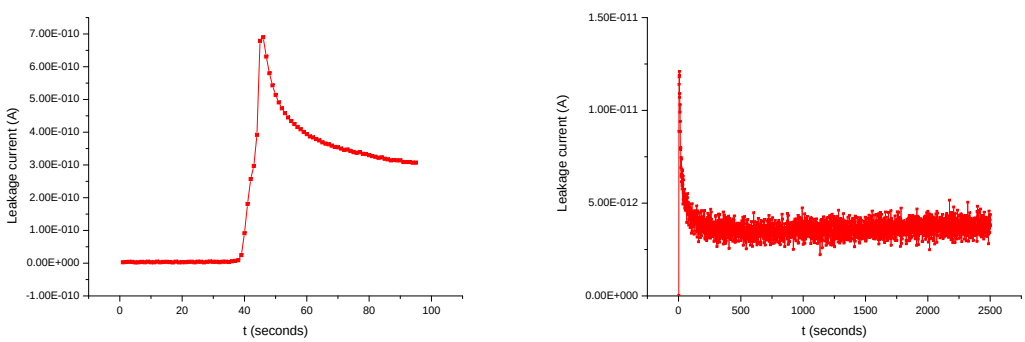

(a) (b)

Figure 4.3: The leakage current of diamond sample 1001615-36 measured at 500V bias before irradiation (a) and after receiving 3.85×10^{15} p/cm^2 (b).

4.4.5 Leakage current

Stability test

Since diamond is an insulator (unlike silicon, which is a semiconductor), it takes a much longer time for the diamond to reach steady state after application of these high voltages. To estimate the time needed for the current to be stable, long-term stability tests were done.

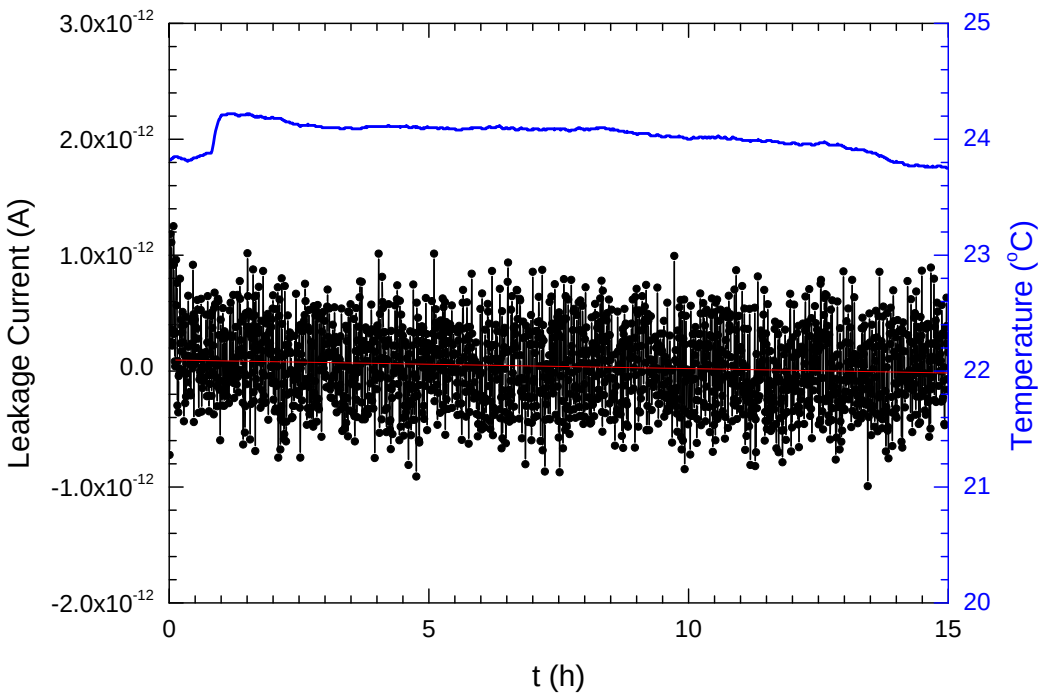

Figure 4.4: This current versus time graph for a typical measurement illustrates the stability of the current. Measurements commence about an hour after the change in bias voltage and are recorded every 30 seconds thereafter. These data were taken at 20°C on device 1006115-36 after it had received a fluence of 1.63×10^{16} p/cm^2 with temperature profile shown in the upper curve.

Figure 4.4 demonstrates the stability of the current at a typical bias point and illustrates the size of the standard deviation on any measured current. This particular measurement involved application of 500 V over 15 hours at 20° C to diamond 1006115-36 after it had received 1.63×10^{16} p/cm^2. The line fitted to the graph for all data after 30 minutes intercepts current 90 ± 17 fA with a slope of $(-5.74 \times 10^{-17} \pm 1.61 \times 10^{-17})$ A/hr, i.e., consistent with zero. For the interval from 1 hr to 4 hr over which a measurement is taken, the slope of the data is $(-2.29 \times 10^{-16} \pm 1.65 \times 10^{-16})$ A/hr. Therefore, for each voltage, the leakage current is recorded after 30 minutes application of the bias voltage to ensure stable current.

Leakage current versus bias voltage

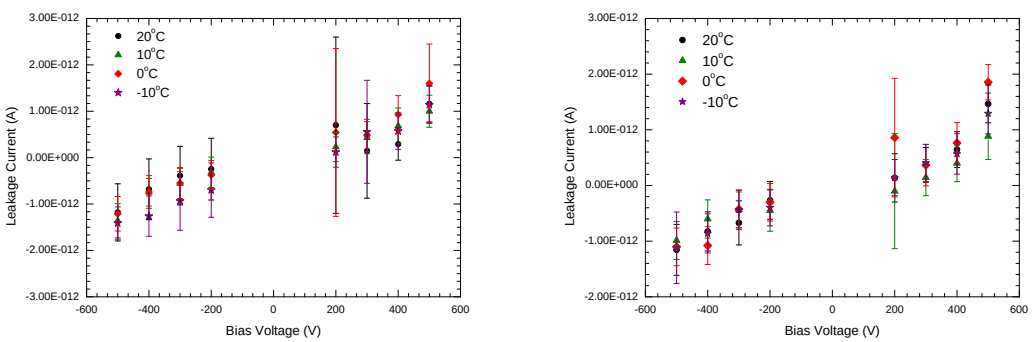

(a) (b)

Figure 4.5: Current versus voltage of 1006115-36 measured with its small side upward (a) and with its large side upward (b) before irradiation.

The leakage current is measured with bias voltage ramped over the range from -500 V to +500 V, for magnitudes greater than 100 V to avoid artifacts arising from the discontinuity at currents comparable to the intrinsic accuracy of the Keithley devices, which is 100 fA. An average of the leakage current, after reaching the stable stage, is taken to be the mean value. The standard deviation is assigned to be the

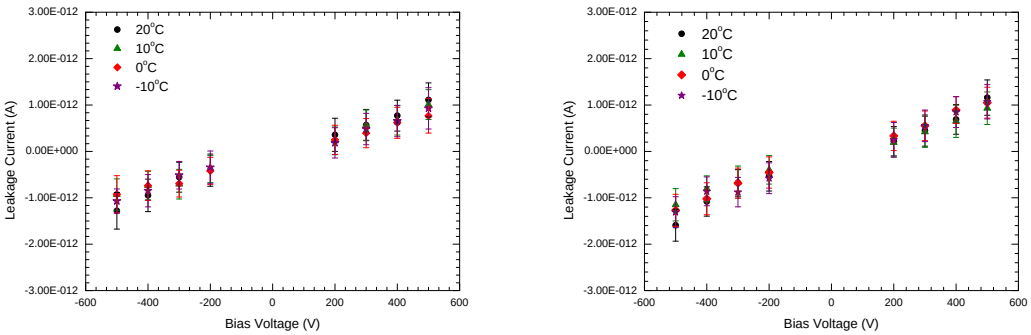

(a) (b)

Figure 4.6: Current versus voltage of 1006115-36 measured with its small side upward (a) and with its large side upward (b) after irradiation to 3.85×10^{15} p/cm^2.

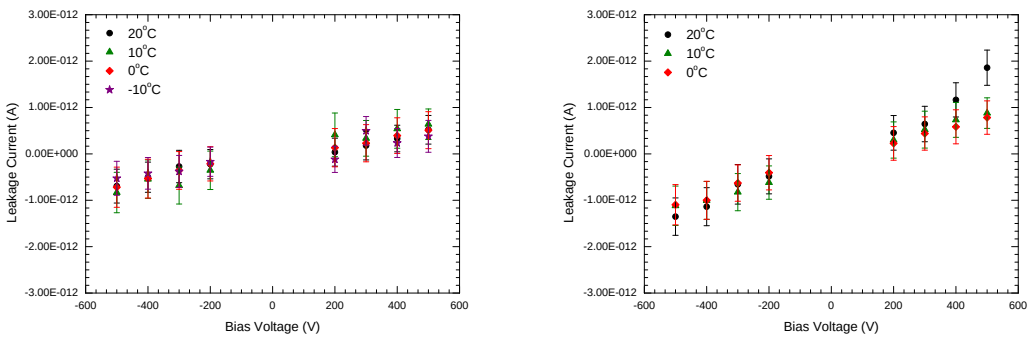

(a) (b)

Figure 4.7: Current versus voltage of 1006115-36 measured with its small side upward after irradiation to 1.11×10^{16} p/cm^2 (a) and 1.36×10^{16} p/cm^2 (b).

statistical uncertainty for each particular voltage and temperature point.

Confirmation measurements are done for bias voltage ramped both ways, and for the sensor placed with large side or small side (4.1(b)) up. Figures 4.5 and 4.6 show the leakage current in diamond 1006115-36 for positive and negative bias voltages up to 500 V measured with both small side and big side facing upward. No significant

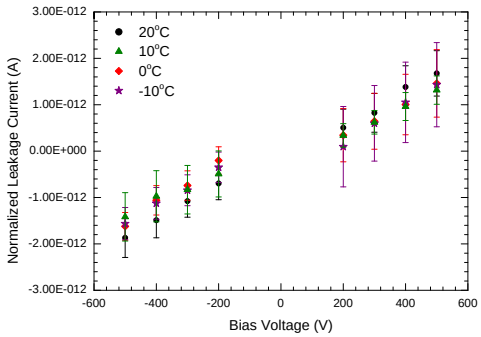

Figure 4.8: Current versus voltage of 1006115-36 measured with its small side upward after irradiation to 1.63×10^{16} p/cm^2.

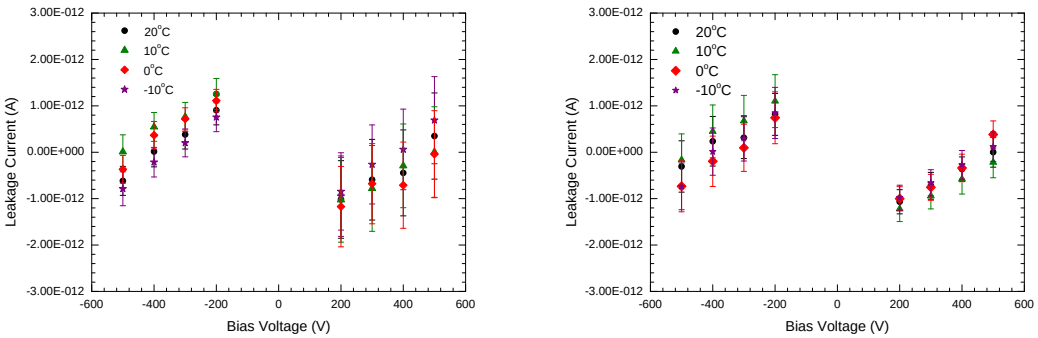

(a) (b)

Figure 4.9: Current versus voltage of 1006115-46 measured with its small side upward after irradiation to 2.76×10^{15} p/cm^2 (a), and 7.5×10^{15} p/cm^2 (b).

difference between those leakage current versus bias voltage (IV) curves can be seen in either absolute value or shape. Therefore after further irradiations the leakage current is measured only with the small side upward.

Leakage current versus temperature

To reach the HL-LHC condition, sensor 1006115-36 was irradiated four times with accumulated fluences of 3.85×10^{15} p/cm^2, 1.11×10^{16} p/cm^2, 1.36×10^{16} p/cm^2 and 1.63×10^{16} p/cm^2. For a cross check, sensor 1006115-46 was irradiated twice with accumulated fluences of 2.76×10^{15} p/cm^2 and 7.5×10^{15} p/cm^2. For each of those fluence points, the IV is measured as shown in Figures 4.5 (a), 4.6 (a), 4.8, and 4.9. (An instrument failure caused the data taken for 1001615-36 at -10°C after the 1.36×10^{16} p/cm^2 exposure and the unirradiated data for 1001615-46 to be lost.)

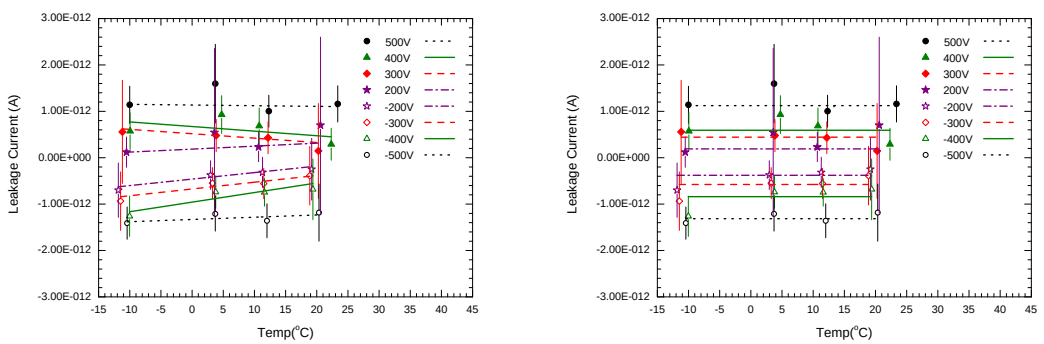

(a) (b)

Figure 4.10: Current versus temperature fitted using a linear function with floating slope (a) and fixed slope (b) prior to irradiation.

	500V	400V	300V	200V	-200V	-300V	-400V	-500V
floating slope	0.43	1.12	0.04	0.08	0.05	0.10	0.25	0.15
fixed slope	0.44	1.50	0.11	0.17	0.37	0.42	1.18	0.21

Table 4.4: The χ^2 of the linear fits applied to the current versus temperature curve for each bias voltage point before irradiation.

As is shown in those plots, the IV curve became more linear with irradiation, while the change in the absolute value remained within the statistical uncertainty at

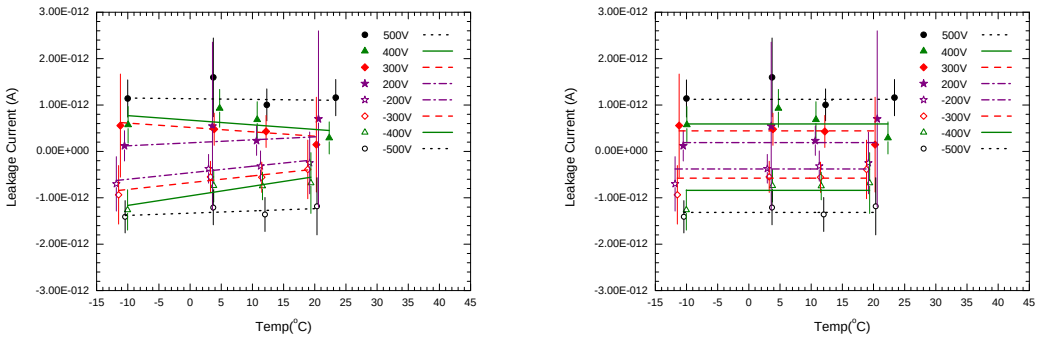

(a) (b)

Figure 4.11: Current versus temperature fitted using a linear function with floating slope (a) and fixed slope (b) at 3.85×10^{15} p/cm^2.

	500V	400V	300V	200V	-200V	-300V	-400V	-500V
floating slope	0.28	0.06	0.13	0.04	0.02	0.28	0.26	0.54
fixed slope	0.47	0.11	0.20	0.14	0.03	0.31	0.28	0.57

Table 4.5: The χ^2 of the linear fits applied to the current versus temperature curve for each bias voltage point after the application of 3.85×10^{15} p/cm^2.

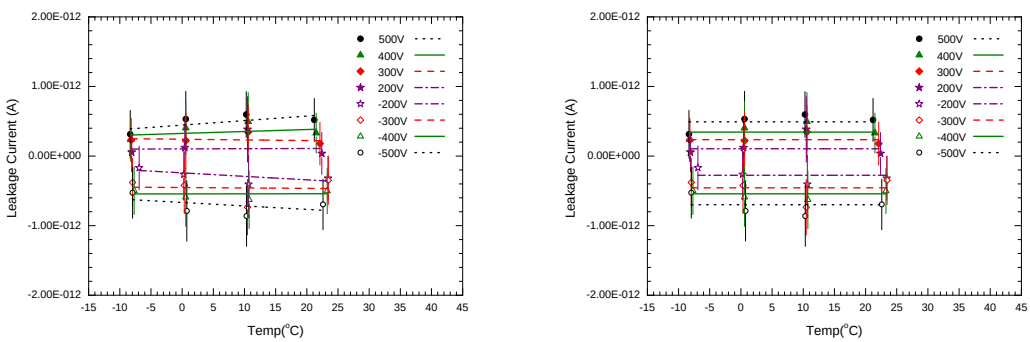

(a) (b)

Figure 4.12: Current versus temperature fitted using a linear function with floating slope (a) and fixed slope (b) at 1.11×10^{16} p/cm^2.

	500V	400V	300V	200V	-200V	-300V	-400V	-500V
floating slope	0.20	0.23	0.11	0.43	0.10	0.64	0.09	0.31
fixed slope	0.39	0.27	0.12	0.43	0.23	0.64	0.09	0.40

Table 4.6: The χ^2 of the linear fits applied to the current versus temperature curve for each bias voltage point after the application of 1.11×10^{16} p/cm^2.

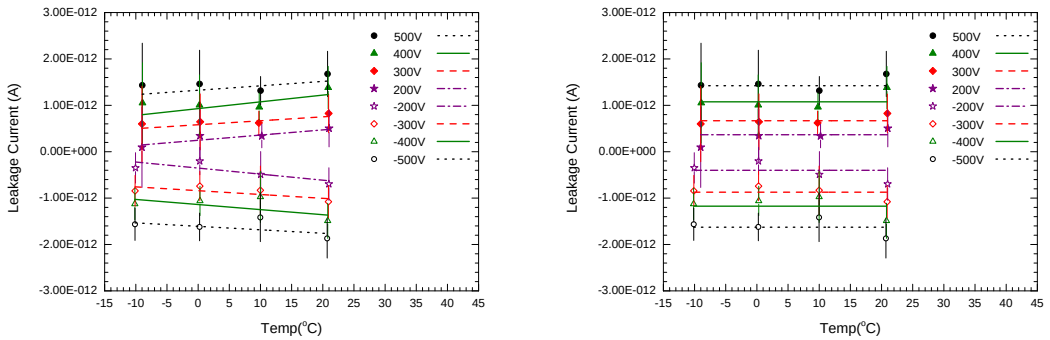

(a) (b)

Figure 4.13: Current versus temperature fitted using a linear function with floating slope (a) and fixed slope (b) at 1.63×10^{16} p/cm^2.

	500V	400V	300V	200V	-200V	-300V	-400V	-500V
floating slope	0.29	0.33	0.07	0.04	0.46	0.25	0.50	0.33
fixed slope	0.39	0.61	0.18	0.22	1.23	0.54	0.98	0.53

Table 4.7: The χ^2 of the linear fits applied to the current versus temperature curve for each bias voltage point after the application of 1.63×10^{16} p/cm^2.

approximately 4 $\times 10^{-13}$ A for 1001615-36. It is approximately 3 (9) $\times 10^{-13}$ A for negative (positive) voltages applied to 1001615-46, depending upon the setups for all the points.

The leakage current dependence upon the temperature (IT) is shown in Figures 4.10, 4.11, 4.12, and 4.13 using sample 1001615-36. A linear fit has been applied to each voltage point with the χ^2 recorded (Tables 4.4, 4.5, 4.6, and 4.7 respectively).

The fits with floating slope and slope fixed to 0 are compared. The compatible χ^2 values show that the fit quality with slope fixed to 0 is not worse. No significant dependence upon the temperature is observed. The measurements at 1.36×10^{16} p/cm^2 are not included as they are missing one of the temperature points.

4.4.6 Resistivity

Resistivity is computed as

$$\rho = AR/d \tag{4.1}$$

where R is the resistance, given by the inverse of the slope of a linear fit to the IV curve; A is the area of the sensor; and d is the thickness of the sensor.

Data taken at positive and negative voltages are fitted separately for each voltage due to the difference of the zero level and the shifts in the leakage current introduced by the setups. The data in each IV graph are fitted to straight lines for the two separate ranges [-500 V, -200 V] and [200 V, 500 V]. Their average slope gives R.

For each temperature and fluence combination, those two slopes are extracted and averaged, and this average R is converted to a resistivity using Equation 4.1. Figure 4.14 shows the set of fitted lines resulting from this procedure applied to sensor 1006115-36 after exposure to 3.58×10^{15} p/cm^2.

4.4.7 Uncertainties

The statistical uncertainty on any measured current using Configuration 1 is approximately 4×10^{13} A, derived from its standard deviation. For Configuration 2, due to the lower precision of the Keithley 617, the statistical uncertainty on the measured current is approximately $(3 - 9) \times 10^{13}$ A.

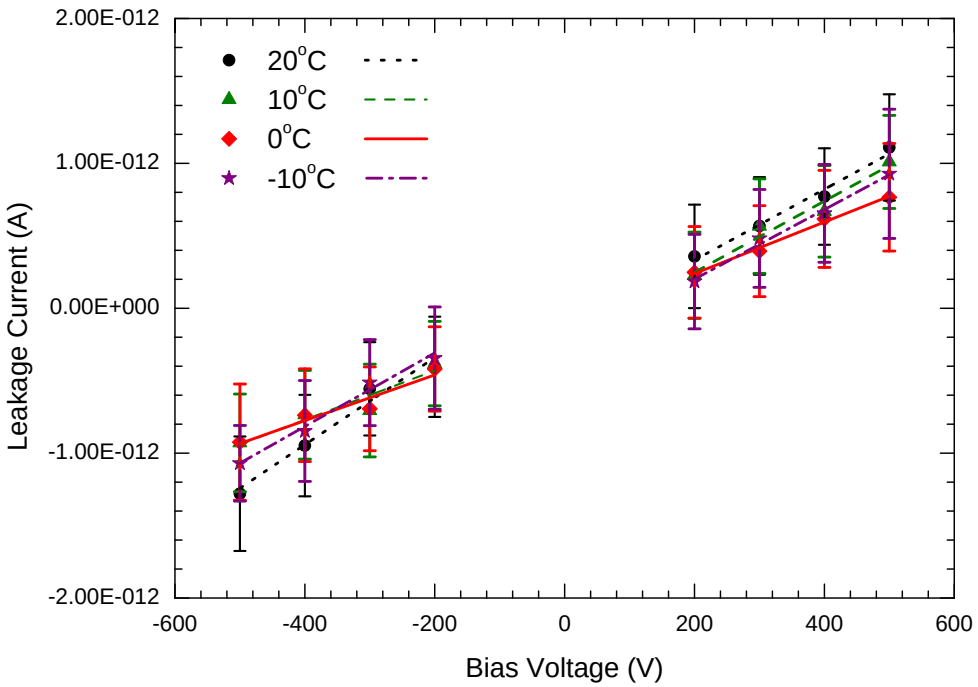

Figure 4.14: Current versus voltage of the sensor with separate linear function fits to both the positive and negative voltages after it has received 3.58×10^{15}p/cm^2.

The systematic uncertainties on the bias voltage and leakage current derive from the manufacturer's accuracy specifications for the Keithley 237 and are $\pm$(0.04%+240 mV) on the applied voltage and $\pm$(0.3% + 100 fA) on the measured current respectively. For the Keithley 613 it is $\pm$(0.16% + 66 fA) on the measured current. The uncertainties on the measured dimensions are given in the caption of Table 4.2.

The systematic uncertainty on the measured value of each temperature and fluence condition is obtained by shifting the measured voltages, leakage current, and dimensions by ± 1 standard deviation, then repeating the fitting procedure as shown in Figure 4.15. These three contributions yield a systematic uncertainty of magnitude less than $6 \times 10^{14}\ \Omega - \text{cm}$ (30%). The difference between the resistivity measured by

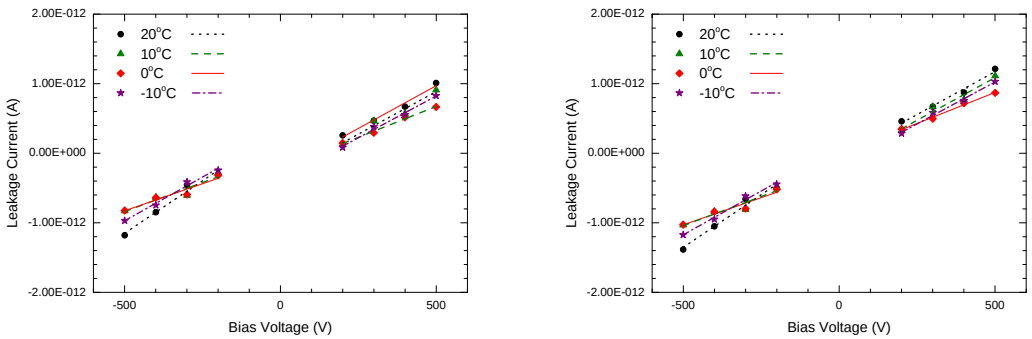

(a) (b)

Figure 4.15: The IV data refitted with several options as part of the systematic uncertainty calculation, following receipt of fluence 3.85×10^{15} p/cm^2. Figure (a) is the one with data points shifted by -1 σ, and Figure (b) is the one with data points shifted by +1 σ.

the two setups is about 25%. The total uncertainty is 40%.

Relative humidity is less than 5% for all measurements below 20°C and less than 35% for room temperature measurements. The fluence precision is known to be within 10-30%.

4.4.8 Results

Figure 4.16 summarizes the resistivity versus temperature for all fluences and both diamonds. A linear fit to the data in Figure 4.16 returns an intercept of $(8.37 \pm 0.55) \times 10^{15}$ Ω-cm and slope $(-0.63 \pm 4.13) \times 10^{13}$ Ω-cm, with $\chi^2/N.d.o.f. = 0.62$. Figure 4.17 summarizes the resistivity versus fluence for all temperatures and both diamonds. A linear fit to the data in Figure 4.17 returns an intercept of $(8.01 \pm 0.81) \times 10^{15}$ Ω-cm and slope $(0.49 \pm 8.4) \times 10^{-2}$ Ω-cm/(p/cm^2) with similar $\chi^2/N.d.o.f.$

Thus diamonds 1006115-36 and 1006115-46 have resistivity approximately 10^{16} Ω-

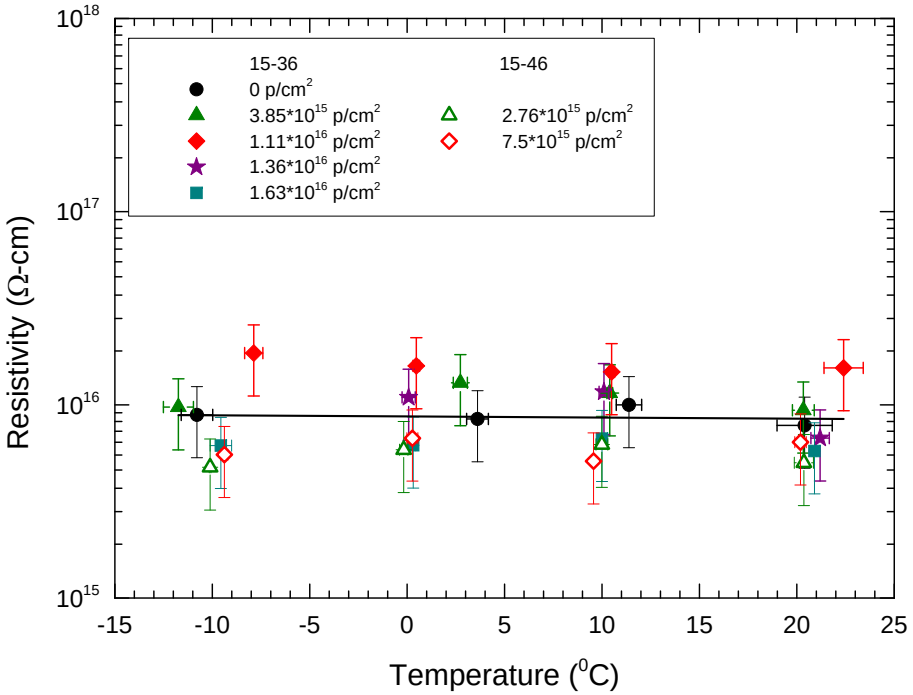

Figure 4.16: Resistivity of the diamond sensors as a function of temperature, for fluences ranging from 0 to 1.63×10^{16} 800 MeV protons/cm^2. A free linear fit to the data is shown, with intercept $(8.37 \pm 0.55) \times 10^{15}$ Ω-cm, slope $(-0.63 \pm 4.13) \times 10^{13}$ Ω-cm/°C, and $\chi^2/N.d.o.f. = 0.62$. The relative humidity is less than 5% for all measurements below 20°C and less than 35% for room temperature measurements, and is not included in the error bar.

cm, independent of fluence up to 1.63×10^{16} 800 MeV p/cm^2 and independent of temperature over the range [−12°C, +23°C], with total uncertainties of 40% for both samples.

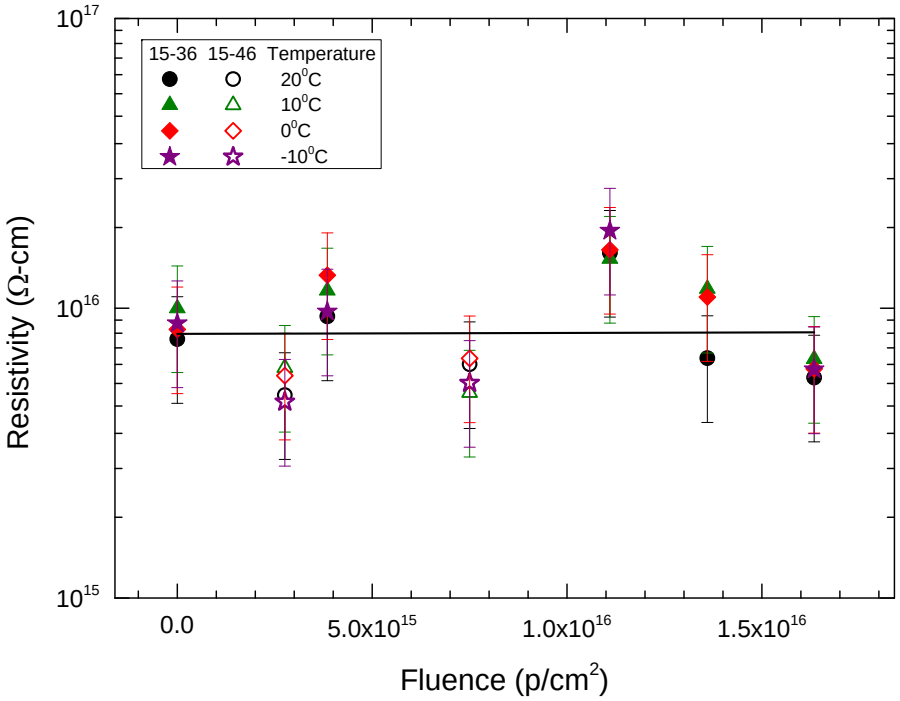

Figure 4.17: Resistivity of the diamond sensors as a function of fluence, for temperatures ranging from $-10°$C to $+20°$C. A free linear fit to the data is shown, with intercept $(8.01 \pm 0.81) \times 10^{15}$ Ω-cm, slope $(0.49 \pm 8.54) \times 10^{-2}$ Ω-cm/(p/cm^2), and $\chi^2/N.d.o.f. = 0.62$. The fluences are known to within 10-30%, and this is not included in the error bar.

4.5 ATLAS pixel current monitoring project

In addition to the development of new technologies for the pixel detector, it is important to measure the effect of the radiation damage to the present sensors. This affects their depletion voltage and leakage current and can be monitored during the LHC operation. The hardware system which provides the basis for this is the High Voltage Patch Panel 4 (HVPP4) and Current Monitoring Board (CMB) system [98].

4.5.1 Introduction

The HVPP4 system is designed to connect the high voltage power supply (Iseg [99]) to the pixel sensors and is able to control the bias voltage of each individual module. Thus the current measurement system based on the HVPP4 can be used for monitoring the leakage current of the pixel sensors in real time.

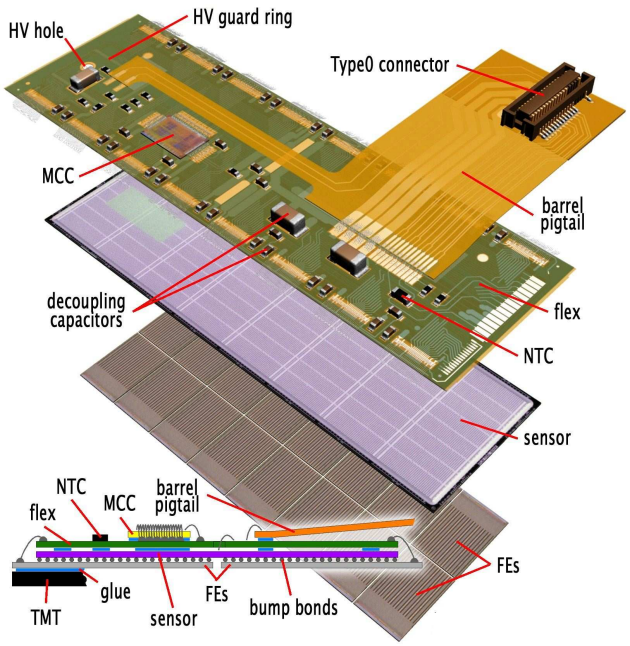

Figure 4.18: Schematic view of a barrel pixel module (top) illustrating the major pixel hybrid and sensor elements, including the MCC (module-control chip), the front-end (FE) chips, the NTC thermistors, the high-voltage (HV) elements, and the Type0 signal connector. Also shown (middle) is a plan view showing the bump-bonding of the silicon pixel sensors to the polyimide electronics substrate. The photograph at the bottom shows a barrel pixel module.

Each pixel sensor at ATLAS consists of a 252.5 ± 2.8 μm thick n-bulk. The bulk contains n^+ implants on the read-out side and the p-n junction on the back side. For each sensor tile, the 47232 pixel implants are arranged in 144 columns and 328 rows. In 128 columns (41984 or 88.9%) pixels have implant sizes of 382.5×30 μm^2 with a pitch corresponding to $400 \times 50\,\mu m^2$, and in 16 columns (5248 or 11.1%) pixels

have implant sizes of 582.5×30 μm^2 corresponding to a pitch of 600×50 μm^2. In each column, eight pairs of pixels are ganged to a common read-out. This allows the connection of the sensor tile to 16 electronic front-end chips to be combined into a single module. The geometry of a single pixel module is shown in Figure 4.18. Each module has an active surface area of 6.08×1.64 cm^2.

Layer Number	Mean Radius [mm]	Number of Staves	Number of Modules	Active Area [m^2]
0	50.5	22	286	0.28
1	88.5	38	494	0.49
2	122.5	52	676	0.67
Total		112	1456	1.45

Table 4.8: Basic parameters of the barrel region of the ATLAS pixel detector system.

As mentioned in Section 2.2.1, the ATLAS Pixel Detector comprises three Layers (Layer-0, Layer-1 and Layer-2) in the barrel region, and three disks in both forward and backward endcap regions, with a total number of 1744 modules mounted. The parameters of the three Layers are summarized in Table 4.8. The modules are mounted on evaporative cooling supports. The average operational temperature is about -13 °C. During the scheduled maintenance warm-up periods it is about 20 °C.

In each stave there are 13 modules instrumented, which in total gives an active length of about 801 mm. During the first period of data-taking, when the radiation damage of the sensors is small, the sensors in one stave are fed by two Iseg power supply channels (with maximum current I $<$ 4000 μA). One channel is connected to one half-stave, which has six or seven modules. Beyond some level of radiation damage after the type inversion of the silicon sensors, the current will reach the Iseg limit. A number of power supply channels will be added until two pixel modules can be fed by one Iseg power supply. Right now, the radiation damage level is still low

enough for two Iseg supplies per stave to supply 6 or 7 modules.

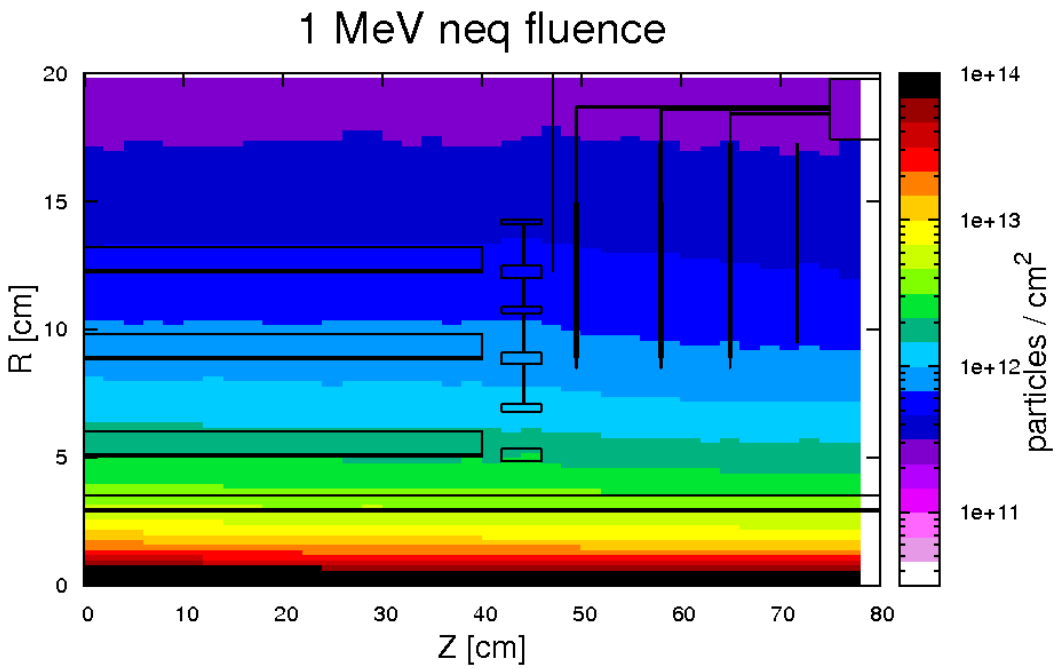

Figure 4.19: The simulated 2 MeV neutron equivalent fluence for an integrated luminosity of 1 fb^{-1} in the R-z plane at $\sqrt{s} = 7$ TeV. The geometry of the ID is assumed to be symmetric. [102]

At ATLAS, the integrated fluence is expected to be proportional to the integrated luminosity, $\int \mathscr{L} dt$. In the Pixel detector volume, the simulated fluence [102] for an integrated luminosity of 1 fb^{-1} is shown in Figure 4.19 at $\sqrt{s} = 7$ TeV and in Figure 4.20 at $\sqrt{s} = 8$ TeV. The highest fluence appears at the interaction point, and decreases to the end of the pixel barrel region and the disks.

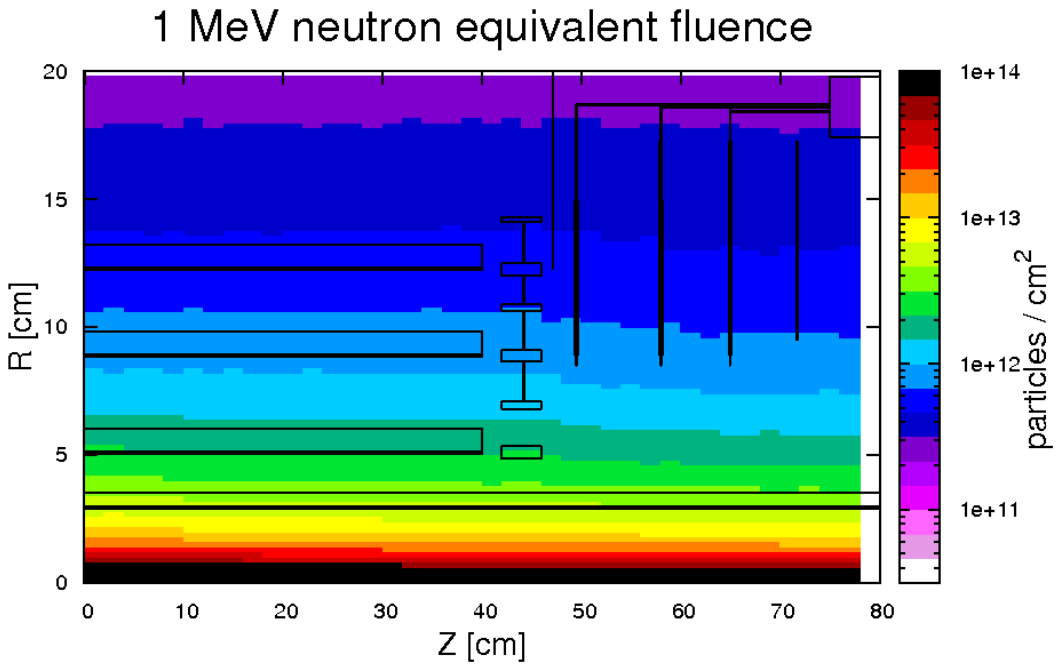

Figure 4.20: The simulated 1 MeV neutron equivalent fluence for an integrated luminosity of 1 fb^{-1} in the R-z plane at $\sqrt{s} = 8$ TeV. The geometry of the ID is assumed to be symmetric. [102]

4.5.2 Radiation damage

Because the barrel layers and disks are very close to the *pp* interaction point, the dominant source of the radiation damage is charged pions. Albedo neutrons originating in the outer ATLAS detectors also contribute. These mainly introduce displacement defects in the bulk of the pixel sensors, caused by non-ionizing energy losses (NIEL). These defects result in three effects:

- Increase of the leakage current. This is caused by electron-hole pair generation in defect centers. It will degrade the signal-to-noise ratio and require more

cooling.

- Change of the depletion voltage. When the n-type bulk inverts to p-type, the depletion voltage increases. It will require higher bias voltage to maintain the sensor fully depleted. This effect is expected to occur at $\Phi \geq 1 \times 10^{14}$ n_{eq}/cm^2.

- Decrease of the charge collection efficiency due to charged carrier trapping. The number of localized trapping centers is increased by the displacement damage. When the time to re-emit the trapped charge carrier is longer than the amplifier shaping time, the charge collection efficiency degrades. This causes a loss of induced charge resulting in a reduction of signal. This effect is dominant at $\Phi > 1 \times 10^{15} n_{eq}/cm^2$.

The radiation hardness requirement on the pixel sensors is therefore greater than $10^{15} n_{eq}/cm^2$.

4.5.3 Leakage current

The leakage current of a silicon sensor strongly depends upon both the temperature of the sensor and the particle fluence. The fluence $\Phi_{n_{eq}}$ is defined as the number of particles which cause damage equivalent to 1 MeV neutrons, traversing 1 cm^2 of a sensor's surface. The ATLAS pixel detector integrated fluence $\Phi_{n_{eq}}$ is proportional to the integrated luminosity $\int \mathscr{L} dt$.

Temperature

For the Pixel detector, the average barrel temperature used in model predictions and the average temperature for each layer during the stable beam are shown in Figures 4.21(a), (b), and (c). The temperature is stable with an average of about -13

°C and fluctuations of ±3 °C. The temperature variation in one individual module is much smaller (Figure 4.21(d)), less than 0.5 °C.

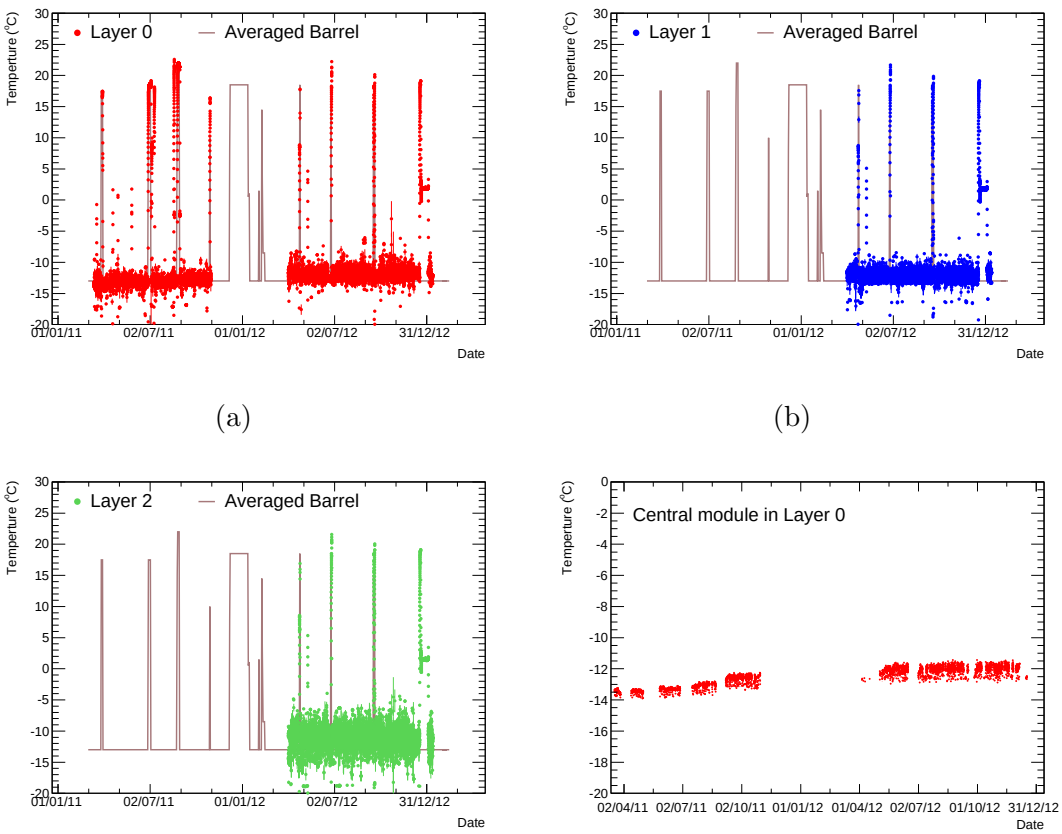

Figure 4.21: The average barrel temperature ((a) Layer-0 from 2011 to 2012, (b) Layer-1 in 2012 and (c) Layer-2 in 2012) with the temperature used for model predication during the whole LHC operation (solid line). Figure (d) is an example for one central module in Layer-0.

To compare the leakage current data to a model prediction, the leakage current is normalized to a reference temperature (T_{ref}), using

$$I(T_{ref}) = I(T)(T_{ref}/T)^2 \cdot \exp\left(-\frac{E_g}{2k_B}(1/T_{ref} - 1/T)\right), \tag{4.2}$$

where $T_{ref} = 0°\text{C}$ and the silicon band gap $E_g = 1.21$ [100].

Fluence dependence

The increase of the leakage current due to radiation damage has been observed to be proportional to fluence [101], giving

$$\Delta I = \alpha \Phi_{\text{eq}} V. \tag{4.3}$$

Here ΔI is the difference in leakage current at fluence Φ_{eq} relative to the value before

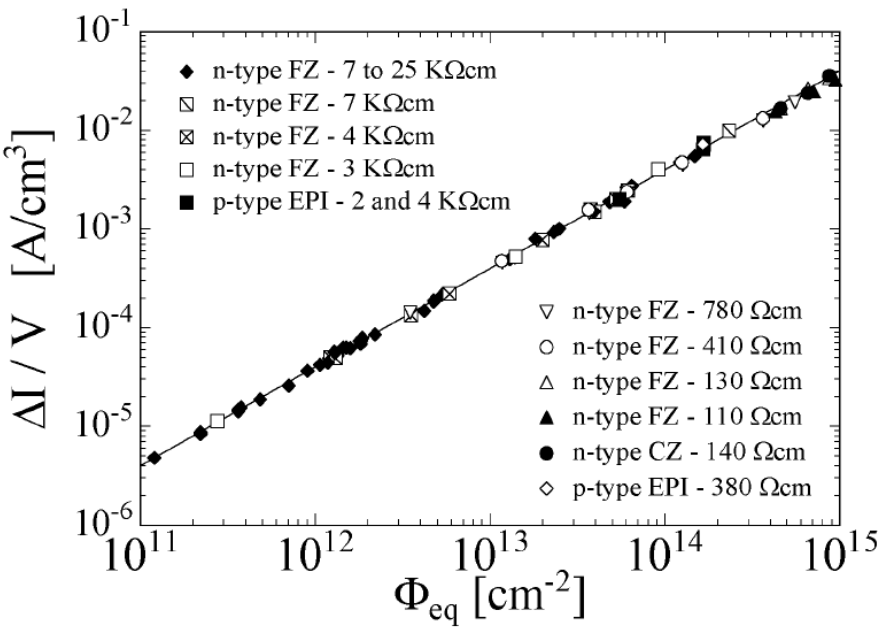

Figure 4.22: Fluence dependence of leakage current for silicon produced by various process technologies from different silicon materials. The current was measured after a heat treatment for 80 min at 60°C, with the result that $\alpha(20^\circ\text{ C}; 80\text{min@}60^\circ\text{C}) = (3.99 \pm 0.03) \times 10^{-17}$ A/cm. [101]

irradiation, V is the physical volume, and α is the current-related damage rate. The α has been measured at 20°C (Figure 4.22) and found to be:

$$\alpha(20^\circ\text{C}; 80\text{ min@}60^\circ\text{C}) = (3.99 \pm 0.03) \times 10^{17}\text{A/cm} \tag{4.4}$$

after annealing for 80 minutes at 60°C.

Annealing

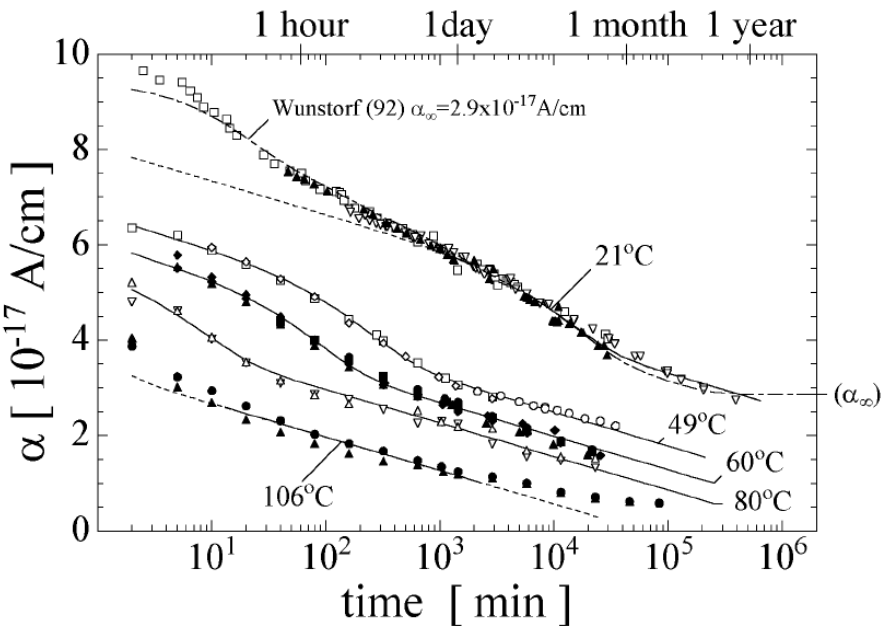

Figure 4.23: The current-related damage rate α as a function of accumulated annealing time at different temperatures. For each temperature at least one type inverted and one non-type inverted sample have been used. [101]

Defects in the crystal bulk can anneal through dissociation and diffusion, and thus the defects migrate and form new complex defects. These effects strongly depend on the temperature. The leakage current benefits from annealing as is shown in Figure 4.23. Even after type inversion, the leakage current diminishes during annealing.

Lifetime estimate/ Planning

By comparing the temperature corrected leakage current with the integrated luminosity, the amount of current the pixel modules will draw after a certain integrated luminosity can be predicted per module for the ATLAS Pixel detector. This permits

the estimation of the time when the Iseg power supplies will saturate and ATLAS will need to add more Iseg channels.

4.5.4 Leakage current monitoring system

Figure 4.24: A Current Measurement Board. [103]

At the Iseg level, the current is monitored with precision of about 80 nA per Iseg channel for 6 or 7 modules. There is a need to measure individual sensor currents in order to monitor and understand the damage resulting from increasing radiation dose. To make a more precise measurement of the leakage current for each individual pixel module, a dedicated Current Measurement Board (CMB, Figure 4.24) system has been developed. It is complementary to the Iseg monitoring system and has the advantage of greater precision on low currents giving the ability to track the increase in leakage current in the early stages of sensor damage.

The CMB circuit is a current to frequency converter which is coupled to a frequency to voltage convertor as shown in Figure 4.25 [103]. Each CMB holds 4 current

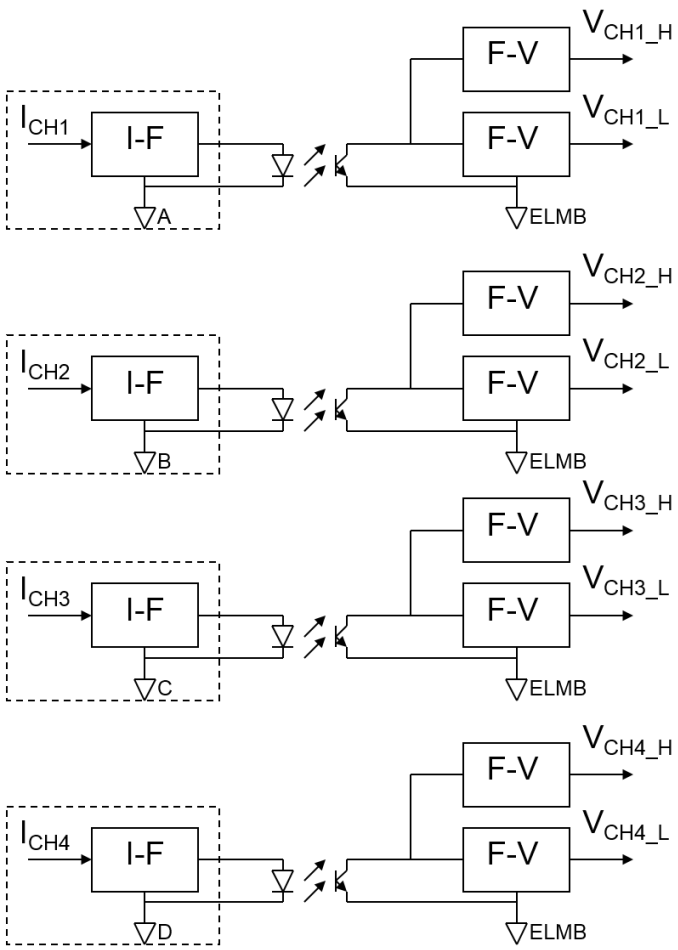

Figure 4.25: The circuit of the Current Measurement Board.

measurement circuits and provides the current measurement for 4 modules. Two similar circuits with different gains are provided for each module measurement, the low range (high gain) channel for $\sim [10^{-8} - 10^{-5}]$ A and a high range (low gain) channel for $\sim [10^{-6} - 10^{-3}]$ A. As is shown in Figure 4.26, the low range channel covers the transition region of the high range channel well. The measured range of the CMB is [0.01 μA - 2 mA] with a precision of better than 20% per module.

Before installation, each CMB is calibrated for its gain and pedestal [103]. Calibration runs are made with a test stand offline. For each individual channel, a linear

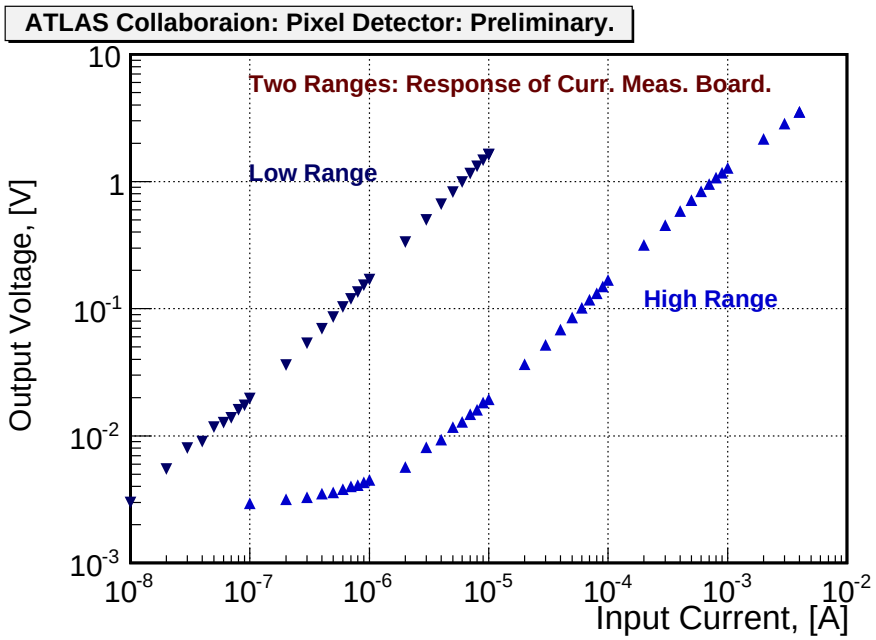

Figure 4.26: The response of a pre-prototype current measurement board to the calibrated current supplied by a Keithley power source. [103]

function is fitted to the stored intercept (pedestal) and slope (Figure 4.27). The obtained parameters were uploaded to the ATLAS Detector Control System (DCS) database. For precision, the pedestals are recalibrated in situ with the high voltage off.

The installation of the CMBs in the ATLAS pit took place between the beginning of 2011 and mid-2012. Every CMB measures four modules in the same half stave. The measured modules were chosen to be almost uniformly distributed in η and ϕ in all three layers. In total, there are 21 CMBs installed in Layer-0 (84 modules instrumented), 16 CMBs installed in Layer-1 (64 modules instrumented), and 16 CMBs installed in Layer-2 (64 modules instrumented).

The currents measured by the CMB are digitized by the CERN-developed digital board ELMB [104] and transmitted via data Controller Area Network (CAN) bus to

the DCS. The output CMB voltage range is determined by one of 5 available ELMB input voltage ranges: [0-25] mV, [0-100] mV, [0-1] V, [0-2.5] V, and [0-5] V. The 16-bit ADC of the ELMB provides a resolution of (ELMB range)/2^{16}. In 2011 the ELMB range [0-1] V was chosen. In 2012 this range has been changed to the [0-5] V for Layer-0 , because the low range channels were saturated by the end of May. This corresponds to leakage currents larger than 10^{-5} A. Layer-1 and Layer-2 continue to use the low range channels in 2012.

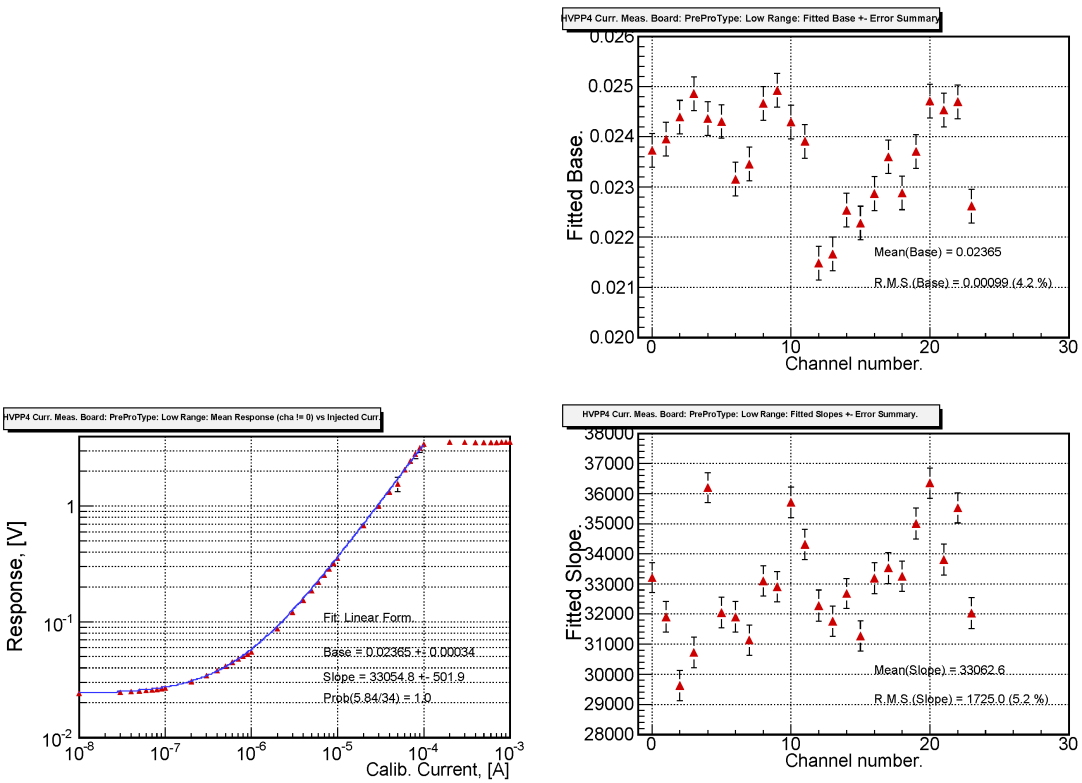

(a) (b)

Figure 4.27: (a) An example of the individual linear fit to the stored intercept (pedestal) and slope per channel (low range). (b) The pedestals (upper) and slopes (lower) of 16 low range channels in 4 CMBs. [103]

4.5.5 Result

The leakage current and temperature of each individual module that is monitored are stored in the ATLAS DCS database. They can be accessed offline. Because the current data are recorded once per half hour, the temperature used is the averaged value in this time period. The current is normalized to the reference temperature per module.

When Layer-0 was switched to the high range channel, a universal drop in the current was observed compared to that in the low range channel. Because the initial data-taking began in the low range, high range data in early 2012 were calibrated to low range values. In late 2012, those data were re-calibrated to the Iseg measurement by comparing them to the summed value

$$I_{sum} = (1 + 2(3) * 0.25) * (I_1 + I_2 + I_3 + I_4), \tag{4.5}$$

of each half stave. The 2(3) is used when the Iseg supplies 6(7) modules. This calibration is done by obtain the average coefficient for each of the 4 periods separated by the technical stops. All of the 4 channels in the same half-stave share the same coefficient.

The average leakage current of all channels in Layer-0, Layer-1, and Layer-2 versus date and integrated luminosity are shown in Figure 4.28. The data points are restricted to periods when the LHC stable beam flag and pixel detector HV were on. For Layer-1 and Layer-2, due to the installation plan, only 2012 data are available. The beam introduced ionization current correction is included. It is defined as:

$$I_{hit} = N_{bunches} \cdot \mu_{LHC} \cdot Occ \cdot C_{hit}, \tag{4.6}$$

where $N_{bunches}$ is the number of bunches, μ_{LHC} is the average bunch crossing frequency, Occ is the pixel hits occupancy, and C_{hit} is the charge per hit. This correction is less than 1%. The model used for the prediction is described in [105]. The

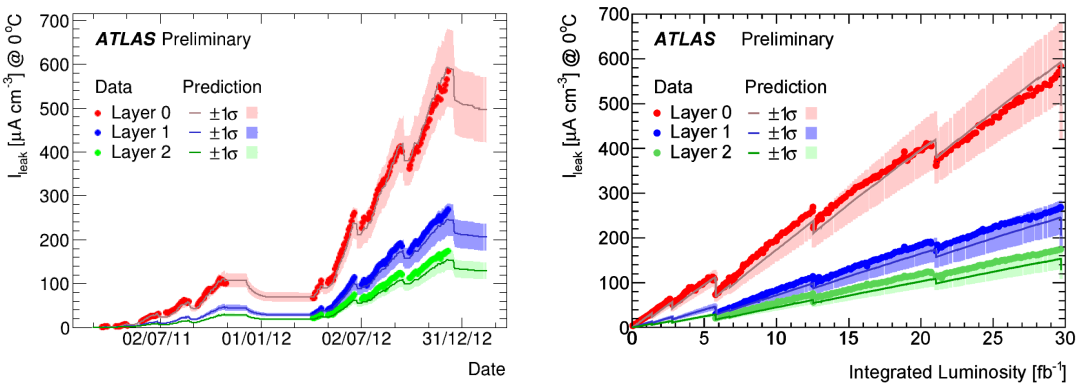

(a) (b)

Figure 4.28: (a) ATLAS Pixel module leakage current versus date and (b) ATLAS Pixel module leakage current versus integrated LHC luminosity. The currents are averaged over their layer for all modules equipped with Current Monitoring Boards within the layer. The current is continuously monitored by the ATLAS Detector Control System (DCS). A prediction based on the Hamburg Model is included. Discontinuities are due to annealing during cooling stops.

predicted current is included for each layer. Its uncertainty takes into account the temperature variation and uncertainty on α. The beneficial annealing periods can be clearly seen, and the data matches the prediction within the uncertainty.

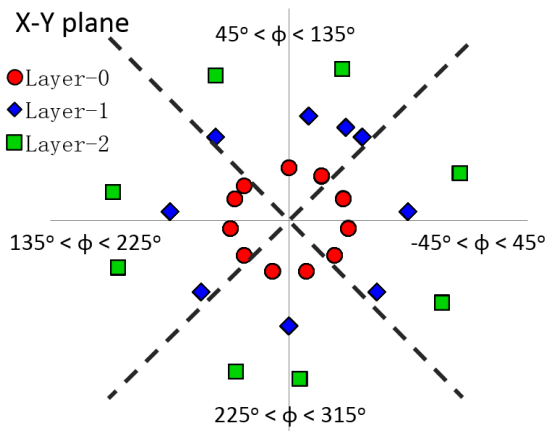

Figure 4.29: The distribution of the monitored modules in the x-y plane.

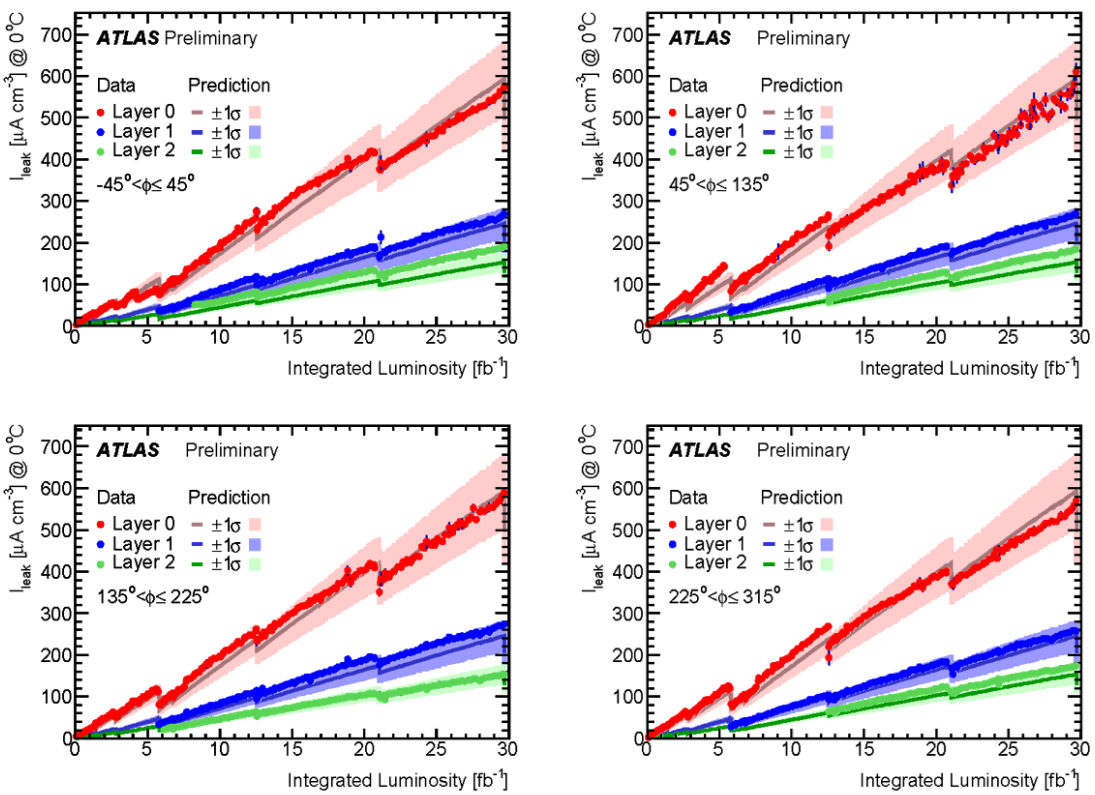

Figure 4.30: ATLAS Pixel module leakage current in each of 4 quadrants in azimuthal angle, versus integrated LHC luminosity. The currents are averaged over their layer for all modules equipped with Current Monitoring Boards within the layer. The current is continuously monitored by the ATLAS Detector Control System (DCS). A prediction based on the Hamburg Model is included. Discontinuities are due to annealing during cooling steps.

As mentioned in Section 4.5.4, the monitored modules were chosen to be uniformly distributed in η and ϕ. This allows the study of the leakage current angular dependence.

The module positions in the x-y plane are shown in Figure 4.29. The plane is divided into quadrants. The average leakage current in each quadrant is shown in Figure 4.30. The model prediction is included. The leakage current is found to be symmetric over x and y, with no dependence upon ϕ observed. It is consistent with

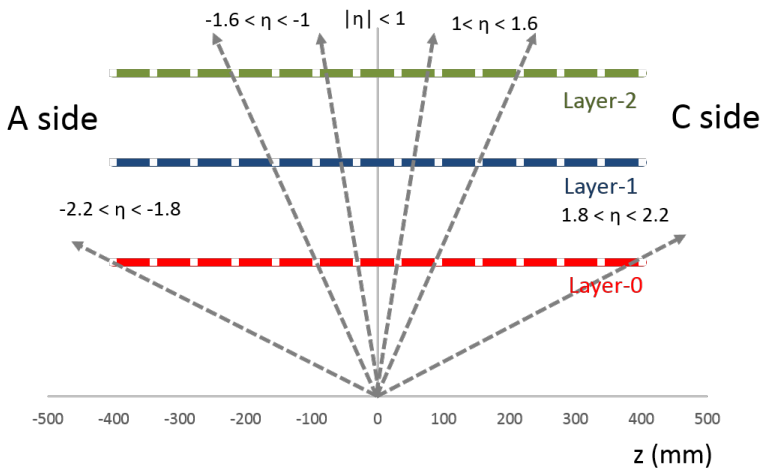

Figure 4.31: The distribution of the monitored modules in z.

the prediction to within 1σ.

The module positions along z are shown in Figure 4.31. The barrel has been divided into five pseudorapidity ranges: two symmetric ones on the A side and C side and one in the center. The η calculation is based on modules in each Layer. The exact ranges are approximately equal between Layers.

The average leakage current in each η range is shown in Figure 4.32. The leakage current decreases with η as is expected from the simulated fluence distribution reported in Section 4.5.1. Especially in Layer-0, the difference between the central range and the end is about 30%. In Layer-1 and Layer-2, the change is smaller because of their distances from the interaction point. There is also a difference ($<$ 20%) between the A side and C side. This maybe introduced by a difference between the two beams.

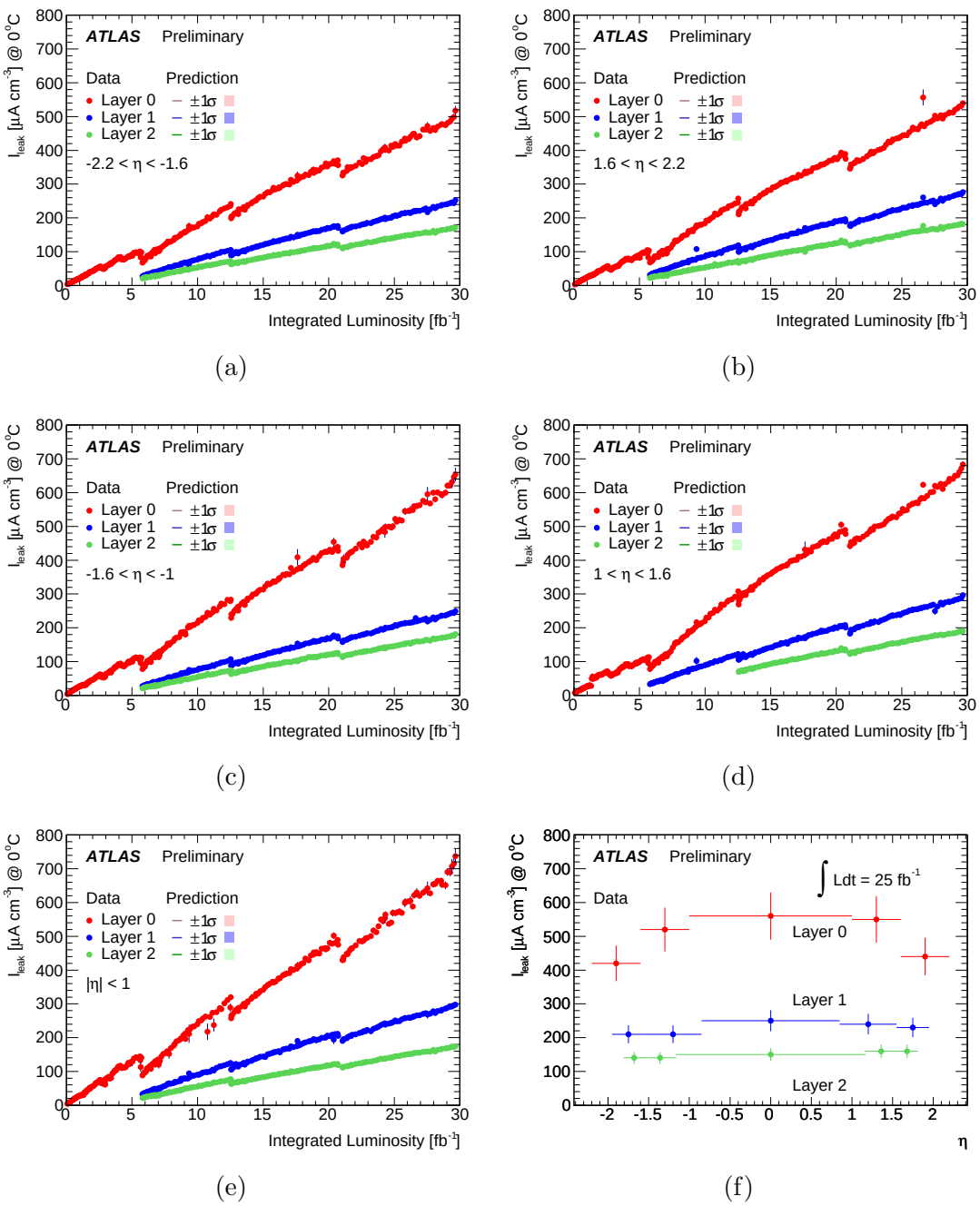

Figure 4.32: ATLAS Pixel module leakage current in each of 5 pseudorapidity sectors ((a) $1.6 < \eta < 2.2$, (b) $-2.2 < \eta < -1.6$, (c) $1 < \eta < 1.6$, (d) $-1.6 < \eta < 1$ and (e) $|\eta| < 1$), versus integrated LHC luminosity. Figure (f) is the leakage current versus module pseudorapidity, for integrated LHC luminosity equal to 25 fb^{-1}. The currents are averaged over their layer for all modules equipped with Current Monitoring Boards within the layer. The current is continuously monitored by the ATLAS Detector Control System (DCS). Discontinuities are due to annealing during cooling stops.

4.5.6 Uncertainties

The contributions to the uncertainty of the current measurement include

- the precision on current measurements: 6% from long cables, connections, and power supplies in the US15/USA15 racks and etc.; 10% from the CMB plus ELMB circuit. They give in total 12% uncertainty.
- the number of current measurements (one per half hour).
- the uncertainty on the averaged temperature, less than 0.3 °C. This corresponds to 3.4% on the normalized current.
- the uncertainty on the cross-scale factor in Layer 0 for the high range channels. This is less than 3.5%.

The uncertainty on the luminosity is 1.8% in 2011 and 2.8% in 2012 [59].

Chapter 5

Outlook

Taking advantage of the detailed B_c and B^+ selection and yield study described in Chapter 3, the relative production cross section measurement is naturally the next step to take. With the absolute B^+ production cross section measurement now available [62], the absolute cross section for the B_c can be inferred as well. These results can be further combined with the LHCb measurements to cover the whole LHC η region. Right now, ATLAS is in its first long shutdown, which will last until the end of 2014 for upgrades. The most important change for the Pixel detector is the addition of the Insertable B-Layer (IBL). This adds a fourth layer in the barrel region. This will enhance the tracking performance, especially for low p_{T} tracks. Currently, the resolution of the reconstructed B_c peak is large compared to the well-measured B^+. Improvement in the tracking performance will allow the possibility of more precise mass, lifetime, and cross section measurements. Also, more low p_{T} tracks can improve the statistics in the reconstruction of the excited B_c states. Starting from 2015, the LHC will run at a higher center of mass energy to collect a few tens of fb^{-1}. This will at least double the statistics on the signals in this report, for more detailed studies in the future. It may allow the production cross section measurement of the $B_c(2\mathrm{S})$ state.

Diamond sensors are still under development for pixel detector tracking. The charge collection distance is highly improved with time but diamond still requires much higher bias voltage than silicon to get to the necessary collection efficiency. New designs are under investigation. The aim is to be the candidate for the Phase II upgrade.

The study of the pixel current using the CMB system shows consistency with the Hamburg model. The model has now been well established for ATLAS conditions and is good for radiation damage and lifetime predictions. This analysis can be extended to the IBL which has current readout for each individual module by default.

Appendix A

$\pi^+\pi^-$ mass distribution

The invariant mass distribution of $\pi^+\pi^-$ pairs associated with the same primary vertex is shown in Figure A.1. All the selection cuts for the excited B_c state have been applied. No significant structure can be observed in both two years (e.g. $\rho(770) \to \pi^+\pi^-$).

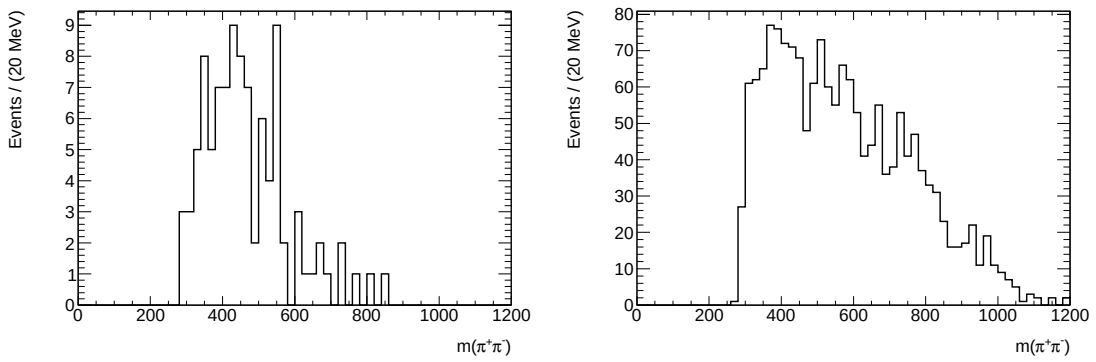

(a) (b)

Figure A.1: The invariant mass distribution of $\pi^+\pi^-$ pairs associated with the same primary vertex (all cuts applied) in (a) 2011 data and (b) 2012 data.

Appendix B

Confirmation of the peak in 2012 data using 2011 selections

Selection criteria for 2012 data were optimized using corresponding 8 TeV MC samples. Only the B_c ground state related selections were optimized. In this section we demonstrate the existence of the peak in 2012 data with 2011 selections applied.

In Figure B.1 (a) and (b), the B_c and $B_c(2S)$ masses and the Q value distributions are shown respectively with 2011 selections applied to the 2012 dataset, with only one exception: the $\Delta z0$ cut is always applied to 2012 data.

The excess in the $B_c(2S)$ signal region is clearly visible. The data in Figure B.1 are fitted with exactly the same fitting procedures as Figure 3.52. The background in Figure B.1 (b) is much higher than the background in Figure 3.52 (b), reflecting the fact that the 2011 selections are not optimal for 2012 data.

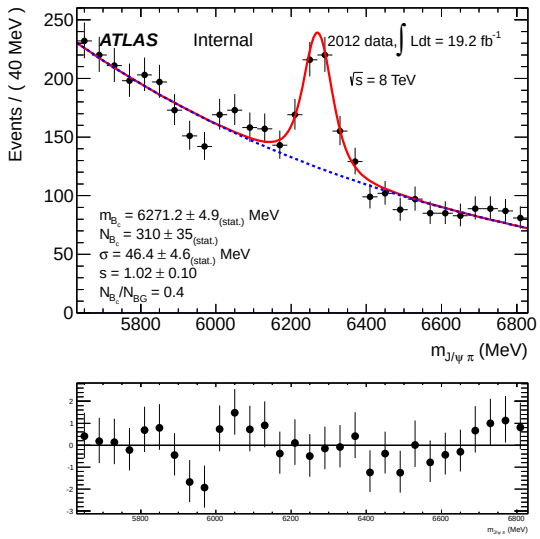

(a)

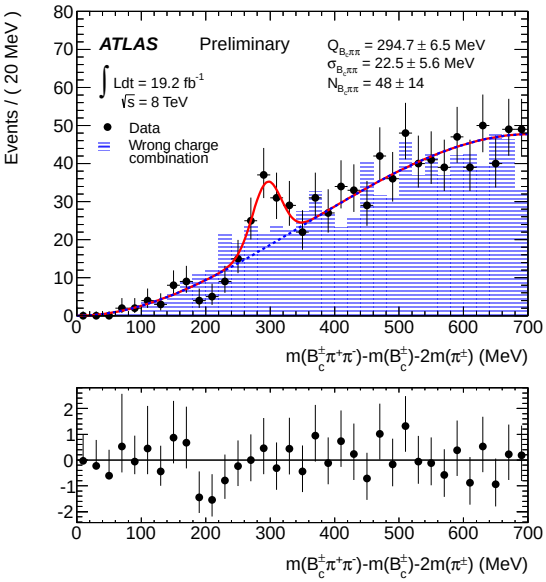

(b)

Figure B.1: (a) the $B_c \to J/\psi\pi$ invariant mass distribution and (b) the Q value distribution for the proper and wrong charge combinations for 2012 dataset with 2011 cuts applied.

Appendix C

Study of the impact of the momentum scale on the mass uncertainty

A study was done using 2011 data to estimate the systematic uncertainty on the mass due to the uncertainty on the hadronic p_{T} scale. The analysis was repeated two times with the p_{T} of every hadronic track in the analysis shifted up and down by 0.05%. The hadronic track momentum scale is extracted by comparing the $K_s^0(\pi^+\pi^-)$ invariant mass to the PDG world average. A 0.03% difference was observed on the $K_s^0(\pi^+\pi^-)$ invariant mass, corresponding to a 0.05% shift in the track momentum scale. Figures C.1–C.2 show the outcome of this study. The results are summarized in Table C.2.

The Q values are stable against small changes in the p_{T} scale, while the mean values of the $B^{\pm}$ mass are not. The systematic uncertainty on the mean value of the $B^{\pm}$ mass due to uncertainty on the hadronic p_{T} scale is about 0.8 MeV.

The same approach was applied to the B_c and $B_c(2S)$ states. In Figures C.3

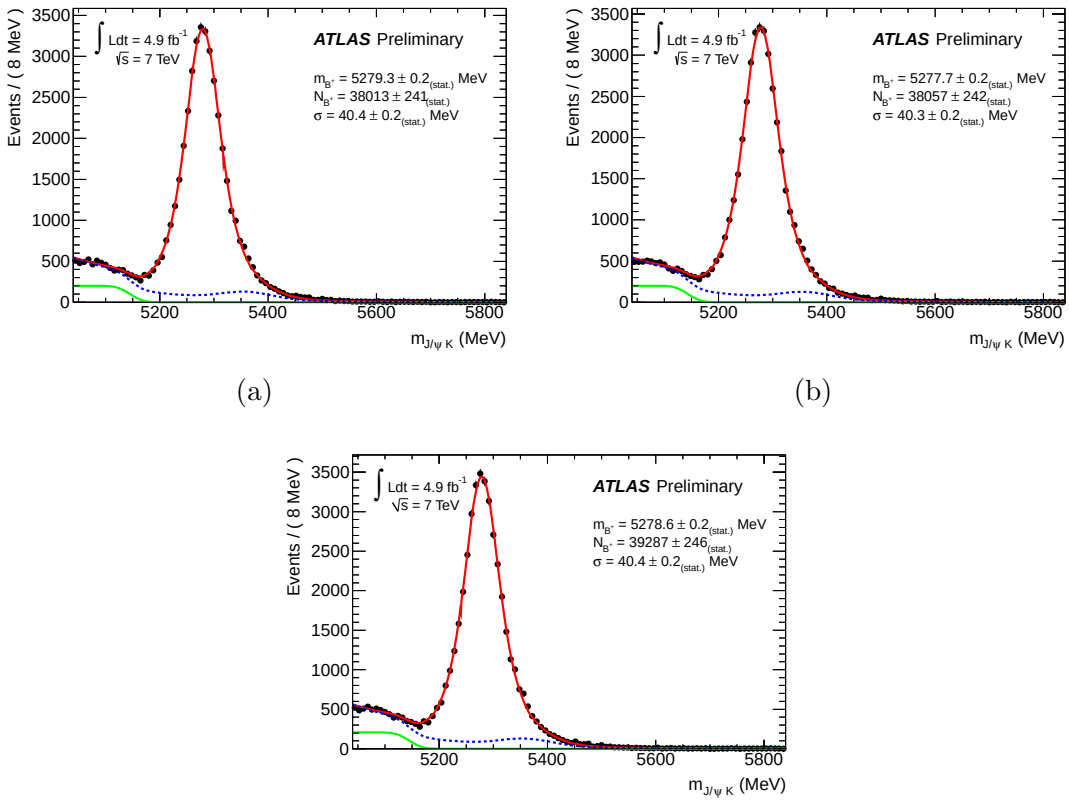

Figure C.1: The $B^{\pm} \to J/\psi K^{\pm}$ candidates, 2011 data. The p_{T} of all hadronic tracks is scaled up (a) and down (b) by 0.05%. The plot with the original p_{T} of all hadronic tracks is shown for comparison (c).

Hadron p_{T}	$m(B^{\pm})$, MeV	$Q(B_{s1})$, MeV	$Q(B^{*}_{s2})$, MeV
original p_{T}	$5278.6 \pm 0.2_{stat}$	$11.4 \pm 0.5_{stat}$	$66.4 \pm 4.6_{stat}$
p_{T} + 0.05%	$5279.3 \pm 0.2_{stat}$	$11.4 \pm 0.5_{stat}$	$66.4 \pm 4.4_{stat}$
p_{T} - 0.05%	$5277.7 \pm 0.2_{stat}$	$11.4 \pm 0.5_{stat}$	$66.4 \pm 4.6_{stat}$

Table C.1: The mass uncertainty introduced by the hadronic track p_{T} scale to the B^{+}, B_{s1}, and B^{*}_{s2} states in the 2011 data.

and C.4, the corresponding plots with the p_{T} of the hadrons varied up and down by 0.05% are shown. The uncertainty propagated to the B_c mass is found to be 1.2

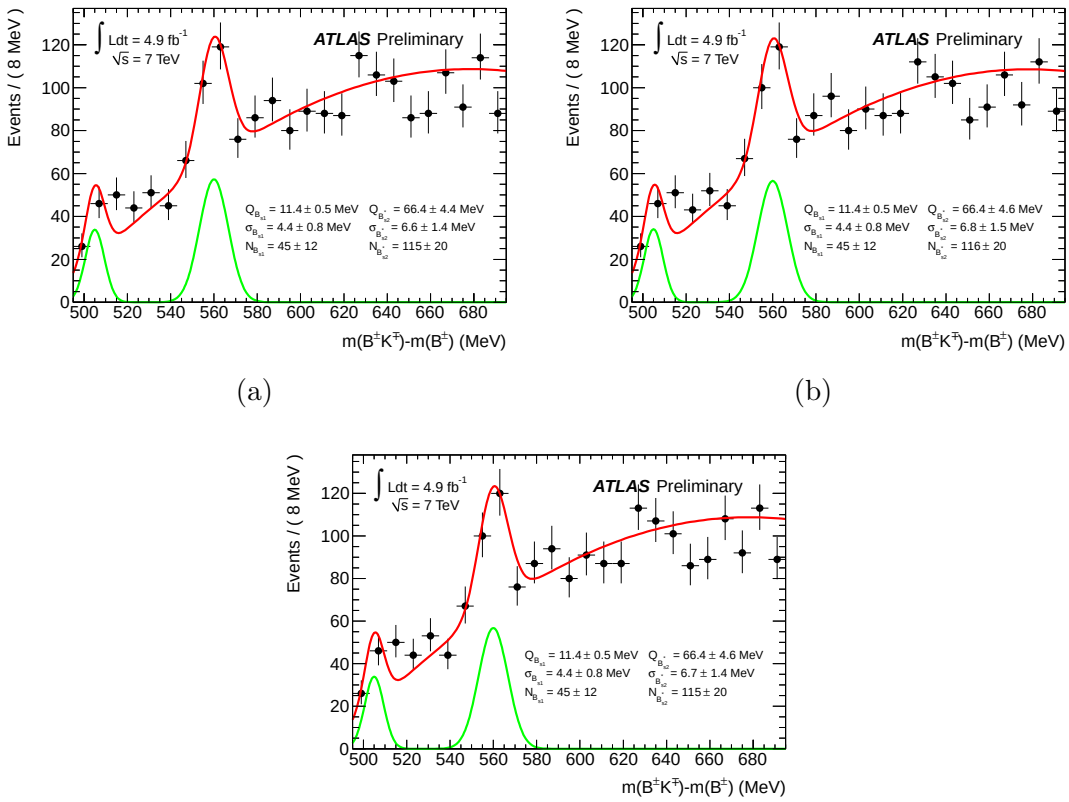

(a) (b)

(c)

Figure C.2: The $B_{s1,2}$ candidates, 2011 data. The p_{T} of all hadronic tracks is scaled up (a) and down (b) by 0.05%. The plot with the original p_{T} of all hadronic tracks is shown for comparison (c).

Hadron p_{T}	$m(B_c)$, MeV	$Q(B_c(2S))$, MeV
original p_{T}	$6281.6 \pm 8.2_{stat}$	$288.2 \pm 5.1_{stat}$
p_{T} + 0.05%	$6282.8 \pm 8.2_{stat}$	$288.3 \pm 5.1_{stat}$
p_{T} - 0.05%	$6280.3 \pm 8.2_{stat}$	$288.0 \pm 5.1_{stat}$

Table C.2: The mass uncertainty introduced by the hadronic track p_{T} scale to the B_c and $B_c(2S)$ states in the 2011 data.

MeV, and the uncertainty propagating to the Q value of the $B_c(2S)$ candidates is about 0.12 MeV. The results are summarized in Table C.2.

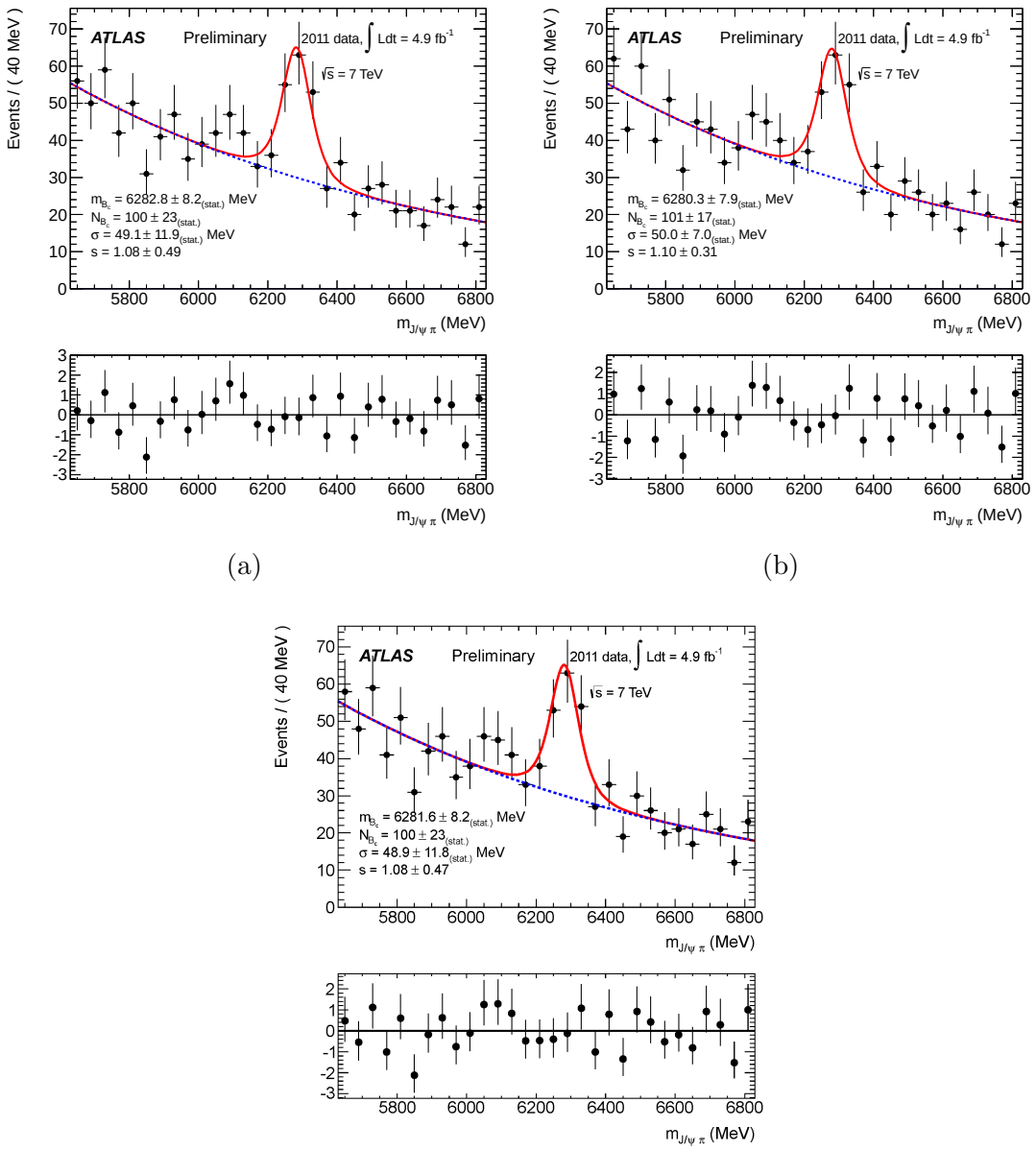

Figure C.3: The $B_c \to J/\psi K^{\pm}$ candidates, 2011 data. The p_{T} of all hadronic tracks is scaled up (a) and down (b) by 0.05%. The plot with the original p_{T} of all hadronic tracks is shown for comparison (c).

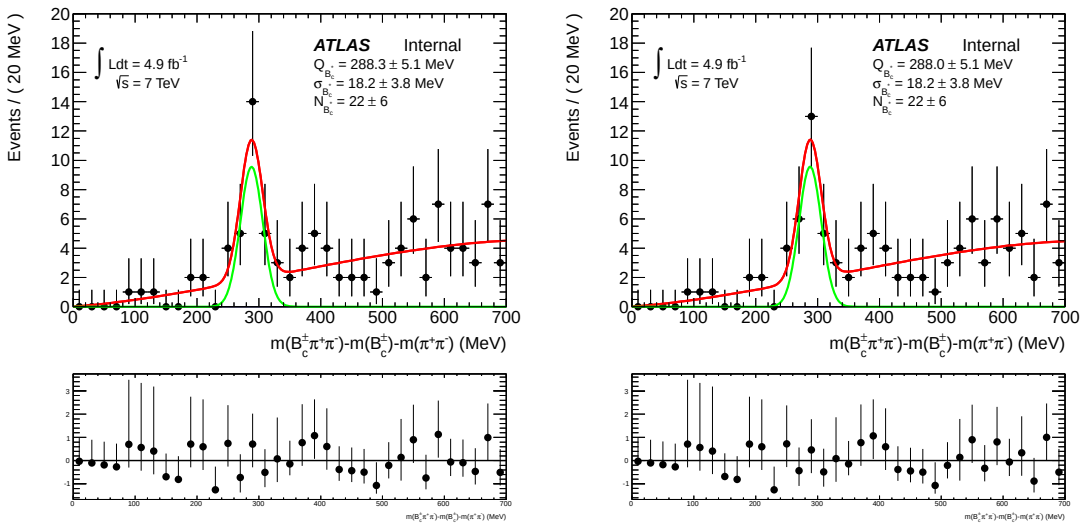

(a)

(b)

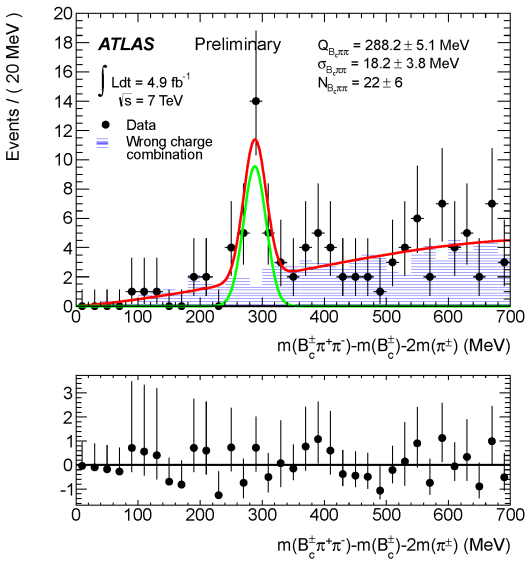

(c)

Figure C.4: The $B_c(2S)$ candidates, 2011 data. The p_{T} of all hadronic tracks is scaled up (a) and down (b) by 0.05%. The plot with the original p_{T} of all hadronic tracks is shown for comparison (c).

Appendix D

Study of the impact of a vertex pointing constraint on pile-up reduction

The analysis of the 2012 data was performed on the Analysis Object Data (AOD). The DAOD (skimed AOD containing di-muon events) of the 2012 B-physics stream was not available until the end of September 2013. This DAOD J/ψ skim has a slightly higher yield of J/ψ, a few percent increase compared to the initial AOD analysis. The DAOD was analyzed on the GRID with the primary vertex pointing constraint enabled.

The motivation for this study was the fact that the background in the 2012 $B_c(2S)$ signal region was significantly higher than in 2011, especially in the higher Q value region. The working hypothesis to be tested was the higher pile-up conditions of 2012, leading to an increase of random combinatorial pions coming from other pp interactions. Strict pointing to the single primary vertex should result in a reduction of the background. The results of the study are shown in Figures D.1 and D.2. Both

figures are fitted with exactly the same fitting procedures as Figure 3.52.

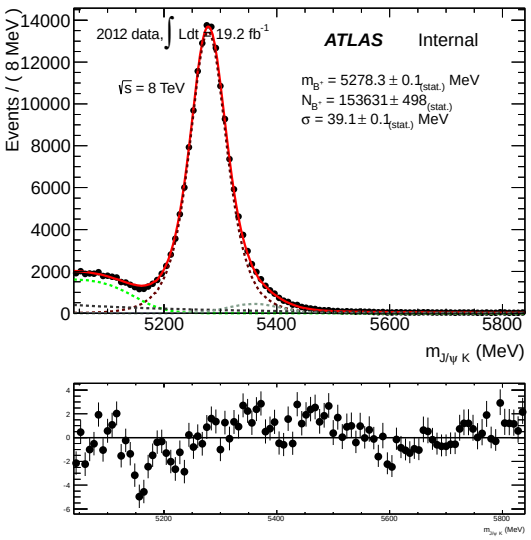

(a)

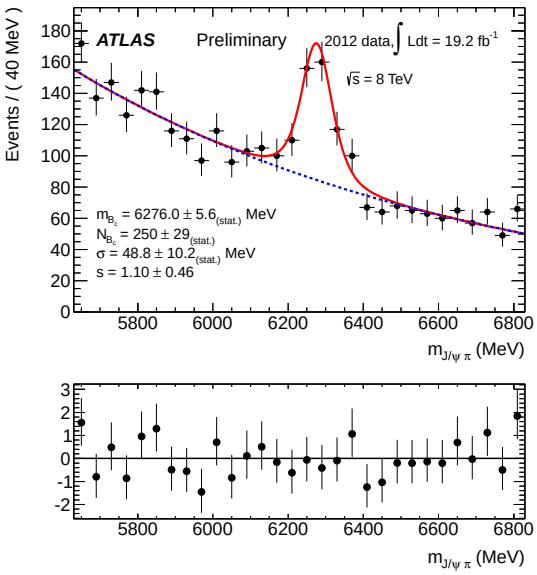

(b)

Figure D.1: The invariant mass distribution for the $B^{\pm}$ (upper) and the $B_c^{\pm}$ (lower) candidates in the 2012 DAOD data. The data are points with error bars. The solid line is the projection of the results of the unbinned maximum likelihood fit.

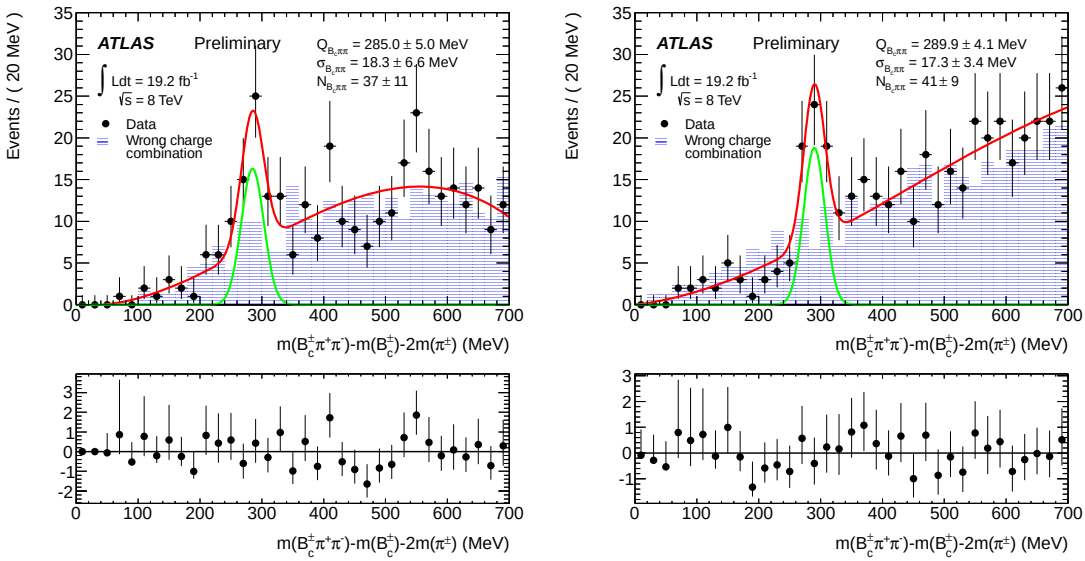

(a) (b)

Figure D.2: The $m(B_c^{\pm}\pi\pi) - m(B_c^{\pm}) - 2 * m_{PDG}(\pi)$ mass difference distribution for the proper charge combinations in the 2012 DAOD with the primary vertex pointing constraint (left) and AOD (right) data. The data are points with error bars. The solid line is the projection of the results of the unbinned maximum likelihood fit.

There is a few percent increase in the yield of the $B^{\pm}$ and B_c ground states. There is a substantial drop in the background rate when the primary vertex pointing constraint is applied. This supports the higher 2012 pile-up hypothesis.

References

[1] S.L. Glashow, *Partial-symmetries of weak interactions*, Nuclear Physics, **22** (1961) 579588.

[2] F. Englert, R. Brout, *Broken Symmetry and the Mass of Gauge Vector Mesons*, Physical Review Letters, **13** (1964) 321323.

[3] P.W. Higgs, *Broken Symmetries and the Masses of Gauge Bosons*. Physical Review Letters, **13** (1964) 508509.

[4] G.S. Guralnik, C.R. Hagen, T.W.B. Kibble, *Global Conservation Laws and Massless Particles*, Physical Review Letters, **13** (1964) 585587.

[5] Dave, Fehling, *The Standard Model of Particle Physics: A Lunchbox's Guide*, (2008).

[6] ATLAS Collaboration, *Observation of a new particle in the search for the Standard Model Higgs boson with the ATLAS detector at the LHC*, Physics Letters B, **716**, 1, (2012), 1-29.

[7] CMS Collaboration, *Observation of a new boson at a mass of 125 GeV with the CMS experiment at the LHC*, Physics Letters B, **716**, 1, (2012), 30-61.

[8] ATLAS Collaboration, *ATLAS detector and physics performance: Technical Design*, ATLAS-TDR-14, CERN-LHCC-99-014, (1999).

[9] CDF Collaboration, F. Abe et al., *Observation of the B_c Meson in $\bar{p}p$ Collisions at $\sqrt{s}$ = 1.8 TeV* , Phys. Rev. Lett. **81** 2432 (1998).

[10] CDF Collaboration, A. Abulencia et al., *Evidence for the Exclusive Decay $B_c^{\pm} \to J/\psi\pi^{\pm}$ and Measurement of the Mass of the B_c Meson*, Phys. Rev. Lett. **96** 082002 (2006).

[11] CDF Collaboration, T. Aaltonen et al., *Measurement of the B_c Lifetime in $B_c^{\pm} \to J/\psi + l^{\pm} + X$ Decays*, Phys. Rev. Lett. **100** 182002 (2008).

[12] CDF Collaboration, A. Abulencia et al., *Measurement of the B_c^+ Meson Lifetime using the Decay Mode $B_c^+ \to J/\psi e^+ \nu_e$*, Phys. Rev. Lett., **97** 012002 (2006).

[13] CDF Collaboration, T. Aaltonen et al., *Measurement of the B_c^- meson lifetime in the decay $B_c^- \to J/\psi\ \pi^-$*, Phys. Rev. D **87** 011101 (2013), arXiv:1210.2366.

[14] D0 Collaboration, V. M. Abazov et al., *Observation of the B_c Meson in the Exclusive Decay $B_c \to J/\psi\pi$*, Phys. Rev. Lett. **101** 012001 (2008).

[15] D0 Collaboration, V.M. Abazov et al., *Measurement of the Lifetime of the $B_c^{\pm}$ Meson in the Semileptonic Decay Channel*, Phys. Rev. Lett. **102** 092001 (2009).

[16] LHCb Collaboration, R Aaij et al., *Measurement of the B_c^+ meson lifetime using $B_c^+ \to J/\psi\mu^+\nu_\mu X$ decays*, CERN-PH-EP-2014-008, LHCB-PAPER-2013-063 (2014), arXiv:1401.6932.

[17] LHCb Collaboration, R Aaij et al., *Measurements of B_c^+ production and mass with the $B_c^+ \to J/\psi\pi^+$ decay*, Phys. Rev. Lett. **109** 232001 (2012), arXiv:1209.5634.

[18] LHCb Collaboration, *Measurement of the B_c^+ to B^+ production cross-section ratio at $\sqrt{s} = 7$ TeV in LHCb*, LHCb-CONF-2011-017 (2011).

[19] ATLAS Collaboration, *Observation of the $B_c^{\pm}$ meson in the decay $B_c^{\pm} \to J/\psi(\mu^+\mu^-)\pi^{\pm}$ with the ATLAS detector at the LHC*, ATLAS-CONF-2012-028 (2012).

[20] CMS Collaboration, *Observation of the decays $B_c \to J/\psi\pi$ and $B_c \to J/\psi\pi\pi\pi$ in pp collisions at $\sqrt{s} = 7$ TeV*, CMS-PAS-BPH-11-003 (2012).

[21] LHCb Collaboration, *First observation of the decay $B_c^+ \to J/\psi\pi^+\pi^-\pi^+$*, Phys. Rev. Lett. **108**, (2012), 251802, LHCB-PAPER-2011-044, CERN-PH-EP-2012-090.

[22] CDF Collaboration, T.S. Nigmanov, K.R. Gibson, M.P. Hartz, P.F. Shepard, *Measurement of B_c properties at CDF*, arXiv:0910.3013v1.

[23] J. Beringer et al. (Particle Data Group), Phys. Rev. D86, 010001 (2012).

[24] E. Eichten, C. Quigg, *Mesons with beauty and charm: Spectroscopy*, Phys. Rev. D **49** (1994) 5845.

[25] S. S. Gershtein et al., *B_c spectroscopy*, Phys. Rev. D **51** (1995) 3613.

[26] S. Ikhdair, *Theoretical Status of the B_c Meson in the Shifted l-Expansion Technique*, hep-ph/0504176 (2005).

[27] S. Godfrey, *Spectroscopy of B_c mesons in the relativized quark model*, Phys. Rev. D **70** (2004) 054017.

[28] A. A. Penin et al., *$M(B_c^*) - M(B_c)$ splitting from nonrelativistic renormalization group*, Phys. Lett. B **593** (2004) 124.

[29] S. Narison, *Beautiful mesons from QCD spectral sum rules*, Phys. Lett. B **210** (1988) 238.

[30] L. Motyka and K. Zalewski, *Mass spectra and leptonic decay widths of heavy quarkonia*, Eur. Phys. J. C **4** (1998) 107.

[31] S. Ikhdair and R. Sever, *B_c and heavy meson spectroscopy in the local approximation of the Schrodinger equation with relativistic kinematics*, hep-ph/0403280 (2004).

[32] M. Baldicchi and G. M. Prosperi, *B_c meson and the light-heavy quarkonium spectrum*, Phys. Rev. D **62** (2000) 114024.

[33] W. Kwong and J. Rosner, *Masses of new particles containing b quarks*, Phys. Rev. D **44** (1991) 212.

[34] S. Kim, *Some properties of B_c from lattice QCD*, hep-lat/9511010.

[35] I. F. Allison et al., *Mass of the B_c Meson in Three-Flavor Lattice QCD*, Phys. Rev. Lett. **94** (2005) 172001.

[36] D. Ebert, R. N. Faustov and V. O. Galkin, *Properties of heavy quarkonia and B_c mesons in the relativistic quark model*, Phys. Rev. D **67**, 014027, (2003), hep-ph/0210381.

[37] S. N. Gupta and J. M. Johnson, *B_c spectroscopy in a quantum chromodynamic potential model*, Phys. Rev. D **53**, 312 (1996), hep-ph/9511267.

[38] J. Zeng, J. W. Van Orden and W. Roberts, *Heavy mesons in a relativistic model*, Phys. Rev. D **52**, 5229, (1995), hep-ph/9412269.

[39] C. T. H. Davies, K. Hornbostel, G. P. Lepage, A. J. Lidsey, J. Shigemitsu and J. H. Sloan, *B_c spectroscopy from lattice QCD*, Phys. Lett. B, **382**, 131, (1996), hep-lat/9602020.

[40] I. P. Gouz, V. V. Kiselev, A. K. Likhoded, V. I. Romanovsky and O. P. Yushchenko, *Prospects for the B_c studies at LHCb*, Phys. Atom. Nucl. **67**, 1559 (2004), [Yad. Fiz. **67**, 1581 (2004)], [hep-ph/0211432].

[41] A. K. Likhoded and A. V. Luchinsky, *Light hadron production in $B_c \to J/\psi + X$ decays*, Phys. Rev. D **81**, 014015 (2010), arXiv:0910.3089.

[42] A. V. Berezhnoy, V. V. Kiselev, A. K. Likhoded, A. I. Onischenko, *B_c Meson at LHC*, Phys. Atom. Nucl. **60**, 1729 (1997).

[43] R. J. Dowdall, C. T. H. Davies, T. C. Hammant and R. R. Horgan, *Precise heavy-light meson masses and hyperfine splittings from lattice QCD including charm quarks in the sea*, Phys. Rev. D **86**, 094510 (2012), arXiv:1207.5149 [hep-lat].

[44] J. M. Campbell, J. W. Huston, and W. J. Stirling, *Hard interactions of quarks and gluons: a primer for LHC physics*, Reports on Progress in Physics **70**, 1 (2007) 89.

[45] R. A. Bertlmann and A. Martin, *Inequalities on heavy quark-antiquark systems*, Nucl. Phys. B **168** (1980) 111.

[46] R. Roncaglia et al., *Predicting the masses of heavy hadrons without an explicit Hamiltonian*, Phys. Rev. D **51** (1995) 1248.

[47] P. Jain and H. Munczek, *$q\bar{q}$ bound states in the Bethe-Salpeter formalism*, Phys. Rev. D **48** (1993) 5403.

[48] L. Fulcher et al., *Energies of quark-antiquark systems, the Cornell potential, and the spinless Salpeter equation*, Phys. Rev. D **47** (1993) 4122.

[49] Y.-Q. Chen and Y.-P. Kuang, *Improved QCD-motivated heavy-quark potentials with explicit $\Lambda_{\overline{MS}}$ dependence*, Phys. Rev. D **46** (1992) 1165.

[50] N. Brambilla et al., *QCD potential at $O(1/m)$*, Phys. Rev. D **63** (2001) 014023.

[51] A. Pineda and A. Vairo, *The QCD potential at $O(1/m^2)$: Complete spin-dependent and spin-independent result*, Phys. Rev. D **63** (2001) 054007.

[52] K. Toms and A. Berezhnoy, *ATLAS PythiaBc Monte Carlo Generator for B_c meson production*, ATL-COM-PHYS-2012-549, (2012).

[53] ATLAS Collaboration, JHEP **10** (2013) 042, arXiv:1307.0126 [hep-ex]. (2013).

[54] CMS Collaboration, Phys. Rev. Lett. **106** (2011) 112001, arXiv:1101.0131.

[55] LHCb Collaboration, *Observations of Orbitally Excited $B^{**}_{(s)}$ Mesons*, LHCb-CONF-2011-053 (2011).

[56] CDF Collaboration, *Study of orbitally excited B mesons and evidence for a new $B\pi$ resonance*, submitted to Phys. Rev. D, FERMILAB-PUB-13-393-E (2013).

[57] L. Evans and P. Bryant, *LHC Machine*, JINST **3** (2008) S08001.

[58] ATLAS Collaboration, *The ATLAS Experiment at the CERN Large Hadron Collider*, JINST **3** (2008) S08003.

[59] ATLAS Collaboration, *Improved Luminosity Determination in pp Collisions at 7 TeV using the ATLAS Detector*, Eur. Phys. J. **C** (2013) 73:2518.

[60] ATLAS Collaboration, *J/ψ Performance of the ATLAS Inner Detector*, ATLAS-CONF-2010-078.

[61] ATLAS Collaboration, *VKalVrt – package for vertex reconstruction in ATLAS*, ATL-PHYS-2003-031 (2003).

[62] ATLAS Collaboration, *Observation of the $B^{\pm}$ meson in the decay $B^{\pm} \to J/\psi(\mu^+\mu^-)K^{\pm}$*, ATL-CONF-2010-098 (2010).

[63] L. Moneta et al., *The RooStats Project*, (2011). arXiv:1009.1003v2.

[64] G. Schott et al., *RooStats for Searches*, (2012). arXiv:1203.1547v1.

[65] `https://mediastream.cern.ch/MediaArchive/Photo/Public`, 2008.

[66] `https://twiki.cern.ch/twiki/bin/view/AtlasPublic`.

[67] ATLAS photos, `http://www.atlas.ch/photos/`.

[68] ATLAS Collaboration, *Performance of the ATLAS Inner Detector Track and Vertex Reconstruction in the High Pile-Up LHC Environment*, ATLAS-CONF-2012-042.

[69] ATLAS Collaboration, *Muon reconstruction efficiency in reprocessed 2010 LHC p-p collision data recorded with the ATLAS detector*, ATLAS-CONF-2011-063 (2011).

[70] ATLAS Collaboration, *Preliminary results on the muon reconstruction efficiency, momentum resolution, and momentum scale in ATLAS 2012 pp collision data*, ATLAS-CONF-2013-088 (2013).

[71] ATLAS Collaboration, *Performance of the ATLAS Trigger System in 2010*, Eur. Phys. J. **C72** (2012) 1849.

[72] W. Ji, S. Seidel, S. Sivoklokov, and K. Toms, *Measurement of the Mass of the B_c Meson through the Decay $B_c \to J/\psi\pi$*, ATL-COM-PHYS-2010-261 (2010).

[73] G. Aad, et al., *Track Reconstruction Efficiency in $\sqrt{s} = 7$ TeV Data for Tracks with $p_{\mathrm{T}} > 100$ MeV*, ATL-PHYS-INT-2011-001, 2011.

[74] `https://svnweb.cern.ch/trac/atlasoff/browser/Tracking/TrkEvent/TrkParameters`.

[75] `https://svnweb.cern.ch/trac/atlasoff/browser/Generators/PythiaBc_i`.

[76] D. Lange, *The EvtGen particle decay simulation package*, Nucl. Inst. Meth. A **462**, 152 (2001).

[77] T. Sjöstrand, S. Mrenna and P. Z. Skands, *PYTHIA 6.4 Physics and Manual*, JHEP **05** (2006) 026, arXiv:hep-ph/06/03175.

[78] T. Sjöstrand, S. Mrenna and P. Z. Skands, *A Brief Introduction to PYTHIA 8.1*, Comput. Phys. Comm. 178 (2008) 852, arXiv:0710.3820.

[79] Maria Smizanska, *PythiaB interface to Pythia6 dedicated to simulation of beauty events.*, `https://svnweb.cern.ch/trac/atlasoff/browser/Generators/PythiaB/trunk/doc/PythiaB.pdf`, (2005).

[80] S. Agostinelli et al., *Geant4: A simulation toolkit*, Nucl. Inst. Meth. A **506 no. 3**, (2003) 250303.

[81] S. S. Wilks, *The large-sample distribution of the likelihood ratio for testing composite hypotheses*, Ann. Math. Statist. **9**, 60 (1938).

[82] R. Royall, *On the probability of observing misleading statistical evidence*, J. Amer. Statist. Assoc. **95**, 760 (2000).

[83] G. Cowan, K. Cranmer, E. Gross and O. Vitells, *Asymptotic formulae for likelihood-based tests of new physics*, Eur. Phys. J. C **71**, 1554 (2011), arXiv:1007.1727 [physics.data-an].

[84] ATLAS Collaboration, *Physics at a High-Luminosity LHC with ATLAS*, ATL-PHYS-PUB-2012-004.

[85] ATLAS Collaboration, *Letter of Intent for the Phase-II Upgrade of the ATLAS Experiment*, CERN-LHCC-2012-022; LHCC-I-023.

[86] ATLAS Collaboration, *ATLAS Insertable B-Layer Technical Design Report*, CERN-LHCC-2010-013; ATLAS-TDR-19; *ATLAS Insertable B-Layer Technical Design Report Addendum*, CERN-LHCC-2012-009; ATLAS-TDR-19-ADD-1.

[87] ATLAS Collaboration, *Letter of Intent for the Phase-I Upgrade of the ATLAS Experiment*, CERN-LHCC-2011-012; LHCC-I-20.

[88] P. Palni et al., *A method for real time monitoring of charged particle beam profile and fluence*, Nuclear Instruments and Methods in Physics Research Section A, **735**, (2014), 213:217.

[89] M. Marinelli, et al., *High-Quality Diamond Grown by Chemical-Vapor Deposition: Improved Charge Collection Efficiency in α-Particle Detection*, Appl. Phys. Lett. vol. 75, no. 20 (1999) 3216-3218.

[90] P.J. Sellin, et al., *Imaging of Charge Transport in Polycrystalline Diamond Using Ion-Beam-Induced Charge Microscopy*, Appl. Phys. Lett. vol. 77, no. 6 (2000) 913-915.

[91] M. Schloegl and B.E. Fischer, *Investigation of the Detection Efficiency of Polycrystalline Diamond Detectors with a Heavy Ion Microprobe*, Proc. 1999 Fifth European Conf. on Radiation and its Effects on Components and Systems, Fontevraud, France (2000) 132-135.

[92] A. Brambilla, et al., *Thin CVD Diamond Detectors With High Charge Collection Efficiency*, IEEE Trans. Nucl. Sci. vol. 49, no. 1 (2002) 277-280.

[93] A. Gorisek, et al., *ATLAS Diamond Beam Condition Monitor*, Nucl. Instr. and Meth. A **572** (2007) 67-69.

[94] E. Bartz et al., *The PLT: A Luminosity Monitor for CMS Based on Single-Crystal Diamond Pixel Sensors*, Nucl. Phys. B Proc. Suppl. **197** (2009) 171-174.

[95] D. Asner et al., *Diamond Pixel Modules,* Nucl. Instr. and Meth. A **636** (2011) S125-S129.

[96] Element six, `www.e6.com`.

[97] S. Zhao, *Characterization of the Electrical Properties of Polycrystalline Diamond Films*, Ph.D. dissertation, The Ohio State University, 1994 (unpublished).

[98] R. Boyd, *ATLAS Pixel PP4 HV Design. Specification for construction and use of Patch Panel 4 High Voltage Services*, CERN EDMS Document, Number: ATL-IP-ER-0017, EDMS Id: 772658, 2006-09-11, CERN.

[99] Iseg Spezialelektronik GmbH, Bautzner Landstr. 23, D-01454 Radeberg/Rossendorf, `http://www.iseg-hv.de`, *High Voltage Power Supply EHQ F607n-F*, Operator's Manual.

[100] S. M. Sze, *Semiconductor Devices Physics and Technology*, John Wiley & Sons, 1985.

[101] M. Moll et al., [CERN-ROSE/RD48 Collaboration], *Radiation damage in particle silicon sensors*, Nucl. Instr. Meth. A **426** 87 (1999).

[102] `https://twiki.cern.ch/twiki/bin/viewauth/Atlas/BenchmarkingAtTheLHC`.

[103] I. Gorelov et al., *ATLAS Pixel Radiation Monitoring with HVPP4 System*, eConf C090726, `http://arxiv.org/abs/0911.0128`, (2009).

[104] *Embedded Local Monitor Board ELMB128*, `http://elmb.web.cern.ch/ELMB/elmb128_1.pdf`.

[105] O. Krasel, *Charge collection in irradiated silicon detectors*, `http://hdl.handle.net/2003/2354`, 2004.